A SAR-derived long-term record of glacier evolution in North-West Greenland.

Reinier Oost

Technische Universiteit Delft

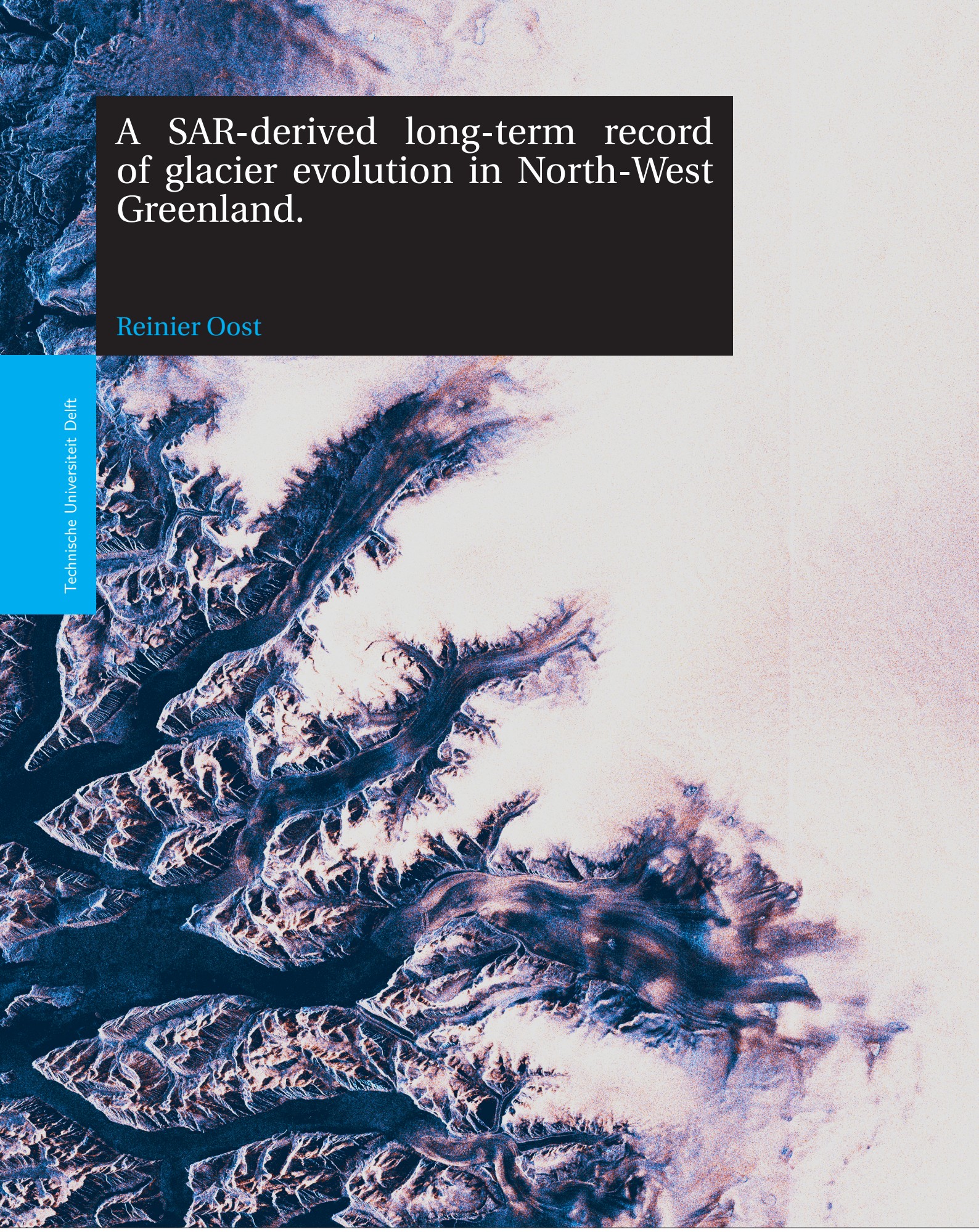

TU Delft Delft University of Technology

Challenge the future

On the cover
A false color image of a duo-polarized Sentinel-1A Extra-Wide SLC-image above the Uummannaq-region. The different polarizations have been assigned different RGB-bands.

A SAR-derived long-term record of glacier evolution in North-West Greenland.

by

Reinier Oost

in partial fulfillment of the requirements for the degree of

Master of Science
in Applied Earth Sciences

at the department of Geoscience and Remote Sensing
of the Delft University of Technology.

Student number:	1515500	
Supervisor:	Prof. dr. ir. R.F. Hanssen,	TU Delft
Thesis committee:	Dr. ir. F. van Leijen,	TU Delft
	Dr. M. Vizcaino,	TU Delft
Co-reader	Dr. P. G. Ditmar,	TU Delft

TU Delft Delft University of Technology

I just wish the world was twice as big and half of it was still unexplored.

David Attenborough

PREFACE

The icy worlds of the Arctic and the Antarctic are the last real wilderness, almost as unknown as the surface of another planet. They have always triggered my imagination, as most of these landmasses are still unaffected by human cultivation; a sharp contrast to the Dutch human-made landscape I cycle through every day. The unexplored nature of the ice sheets inspired me to study their dynamics, and to investigate how anthropogenic climate change will change the world of tomorrow.

During this study I read many articles, processed many radar images and thought of various theories and hypothesis. Working with large datasets showed me that space-based data has an enormous potential. The next decades will be the era of information, where data is abundant, and the next challenges are not how to obtain data, but how to mine it.

With this thesis I conclude my long journey at the TU Delft. It started in 2008 at Aerospace Engineering, where I got to understand the basic principles of technology. Where most Aerospace Engineers were fascinated by the physical principles of an aircraft or spacecraft, my fascination was to look out of the window, down on the Earth. Therefore, I decided to start a master at Geoscience and Remote Sensing, a decision never to regret. This thesis also marks the end of my student life, undoubtedly the best time of my life.

I would like to express my gratitude to my supervisors that supported me in this study. I would like to thank professor Ramon Hanssen, who always triggered me to reach higher levels and to learn even more. Another word of gratitude goes to Miren Vizcaino for her supervision on the glaciological part, and who was always prepared to give suggestions and feedback, even during the weekend. Furthermore, I would like to thank Freek van Leijen for his daily supervision on the data processing, and who was always willing to answer my, sometimes stupid, questions. Thanks as well to Pavel Ditmar, who was prepared to be my co-reader.

Last, but certainly not least, plenty of thanks goes my girlfriend, family, friends, colleagues and fellow students that supported and motivated me. Thanks for hearing my complaints and nerdy talks about the study, and thanks for helping me with finding solutions or new motivation. I will never forget all the coffees we drank. Without all your support, I would not have been able to complete this study.

Reinier Oost
Delft, May 2016

ABSTRACT

Observations show that the Greenland ice sheet is losing mass with accelerating pace. Ice discharge trough outlet glaciers contributes approximately for half of the mass loss. However, the role of marine-terminating outlet glaciers on the response of the Greenland ice sheet to climate change is relatively unknown. In recent years, observations have shown dramatic changes in the velocity and front position in a number of marine-terminating outlet glaciers, but a questions remains why some outlet glaciers are stable and others are not. Consequently, predictions on the evolution of the Greenland ice sheet are uncertain until a realistic representation of marine-terminating outlet glaciers is possible. More specifically, significant uncertainty exists on the link between climate forcing and marine-terminating outlet glacier behaviour. This link has been associated to glaciers-specific factors, such as bedrock topography and fjord width, but more glaciers need to be studied. Here we present a study that focussed on the response of different glaciers to a similar climate forcing, thereby taking into account their topographic situation. SAR observations of seven marine-terminating glaciers in the Uummannaq-bay (West-Greenland) are used to estimate terminus positions and glacier flow velocity. The observations are acquired between 1991 - 2014 using ERS, Envisat and TerraSAR-X, thereby extending the length of the state-of-the-art records. Terminus positions are manually digitized and an equivalent position is determined on the glacier flowline, a significant improvement with respect to the box-method. Glacier flow velocities are obtained using ICC offset tracking. The estimated offsets of ERS and Envisat image pairs were noisy, but have been filtered using the along-track velocity profile that was accurately estimated with TerraSAR-X image pairs.

The results showed that the outlet glaciers in this region have been stable during the 1990's, and that the warm winter of 2003 initiated retreat. Three glaciers (Lille Gletscher, Umiammakku Isbræ and Inngia Isbræ) have found to show terminus retreat, of which Lille Gletscher and Inngia Isbræ show long-term speed-up. All other glaciers have a stable terminus position, and show no long-term acceleration. Surface air temperature and sea surface temperature show an increasing trend since 1980, whereas the duration of high ice concentrations (sea-ice melange) becomes shorter each year. The retreat of Umiammakku Isbræ and Inngia Isbræ starts after the winter of 2003, in which surface air temperatures were exceptionally high and the period of sea ice was short. The years after, this retreat continued even under normal climatic conditions. Inngia Isbræ showed an ongoing retreat of approximately 6 km between 2003 and 2013, and its flow velocity is estimated to tripled from 500 m/yr to 1500 m/yr. On the contrary, Umiammakku Isbræ ceased its 4 km retreat in 2010, and did not show a increase in flow velocity. Next to long-term patterns, seasonal patterns are identified to differ from glacier to glacier. The terminus position of Rink Isbræ shows a seasonal variation of 1 km, whereas the terminus position of Støre Gletscher only fluctuates around 200 m.

The three retreating glaciers are located in a shallow fjord (< 300 m depth) with a reversed bedrock slope. Their retreat into deeper waters initiated a positive feedback-loop leading to multi-year retreat. Glaciers located in a deep fjord (Rink Isbræ and Støre Gletscher) are exposed to warm Atlantic waters, and consequently subject to submarine-melting, but our results show that their front position remained stable and their flow velocity did not increase. The fact that the retreating glaciers are located in a shallow fjord, and exposed to cold Polar water, could indicate that submarine-melting is not a major factor controlling glacier retreat. This also indicates that the bedrock topography is important for a glaciers sensitivity to climate forcing. It is recommended that more effort is put into observations of the submarine-melting process and high resolution bedrock topography and bathymetry, as the relative importance of submarine-melting with respect to the surface mass balance and calving is still obscure. Nevertheless, our results suggest that there is an important link between the fjord depth at the terminus location and the sensitivity to climate forcing.

ABBREVIATIONS

AIS	Antarctic Ice Sheet
AW	Atlantic Water
BLUE	Best Linear Unbiased Estimator
CCC	Coherent Cross-Correlations
CRS	Coordinate Reference System
DEM	Digitial Elelvation Model
DEM+	adapted Digitial Elelvation Model (with manually filled fjords)
DMI	Danish Meteorological Office
DORIS	Delft Object-oriented Radar Interferometric Software
EGV	Equivalent Glacier Velocity
ELA	Equilibrium Line Altitude
EM	Electro Magnetic
ERS	European Remote sensing Satellite
ESA	European Space Agency
ETP	Equivalent Terminus Position
GIMP	Greenland Ice Mapping Project
GRD	Ground Range Detection
GrIS	Greenland Ice Sheet
ICC	Incoherent Cross-Correlations
IDW	Inverse Distance Weighting
InSAR	Interferometric Synthetic Aperture Radar
IPCC	International Panel of Climate Change
LOS	Line Of Sight
MB	Mass Balance
MIT	Mittarfeqarfiit (Greenlandic Airports)
MW	Mixed Waters
NASA	National Aeronautics and Space Administration
NOAA	National Oceanic and Atmospheric Administration
OT	Ocean Temperature
pdf	Probability Density Function
POES	Polar Operational Environmental Satellites
PW	Polar Water
SAR	Synthetic Aperture Radar
SAT	Surface Air Temperature
SIF	Sea Ice Fraction
SIMONE	Surface Ice Motion by Offset-tracking Non-stationary Estimates
SLC	Single Look Complex
SMB	Surface Mass Balance
SST	Sea Surface Temperature
SW	Surface Water
TSX	TerraSAR-X
YCM	Yaw Control Mode

CONTENTS

List of Figures

LIST OF TABLES

1

INTRODUCTION

Outlet glaciers, ice streams that drain ice sheets, are small but important features in the cryosphere, as it is estimated that they are responsible for half of the ice loss of ice sheets (Bamber et al., 2007). The mass lost by the ice sheets leads to sea level rise, and the Intergovernmental Panel of Climate Change (IPCC) estimated that the total sea level rise by 0.25 to 1 m in the year 2100, of which 0.03 to 0.20 m is contributed by ice sheets. Although ice sheets are not the main contributors to sea level rise, the Greenland Ice Sheet (GrIS) and Antarctic Ice Sheet (AIS) contain a sea level equivalent of 7.4 m and 58.3 m (IPCC, 2013), respectively, if they would completely melt into the ocean. Their role in sea level rise is suggested to become more dominating in a warmer climate. Rignot et al. (2011) estimated that the combined mass loss of the GrIS and AIS was about 475 ± 158 Gt/yr in 2006, and that the contribution of GrIS to this loss is accelerating with 21.9 ± 1 Gt/yr^2, more than the AIS acceleration. More specifically, Enderlin et al. (2014) estimated that the GrIS loss due to ice discharge rose from 389 ± 5 Gt/yr in 2000 to 546 ± 11 Gt/yr in 2010. The total contribution of the GrIS to sea level rise is estimated at 0.46 mm/yr between 2000 and 2008 (Broeke et al., 2009). According to the IPCC, (2013), there is high confidence that the GrIS mass balance has become more negative over the last two decades, mainly due to increased surface melt and ice discharge.

The future mass balance of the ice sheets is predicted by numerical models. However, numerical models have not been able to predict the current changes of the GrIS mass balance, implying that predictions of the future are very uncertain (Bamber et al., 2007). Although new ice sheet models are suggested to allow a more realistic simulation of the role of outlet glaciers, the understanding of their interactions with climate forcing has not reached the level that a realistic coupling between climate models and ice sheet models can be established. In order to have more reliable projections of ice sheet evolution, and consequently future sea-level rise, the climate models should be improved with more realistic physical representation of the role that outlet glaciers are going to have in the future (Straneo et al., 2013).

The influence of the climate on the evolution of marine-terminating outlet glaciers is different for each individual glacier. More specifically, the relevant climate forcing parameters are ocean temperature, surface air temperature and sea ice concentrations. The sensitivity of a glacier to these climate forcing parameters is determined by glacier-specific factors, i.e., bedrock topography, terminus type (Carr et al., 2013a, Howat et al., 2010, Moon et al., 2014, Moon et al., 2015). Due to the complexity of glaciological processes, such as the influence of fjord geometry and bedrock on the sensitivity to climatic/oceanic forcing, the current models cannot explain the timing and magnitude of glacier changes (Bamber et al., 2007). Our understanding of these processes is mainly based on extensive research on a small number of glaciers, such as the Jakobshavn Isbrae, Helheim Glacier and Kangerdlugssuaq Glacier, but it is not known if these results can be extrapolated on other Arctic glaciers and to what time-scale the observed changes apply (Carr et al., 2013a). There are three directions of future research needed to understand these processes: 1) Spatial variability of the climatic and oceanic forcing and their relative importance, 2) the influence of glacier-specific factors and 3) development

of outlet glacier dynamics in numerical models based on observations (Carr et al., 2013a).

In light of these directions, we present a study that will focus on linking climatic forcing and glacier-specific factors by observing the behaviour and evolution of 7 marine-terminating glaciers for more than 20 years and linked to climatic/oceanic forcing and their topographic situation. The observations are done using space-based Synthetic Aperture Radar (SAR) images from ERS-1/2, Envisat and TerraSAR-X satellites. Using these images glacier terminus positions and surface velocities are estimated to assess a glacier its stability in terms of mass balance. The area of interest, the Uummannaq region (see Figure 1.1), is chosen because all glaciers are within a shielded bay, hence the climatic/oceanic forcing on each glacier can be presumed to be similar. This allows the glacier evolution to be compared with their specific geometry, i.e., fjord width, bedrock. The air of this study is to increase the temporal and spatial scale of current observations, and to extend the knowledge on the role of glacier-specific factors on climate forcing and to validate and improve models.

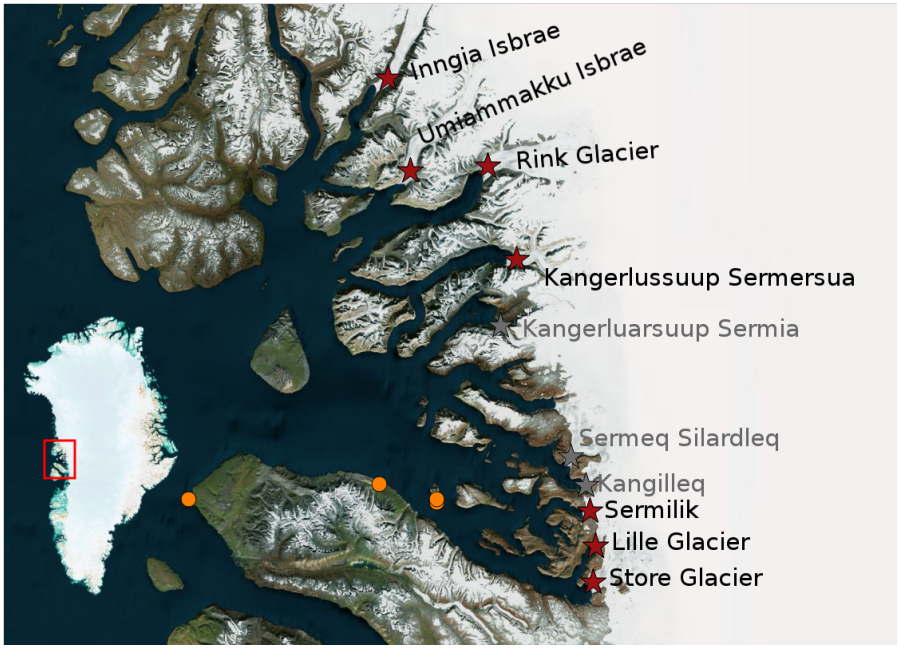

Figure 1.1: An overview of the Uummannaq Bay, located in West-Greenland. Red stars indicate the studied glaciers, gray stars indicate glaciers left out of the study. The orange dots indicate weather stations.

1.1. PROBLEM STATEMENT, MOTIVATIONS AND OBJECTIVES

Outlet glaciers evolution is an important link between climate change and ice sheet mass balance, as they are the frontiers of ice sheets that interact with the sea and air. Marine-terminating glaciers are key-elements in the development of an ice sheet, but their evolution due to climate change is not sufficiently understood to make realistic predictions. Although the parameters and mechanisms are identified that link glacier behaviour to climate change, current research has mainly focussed on a select group of, mainly large, glaciers over short temporal scales. In order to understand the evolution of Marine-terminating glaciers, research has to be expanded, both spatially and temporally, and focussed on the role of glacier-specific factors to the sensitivity of climate forcing.

The main objective of this study is therefore to

> *observe and interpret how different marine-terminating glaciers are responding to a similar climate forcing.*

For this purpose, surface flow velocity and terminus position estimates are made for 7 glaciers in the Uummannaq-region for a long period (1991 - 2014) and associated to external forcing by sea surface temperature, air surface temperature and sea ice fraction. The Uummannaq region is selected due to its location

and topography. As the region is located in a bay with one connection to the sea, the conditions within this region are likely to be the uniform, which enables a proper comparison between individual glaciers.

1.2. RESEARCH QUESTION

Based on the problem statement, motivations and objectives, a research question is formulated:

How do different marine-terminating outlet glaciers respond to a similar climate forcing?

As this question brings up different elements, the question is divided in sub-questions. First, the response of the glaciers is estimated in terms of terminus position and flow velocity using SAR-images. Second, the response is subdivided into seasonal and long-term evolution to understand how long-term evolution is initiated. Third, a relationship between climate forcing parameters and glacier evolution is made. And forth, the differences between glaciers are evaluated based on their glacier-specific factors, such as fjord-width, basal topography and terminus-type. The general research question is therefore subdivided into four sub-questions:

- *How to observe and interpret glacier behaviour using synthetic aperture radar?*
- *What seasonal and long-term evolution can be observed at the glaciers in the Uummannaq-region?*
- *How does climate forcing influence the behaviour of glaciers in the Uummannaq-region?*
- *How do glacier-specific factors influence the behaviour of different glaciers in the Uummannaq-region?*

1.3. OUTLINE

This thesis consists five chapters and one appendix. The current chapter is an introduction to the study. Here the aim of the study is defined and a motivation is formulated. This is done in the perspective of the current state-of-the-art understanding of marine-terminating outlet glaciers, and their relevance to ice sheets and climate change.

Chapter 2 contains the scientific and technical background relevant for this study. The chapter starts with a description of the glaciological concepts of marine-terminating outlet glaciers, followed by an overview of Synthetic Aperture Radar (SAR) and how SAR can be used for glaciological observations. The concepts elaborated in this chapter serve as a basis for the rest of the thesis.

The algorithms, that were applied to translate SAR images into glacier behaviour, are elaborated in Chapter 3. Here the SAR-processing and post-processing are covered. During the SAR processing, the images are coregistrated and offsets are estimated. The post-processing follows after, in which equivalent flow velocities are estimated and an equivalent terminus position is found.

In Chapter 4 the results of this study are presented and discussed. The chapter starts off with an overview of the climatic evolution in the Uummannaq-area, followed by the glaciological evolution and the topographic situation. The interactions between the different components, climatic evolution, glaciological evolution and topographic situation, are discussed in the synthesis. Next to this, based on the quality of the results the used algorithms are also evaluated. Many results have been generated in this study, of which all the detailed results can be found in Appendix A.

The thesis is concluded with Chapter 5. Here one can find the conclusions that try to answer the research question and its sub-questions. In addition, recommendations are given for future studies.

2

TECHNICAL AND SCIENTIFIC BACKGROUND

In this chapter the technical and scientific background, relevant for this study, is elaborated. First, the science behind glaciers and the climate system are considered in Section 2.1, followed by a description of SAR remote sensing in Section 2.2. In Section 2.3 the principles of radar remote sensing of the cryosphere are discussed and in Section 2.4 the external data is described.

2.1. GLACIERS AND THE CLIMATE

Glaciers can be found mainly in the polar and mountainous regions. Glaciers found in mountainous regions are commonly draining from an ice-cap, which are generally found at high elevations where conditions are cold enough. On exteriors of the Greenland Ice Sheet (GrIS) and Antarctic Ice Sheet (AIS), ice streams are draining ice to the oceans. According to the IPCC, these ice streams are 'outlet glaciers' and they are an integral part of the ice sheet (IPCC, 2013). However, in literature the term 'outlet glacier' is also used for ice streams draining ice caps or ice fields (Carr et al., 2013a). In this thesis we are studying outlet glaciers that are connected to the GrIS and, for convenience, we also refer to them as glaciers.

In this section the glaciological principles are discussed. First in Section 2.1.1 the glaciological concepts are discussed, followed by a more detailed elaboration of marine-terminating glaciers in Section 2.1.2 and a description of the regional aspects in Section 2.1.3.

2.1.1. GLACIOLOGICAL CONCEPTS

For a glacier to form, it is required that there is sufficient accumulation (snowfall) to form a compacted ice mass which will, under the pressure of its own weight, start to move downward. The glacier is in equilibrium if the ablation (melting, sublimation) is equal to the accumulation. The total Surface Mass Balance (SMB), in kg per year, defined as B_s, is therefore defined as:

$$B_s = \int_{area} \dot{b} dx dy \tag{2.1}$$

where $\dot{b}$ is the specific balance rate in kg per m^2 per year, and it differs along the glacier coordinates x and y. A positive $\dot{b}$ means accumulation, a negative $\dot{b}$ means ablation. $\dot{b}$ is mainly influenced by temperature, which is dependent on altitude (when considering a yearly average). The equilibrium line E is defined to be a line at which $\dot{b} = 0$, see Figure 2.1. The area above the line is the accumulation area (mass gain), and the area below this line is the ablation area (mass loss). As altitude is the most important factor of the equilibrium line, the Equilibrium Line Altitude (ELA) is introduced. The ELA is a representation of the climatic conditions. If the climate becomes warmer, the ELA moves up, if the climate cools down, the ELA moves down. In both cases, the glacier will either decrease or increase it's ablation area (Van der Veen, 2013).

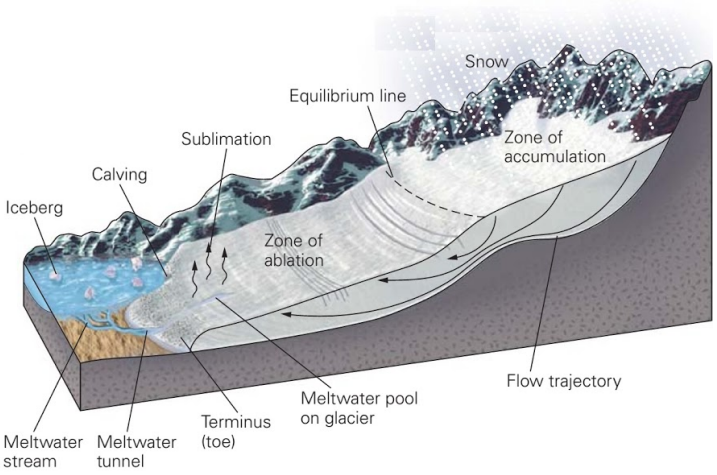

Figure 2.1: An overview of the accumulation and ablation area of a glacier. The equilibrium line is located at an altitude where accumulation is equal to ablation (melting and sublimation). Apart from ablation, a glacier can lose mass trough calving (Marshak,).

Apart from the ablation, a glacier can also lose mass by ice discharge to the ocean through iceberg calving and melt from ocean heat flux. The total Mass Balance (MB) is then defined as:

$$B_s + C = 0 \tag{2.2}$$

where C denotes the mass loss by calving (in kg per year). In the case of outlet glaciers, the accumulation zone is much larger than the ablation zone and it also extents to high altitudes (3 km). Hence, with small accumulation rates the ice-sheet can still be in equilibrium condition (Van der Veen, 2013). Moreover, the SMB of the GrIS and AIS is positive (more accumulation than ablation) and their mass loss is due ice discharge through calving and submarine melting.

Glacier flow is driven by gravity. Ice at higher elevations is pulled down, and follows the topography. The motion of the ice is countered by friction with bedrock, both at the base and at the sides, and by the longitudinal stress. (Van der Veen, 2013) described a glacier force budget:

$$\underbrace{\frac{\partial}{\partial x}(2HW\tau_{xx})}_{\text{Longitudinal Stress Gradients}} + \underbrace{(\tau_{y1}+\tau_{y2})H}_{\text{Friction at sides}} + \underbrace{\tau_b W}_{\text{Friction at base}} = \underbrace{-\rho g H \frac{\partial h}{\partial x} W}_{\text{Driving Stress}}. \tag{2.3}$$

Here the right-hand term is the driving stress, defined by ice thickness H, glacier width W, ice density ρ, slope $\frac{\partial h}{\partial x}$ and gravity g. This driving stress is balanced by resistive forces. The first left-hand side term denotes the effect of the longitudinal stress gradient, that is a derivative of the average longitudinal stress τ_{xx}. In case of a free floating ice shelf this is the only term to counter the driving stress as there is no friction. The friction at the sides is represented by the second left-hand term, where τ_{y1} and τ_{y2} denote the contributions from both sides. The basal friction is represented by the third left-hand term, and this is, in many cases, the most important force to counter the driving stress (Van der Veen, 2013).

Based on this force balance, it is expected that if the right-hand side is larger than the left-hand side, a glacier will accelerate until an equilibrium state is found again. Assuming that the driving stress from an ice-sheet is stable, it is likely that variations in glacier flow are caused by changes of the parameters on the left side. When the friction parameters become lower due to lubrication (i.e., frictional heating, meltwater), the glacier is also likely to accelerate. Next to this, a glacier that becomes narrower or thinner will accelerate until the friction parameters are high enough to resist the driving stress.

2.1.2. MARINE-TERMINATING GLACIERS

Three types of glaciers can be found on the Greenland ice sheet (GrIS): land, marine and ice shelf-terminating glaciers. They are different due to the extent of their front position, that is defined as glacier terminus. The first type has a terminus located on land, the second has a terminus located in the ocean (either floating or

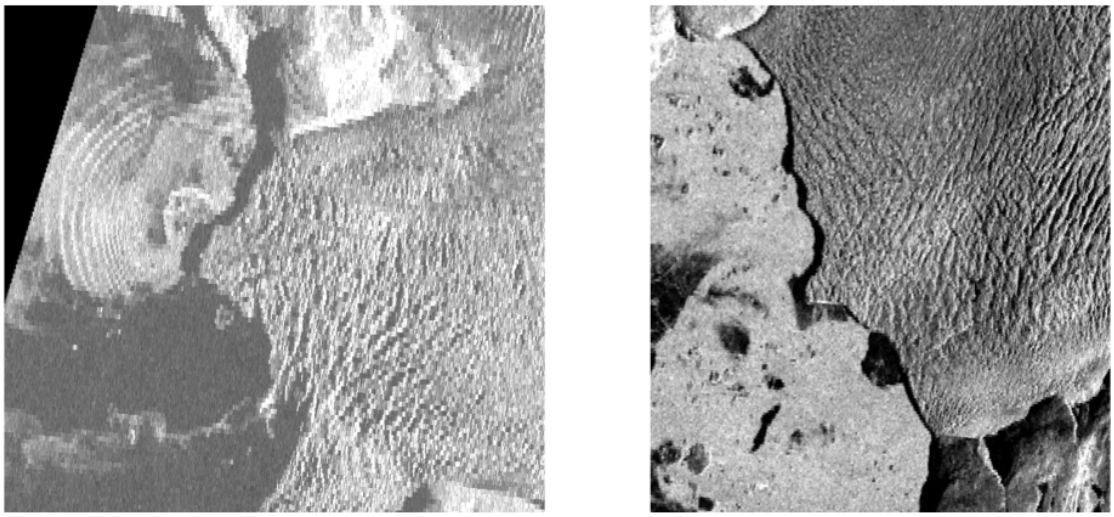

Figure 2.2: Calving events and a meltwater plume as observed from space using a SAR. A shows the waves coming from a recent calving event. B shows a meltwater plume that rises all the way up to the surface and clears the ice.

grounded) and the latter ends up in an ice shelf (floating). A marine-terminating glacier is also referred to as tidewater-glacier or calving glacier. Moreover, the different types of glaciers interact differently with external forcing, i.e., climate change. The glaciological concepts introduced in Section 2.1.1 can be applied on all glaciers, but this study focusses on marine-terminating outlet glaciers. For this study, we will focus on the concepts that are important for marine-terminating outlet glaciers, specifically the role of calving, external forcing and glacier-specific factors.

The vast majority of glaciers on the GrIS are marine-terminating (Moon et al., 2012). The future development of the GrIS mass-balance is dependent on the behaviour of these marine-terminating glaciers and their sensitivity to climate forcing. The definition of a marine-terminating glacier is an "outlet glacier as a channel of fast-moving ice that drains an ice cap or ice sheet and terminates in the ocean, at either a floating or grounded margin" (Carr et al., 2013a), meaning that they are not only influenced by air temperature, but also by sea temperature and seasonal ice concentrations.

CALVING

Marine-terminating glaciers differentiate from land glaciers as they have high calving rates. This holds that the calving C in Equation 2.2 is high, and that even with a positive SMB B_s a glacier can have a negative mass balance. Ice discharge is considered to be a dominating mechanism in the mass loss of the existing ice-sheets, and might have been responsible for the retreat of the Northern ice sheets during the last deglaciation (Nick, 2006). Calving events were also captured in SAR-images, as one can see in Figure 2.2.

The calving flux is defined as the volume of ice that breaks off per unit time and per unit vertical area of the terminus (Paterson, 1994). From observations, it is shown that water depth is an important factor for the calving rate. Glaciers with a shallow terminus show less calving compared to glaciers ending in deep water. Nick (2006) modelled calving is dependent on water depth d, ice thickness at the glaciers front H_f and the calving sensitivity c:

$$\dot{C} = -cdH_f. \tag{2.4}$$

The unit of $\dot{C}$ is m^2/ yr, and thus the calving sensitivity c represents the inverse of time (yr^{-1}). The calving flux $\dot{C}$ is directly related to the calving rate C when integrated over the width of a glacier, and converting the volume to mass using the ice density ρ_{ice}. Therefore, the processes influencing $\dot{C}$ can be directly related to C:

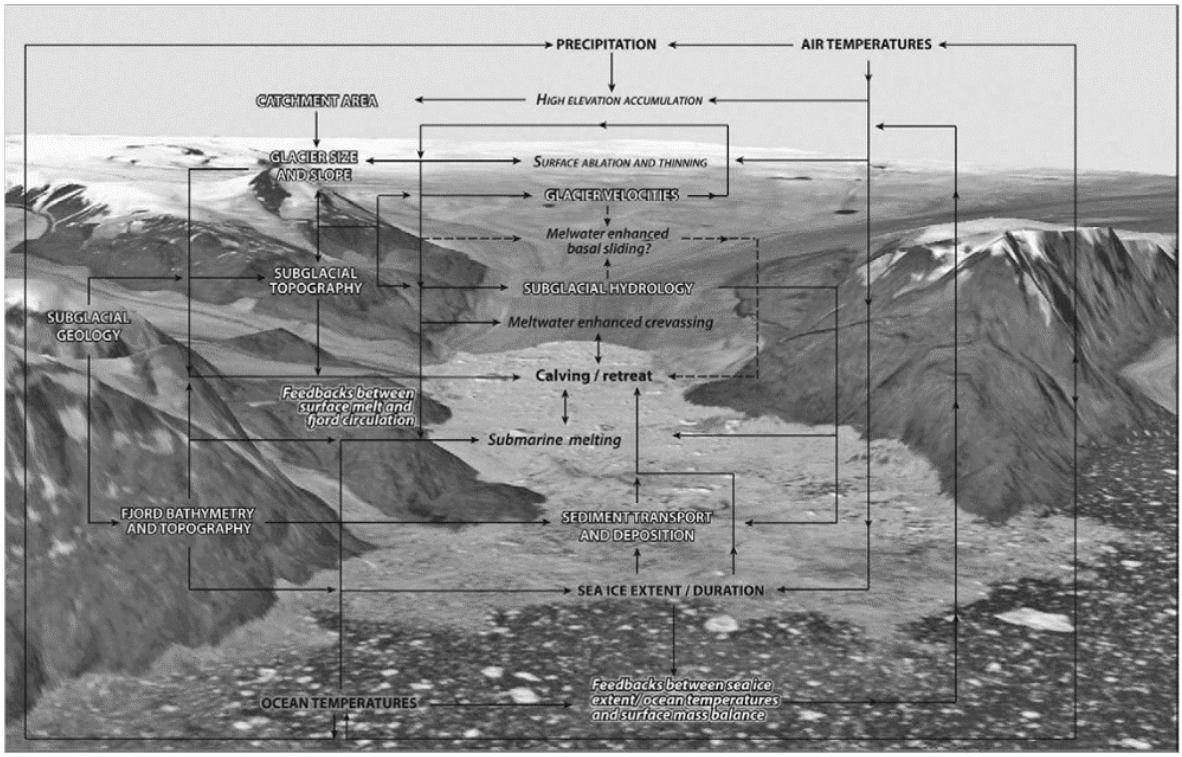

Figure 2.3: Overview of forcing factors induced by climate (black CAPS) and glacier specific controls (white CAPS). In italic the major processes (black) and feedback mechanisms (white) are noted (Carr et al., 2013a).

$$C = \rho_{ice} \int_{width} -cdH_f dx \tag{2.5}$$

The calving sensitivity c is an important parameter for a glacier, as it reflects the sensitivity to calve. How c is exactly influenced remains a question with the current understanding of calving, but on a generic level it is suggested to be combination between the flux and the mechanical properties of the ice (Nick, 2006, Nick et al., 2010). The flux determines the amount of ice that is supplied to the terminus, meaning that a higher flux meaning that more ice is available to calve. The mechanical properties are complex to capture, but it should represent the strength of the ice to avoid ice breaking off. Mechanically, calving is related to the stress at the terminus, if that exceeds the yield stress, the ice will break. Many processes can influence this, deep crevasses will lead to higher stresses for example, and additional stresses occur if there is water in the crevasses. Geometric effects also play are role: a wider and/or thinner terminus is likely to have higher lateral stresses, and thus calving is expected to increase. The presence of sea ice will reduce longitudinal stresses, thereby decreasing the calving sensitivity. All these aspects are represented by the calving sensitivity c, and this is an important parameter that is still poorly understood in glacier models. An attempt to model the calving sensitivity has been performed by Nick et al. (2010) and Morlighem et al. (2016), but they are still generic approaches that do not capture the complete calving processes, such as the influence of crevasses and buttressing.

EXTERNAL FORCING

A marine-terminating outlet glacier loses mass through by runoff (melt) or by calving. The influence of climate forcing on these processing is important to understand the future evolution of marine-terminating outlet glaciers. The interaction of marine-terminating glaciers with climate forcing is mainly governed by three external forcing variables:

- Surface Air Temperature (SAT).
- Sea Ice Fraction (SIF).

- Ocean Temperature (OT), here it will be differentiated into:
  - Sea Surface Temperature (SST),
  - Deep Ocean Temperature (DOT).

Their relative importance is different for each glacier, meaning that each glacier responds differently to climate change. In this study, we will focus on Surface Air Temperature (SAT), Sea Ice Fraction (SIF) and Sea Surface Temperature (SST). In Figure 2.3 it can be seen that these variables are connected to various physical processes in and around a glacier, and that they also interact with each other through various feedback mechanisms, i.e. a warmer SST and SAT leads to a reduction in SIF.

Surface Air Temperature (SAT) has an important role in the SMB, and controls the availability of meltwater. A higher SAT will lead to a higher ELA, thereby increasing the ablation zone. Meltwater is formed at the ablation zones and will drain its way to the glacier basin. At the glacier basin a channel system is formed by the water (see Figure 2.4), that initially is inefficient, leading to pressure below the glacier causing the water to act like a lubricant. This causes surface uplift, reduces basal stresses and, following from equation 2.3, leads to high glacier velocities (up to a 200 % increase (Moon et al., 2014)). Depending on topography and meltwater availability, the system can become efficient when the channel system ends in the ocean and the water can flow away. Pressure will then drop and the glacier will slow down. This effect has been observed at several glaciers, and is an important control in a glaciers flow velocity (Moon et al., 2014).

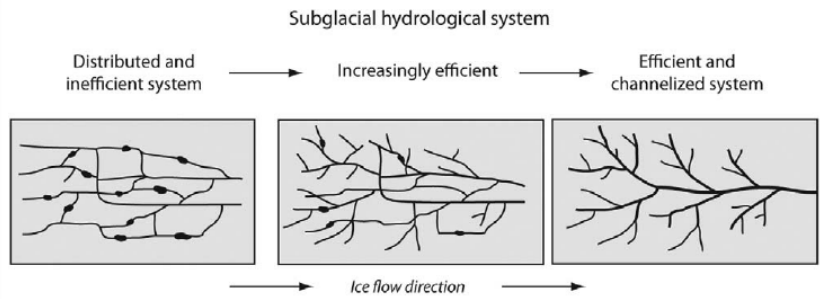

Figure 2.4: Overview of subglacial hydrology. Left is the tunnel system that a glacier has in its winter period, and under the influence of meltwater availability the system will evolve during spring and summer to a potentially efficient system. In an inefficient system the meltwater is trapped under the glacier. Consequently, it will act like a lubricant and allows a glacier speed-up. The efficient system does not necessarily have to form each year (Carr et al., 2013a).

However, the effect of meltwater on interannual behaviour may be limited and of secondary importance to fast flowing outlet glaciers (Carr et al., 2013b, Nick et al., 2010).

Sea Ice Fraction (SIF) influences the behaviour of a marine-terminating outlet glacier by controlling the calving sensitivity. In this study, both sea ice (frozen sea) and sea ice melange (icebergs frozen in the fjord) are considered together by SIF. High concentrations of SIF are suggested to provide buttressing, exerting a small force on the terminus of the glacier, thereby decreasing stresses at a glaciers terminus and reducing calving. This effect is illustrated in Figure 2.5. High concentrations of sea ice are only found during winter and spring periods, and the duration of this period is mainly influenced by sea and air temperature. Terminus advance only happens when there is enough buttressing, and is commonly observed in winter and early spring (Howat et al., 2010). Buttressing also decreases glacier flow speed as it acts an additional resistive force, i.e., increasing the force induced by longitudinal stress gradients (Equation 2.3). Støre Gletscher has been found to show a 14 % speed-up after clearance of the sea ice (Walter et al., 2012). Although SIF are considered to be small forces, their seasonal presence is suggested to be the difference between a positive or negative MB.

Long-term changes in their seasonal presence are suggested to influence the long-term evolution of marine-terminating outlet glaciers. When the terminus advance in winter periods is smaller than the terminus retreat in spring, a glacier will show long-term retreat. SIF is therefore considered to influence both seasonal as well as long-term evolution (Carr et al., 2013a).

The role Ocean Temperature (OT) on the evolution of marine-terminating glaciers is not completely clear in literature. It is one of the components that has not reached the level of understanding to allow realistic

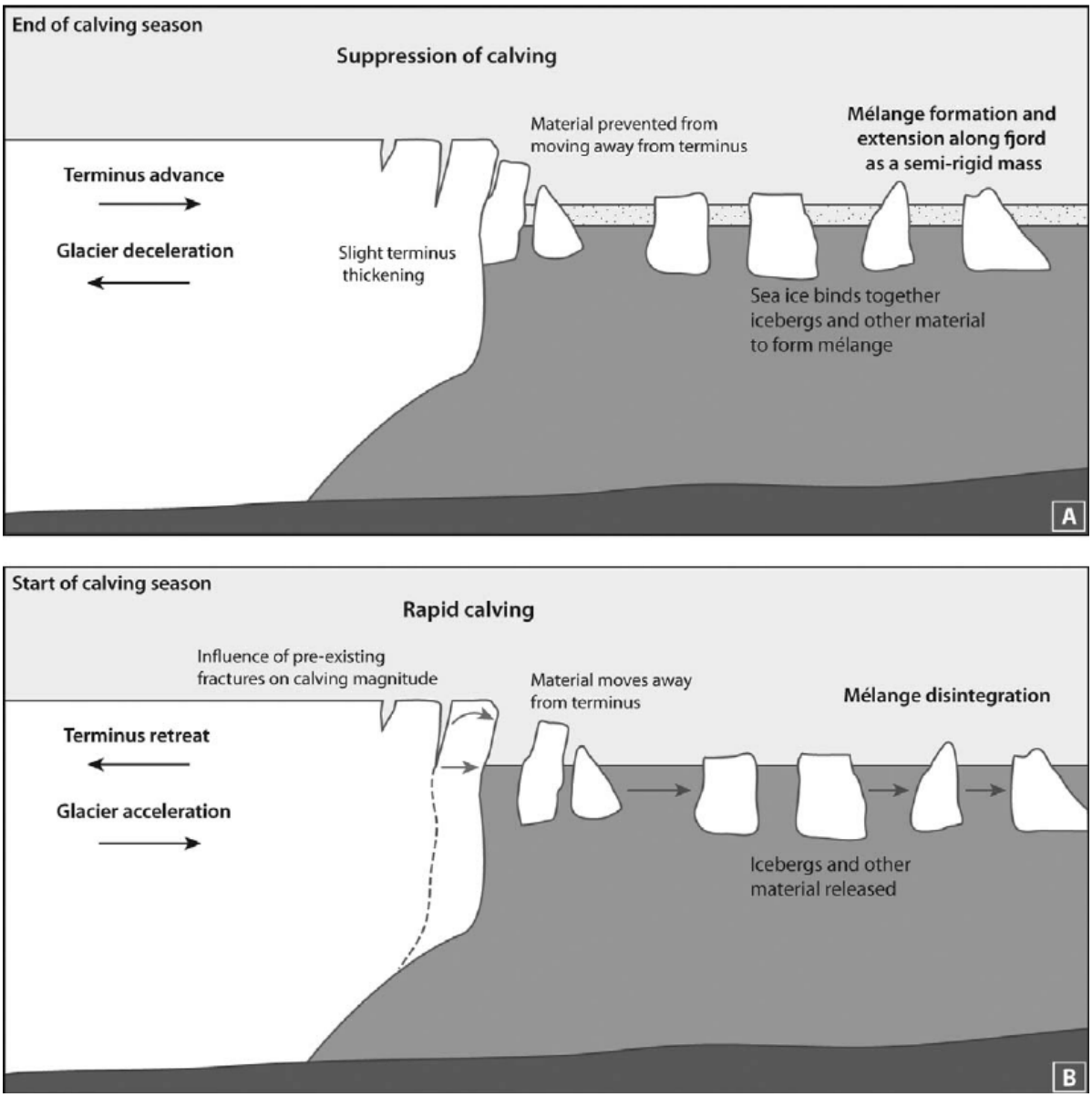

Figure 2.5: An illustration of the formation of sea ice melange. In A) the sea ice has formed and icebergs are frozen in the ice. In situation, the sea-ice melange provides buttressing, thereby reducing calving rates and slowing down the glaciers. In B) the sea ice has vanished, and there is no buttressing. (Carr et al., 2013a).

predictions (Bamber et al., 2007). This is mainly due to the fact that accurate oceanic observations at glaciers are missing. Four mechanisms in the interaction of oceanic forcing on outlet glaciers are identified: submarine melting and thinning of floating sections, grounding line retreat, alternation of calving front geometry at grounding line and SIF loss due to warming (Carr et al., 2013a). The latter influences the seasonal evolution of glaciers and can be properly observed, but the other mechanisms are difficult to assess due to the fact that it happens subsurface, at the grounding line. The absence of subsurface observations means that most studies use Sea Surface Temperatures (SST) (Moon et al., 2014, Moon et al., 2015) to represent oceanic forcing.

The relative importance of submarine melting on glacier evolution is poorly understood, but potentially very big. Observations have shown that oceanic forcing acts as an important form of ice ablation, potentially in the order of hundreds of meters in one summer, although varying significantly from one fjord to the next (Rignot et al., 2010, Rignot et al., 2015). Observations in East-Greenland have shown that there is a distinct difference in glacier evolution for glaciers in warmer and in colder waters (Seale et al., 2011). Three distinct water layers, Atlantic Water, Polar Water, Subglacial Fresh Water, and three mixed water layers, Mixed Water, Plume Water and Surface Water, are identified to be present in the Uummannaq-region (citeauthor-

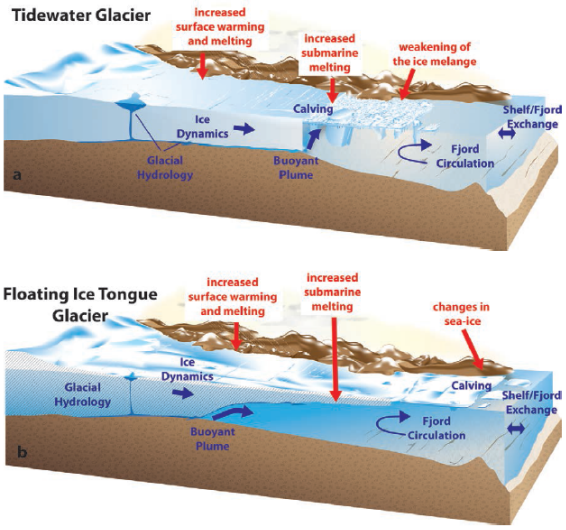

Figure 2.6: Two types of termini. The terminus of type A is connected to the grounding line, the terminus of type B has a floating tongue (Straneo et al., 2013).

Chauche2014, 2014). It is suggested that the Atlantic Water (AW), warm ($> 2.5°C$), salty, subsurface water originating from the tropics, have triggered a large number of glaciers to retreat (Rignot et al., 2016). The AW can be found below 250 m, covered by cold ($< 1°C$) Polar Water (PW) and potentially Mixed Water (MW) from submarine melting. As these waters originate from the ocean, their temperature is denoted as Deep Ocean Temperature (DOT). Based on these studies, here it is argued that that Equation 2.2 should be extended for marine-terminating glaciers:

$$B_s + C + B_o = 0, \tag{2.6}$$

where B_o is the Oceanic Mass Balance (OMB). Due to the lack of continuous sub-surface observations and the poor understanding of subsurface processes it is very hard to quantify the OMB.

There is an interesting feedback between meltwater and submarine melting, as meltwater can induce fjord circulation. An outflow of fresh meltwater leads to buoyancy driven circulation in the fjord, introducing convection driven melting at the grounding line and forced convection that drives the inflow of deep, warm ocean waters. This process has a major impact on melting at the grounding line, and therefore meltwater is likely to result in summertime melting near the grounding line, regardless of ambient seawater temperature (Rignot et al., 2010, Carr et al., 2013b, Jenkins, 2011). The relative importance of these processes to the long-term evolution remains unclear, and suggested to be different for each glacier (Carr et al., 2013a).

Sea Surface Temperature (SST) are suggested to mainly influence SIF, and consequently they influence terminus behaviour. Surface waters are covering the top 15 meters, and consists of a mix of polar waters and meltwater that is also influenced by solar insolation and atmospheric melting (Chauché et al., 2014).

In this study, data will be presented of Surface Air Temperatures, Sea Ice Fraction and Sea Surface Temperature. It is chosen to use Sea Surface Temperature (SST), and not Deep Ocean Temperature (DOT) as there is simply no proper long-term record of these temperatures, but also because DOT influences subsurface processes which are not observed with SAR.

GLACIER-SPECIFIC FACTORS

The processes that influence a marine-terminating outlet glaciers have been discussed, as well as their relation to climate forcing. However, the role of that climatic forcing variables have on the evolution of marine-terminating glaciers is different for each glacier. Glacier-specific factors, such as fjord topography, fjord bathymetry, terminus type, etc, are suggested to control the influence of climate forcing on the glaciological processes (Carr et al., 2013a).

The terminus type, grounded or floating, influences the sensitivity to calving (see Figure 2.6). Floating termini are more sensitive to subglacial melt and, under influence of increased stresses, calving events are

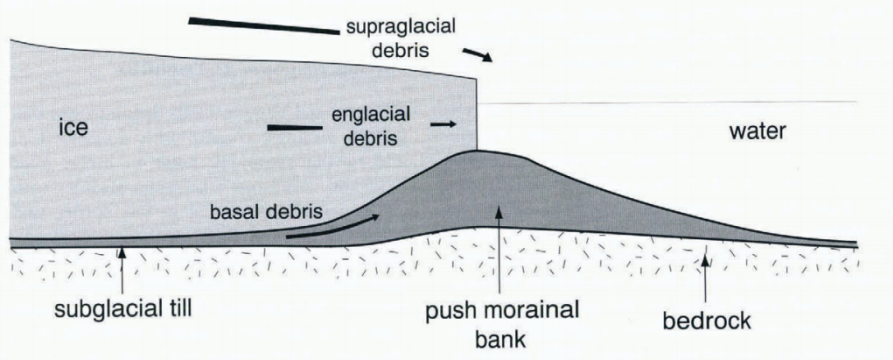

Figure 2.7: An overview of the terminal moraine shoal that is formed by sediment transport at the glacier bed. The terminal moraine shoal acts like a sill, and acts a resistive force on the glacier. An advancing glacier has to push the terminal moraine shoal ahead, like a bulldozer Fischer and Powell (1998).

more likely to occur. Grounded termini are regarded less sensitive, but under influence of oceanic forcing the grounded line can retreat and the terminus can become a floating terminus. In practice, many glaciers have an intermediate terminus type, and it is hard to classify glaciers as completely grounded or completely floating. In addition, it is hard to determine which terminus type a glacier has using SAR images. A bathymetric survey by (Rignot et al., 2015) showed that Rink Isbræ and Støre Gletscher have no typical floating tongue, but a seasonal tongue can be formed.

Another important aspect of the stability of a glacier to external forcing (SST, SAT, SIF) depends on the fjord topography. Carr et al. (2013b) found that for a region in Northwest Greenland the behaviour of specific glaciers is mainly influenced by their topographic situation. A narrow fjord width relaxes lateral stresses, that will lead to a reduced calving sensitivity c and thus leads to a relatively stable MB. Similarly, a shallow fjord lowers the calving flux according to equation 2.5. Glacier terminus retreat is therefore observed to be stepwise, from narrow section to narrow section.

Fjord bathymetry is considered to be an important control on the long-term evolution of a marine-terminating glacier. Most marine-terminating glaciers form a terminal moraine shoal by sediment deposit at its terminus location (illustrated in Figure 2.7), thereby creating a stable position in the fjord by decreasing the calving flux ($B_s + C = 0$). During a period with a high SMB or a low calving flux ($B_s + C > 0$), the glacier is able to advance slowly, thereby pushing its moraine shoal (Powell, 1990) in front of its terminus. In this situation, it can sustain relatively low calving flux until it advances to a position where it remains in equilibrium. If at some point the SMB decreases or the calving sensitivity c increase, the glacier may leave it's equilibrium ($B_s + C < 0$), followed by a retreat into deeper waters where it's calving flux is increased even more. This positive feedback enhances rapid retreat (Nick, 2006). Consequently, marine-terminating glaciers have observed to be either slowly advancing or rapidly retreating (Post, 1975, Meier and Post, 1987).

Where a retreating land-terminating glacier will re-advance the moment the SMB becomes positive again, a marine-terminating might not be able to due to its increased calving flux. On the contrary, the SMB might also become more negative during its rapid retreat. It is suggested by Fischer and Powell (1998) that the terminal moraine shoal also provides a restraining force (basal) against glacier flow. As can be seen in Equation 2.3, a decrease in basal resistive forcing will cause a glacier to accelerate. An increase in velocity will lead to thinning (Van der Veen, 2013), that will lead to a larger ablation area and that in turn lowers the SMB. Retreat of a marine-terminating glaciers leads to a lower SMB and a higher calving flux. Hence, variations in the mass budget can put a marine-terminating glacier in a positive feedback loop, that is irreversible until a new equilibrium position is found. This is confirmed by observations, which found that retreat of the terminus position leads to a decrease in restraining forces and can lead to a rapid speedup, as for example observed at Alison glacier where velocities increased up to 63 % (Carr et al., 2013b). In conclusion, the terminal moraine shoal facilitates a stable position of the terminus, but enhances rapid retreat when the terminus retreats from this position.

Carr et al. (2013b) also states that the magnitude of seasonal retreat is dependent on the forcing parameters during the summer period, but that the magnitude of interannual retreat is in particular influenced by

the topographic situation and not directly by forcing parameters. This is illustrated by the fact that Igdlugdlip Sermia terminus position was stable in a narrow fjord situation for several decades, but is expected to retreat rapidly as the inland fjord topography might facilitate this retreat. This behaviour is confirmed by Moon et al. (2015), as observations showed that meltwater is important for a glacier's seasonal behaviour, but interannual changes are imposed by terminus changes. These observations are in line with the expected behaviour according to the rapid retreat scenario described earlier, where retreat of marine-terminating glaciers imposes a positive feedback that, even during colder periods, is sustained until the calving C is small enough to balance the SMB (either by a reduced calving sensitivity c or a lower fjord depth d). Questions remain about how these patterns connect at different timescales and across different regions, and in what timescales glaciers are able to build a new marine shoal.

CLASSIFICATION OF SEASONAL BEHAVIOUR

As each glacier and its sensitivity to external forcing is unique, it is also expected that glaciers show a different seasonal behaviour. This is important to understand, because seasonal behaviour might have consequences on the long-term stability of a glacier.

The seasonal behaviour of glaciers can be divided into three classes (Moon et al., 2014): terminus controlled behaviour, meltwater driven without an efficient drainage system and meltwater driven with an efficient drainage system. The first type does not occur often on a regular basis, in contrary to the latter two. The latter two are closely connected, with the note that an efficient drainage system does not have to be formed each year. It was observed that in low-melt regions an inefficient system was sustained, leading to an early summer speed-up and relatively stable speeds the rest of the year. In high-melt regions the channel system became efficient, leading to a late summer minimum. One can see this as an negative feedback, where more meltwater does not lead to increased glacier velocities, but to a quicker formation of an efficient drainage system leading to reduced glacier velocities (Moon et al., 2014).

2.1.3. REGIONAL ASPECTS

The glaciological concepts of marine-terminating outlet glaciers have been introduced, and it has been discussed that marine-terminating glaciers are influenced by climate forcing, and that glacier-specific factors are controlling this influence. However, most studies performed on GrIS outlet glaciers are mainly focussed on a small number of large glaciers (Jakobshavn Isbrae, Hellheim, Petermann). The conclusions and relations found on those glaciers should not be extrapolated to all GrIS glaciers without studying more glaciers and during a longer time-span (Carr et al., 2013a). The aim of this study is to study more glaciers during a longer time-span, and to identify which factors play a role in their different sensitivity to climate forcing.

Therefore, it is especially interesting to compare seasonal and long-term behaviour of glaciers which are subject to approximately the same climate forcing, over a prolonged period of time. For this thesis the Uummannaq region is considered, a shielded fjord system in west-Greenland that is connected to Baffin Bay with a 50 km channel. It came to its name by the little village, Uummannaq, that is build on a rock in the middle of the fjord system. This region has been chosen for the research of because of its data availability and the shielded topographic situation. There is much data coverage from 1992-2014 over this region, and also SST, SAT and SIF data is available. Next to this, the shielded fjord system makes that SAT, SIF and SST can be considered approximately the same over the region, making it possible to compare the behaviour between glaciers under the same climate forcing. Ten Glaicers can be found in this region, as depicted in Figure 2.9, of which Støre glacier and Rink Isbræ are the largest and most observed. Based on data availability it is chosen to study 7 of the 10 glaciers, including the fast flowing Støre glacier and Rink Isbræ.

In Figure 2.8 the yearly discharge of the Greenlandic glaciers is given, which shows that the the 15 largest glaciers are responsible for 50% of the cumulative discharge for the GrIS. Two of the glaciers in the Uummannaq-region, Støre glacier and Rink Isbræ, can be found in the top 15.

The largest and most studied glacier of the GrIS, Jakobshavn, is only 100 km South of Støre Gletscher. It showed a rapid retreat and acceleration after the breakup of its floating tongue. As this glacier is close to the region of interest, it is interesting to understand when, why and how it retreated. It was observed that it retreated 20 km after the Little Ice Age (that lasted until 1850) until it found a stable position around 1950. In 1997 the 15 km long floating tongue started to collapse and in 2004 it was completely dissolved (Nick et al., 2010). During this period the glacier accelerated from 6 km/yr to 13 km/yr, and the speed-up has observed to propagate inland together with sustained thinning. Many studies have been performed to understand the

rapid retreat of Jakobshavn (Nick et al., 2010). It is suggested that the collapse of the ice-tongue followed after a sharp decline of sea ice and due to oceanic forcing at it's grounding line (Joughin et al., 2008). The glaciers in the Uummannaq-region might have the potential to undergo a similar retreat and acceleration, and are therefore interesting to study.

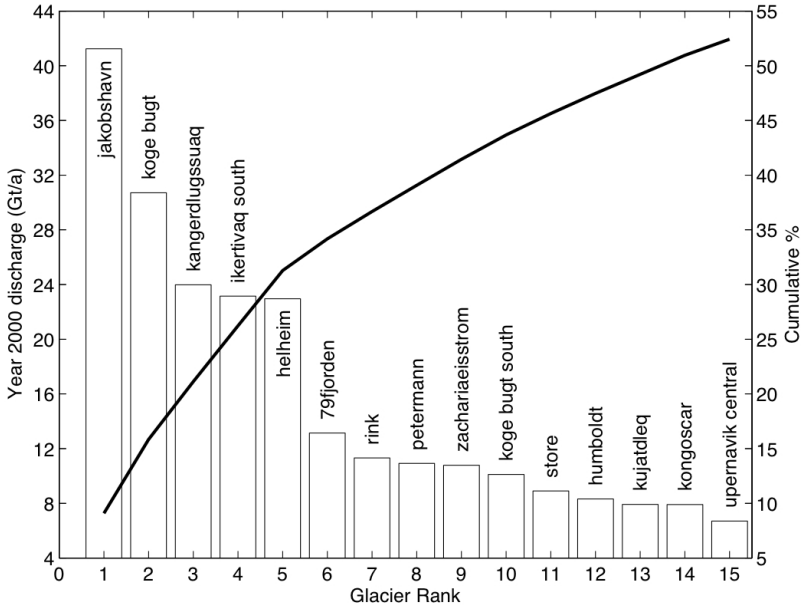

Figure 2.8: Overview of the yearly drainage in 2000 for the Greenlandic glaciers (Enderlin et al., 2014). Rink Isbræ and Støre Gletscher are among the top contributors to drainage.

Figure 2.9: Overview of the Uummannaq-region in West-Greenland. The red stars indicate glaciers that are considered in this study, the gray stars indicate glaciers that are not considered. The orange dots indicate the location of the DMI meteorological stations that are used.

PRIOR RESEARCH ON GLACIER BEHAVIOUR FOR THE STUDY AREA

The glaciers in the Uummannaq Bay have been examined before in various researches. Howat et al. (2010) also selected this region for his research in understanding seasonal variability between 2000-2009, using optical images. He selected six glaciers which had an ice front wider than 3 km, apart from Rink Isbræ and Støre glacier also Sermeq Silardleq, Kangerdlugssup Sermerssua, Umiamako and Ingia Isbræ were selected. Moon et al. (2014) also did observations for Rink Isbræ and Støre glacier, Sermeq Silardleq, Kangerdlugssup Sermerssua, and additionally also for Kangilleq Isbræ. She used TerraSAR-x images to estimate velocities between 2009 - 2013, and also classified the seasonal patterns as described in Section 2.1.2. Rignot and Mouginot (2012) made velocity estimations for 243 glaciers (wider than 1.5 km) in 2008 - 2009, among which the ten glaciers in Uummannaq were considered. Støre and Rink Isbræ were listed as the 5th and 6th fastest glacier in Greenland, although it in Figure 2.8 it can be seen that their discharge is less significant. The results of these studies for the Uummannaq region are listed in 2.1, and will be elaborated further more. For this study the same glaciers are selected as in Howat et al. (2010).

Inngia Isbræ and Umiammakku Isbræ showed stable front position and ice velocities between 1999 and 2003, but front positons retreated quickly between 2003 and 2009 and velocities increased (Howat et al., 2010). Rignot also analysed flow patterns on the GrIS, and identified 7 flow sectors. Remarkably, Inngia Isbræ and Umiammakku Isbræ are in the Northwest sector while the other glaciers are in the west area. This might have implications for meltwater availability from the ice sheet in comparison to the other glaciers.

Rink Isbræ and Kangerdlugssup Sermerssup show a large seasonal oscillations in both front position as in velocity, but no multi-year change was observed (Howat et al., 2010). In 2009, 2010, 2011 and 2012 Rink Isbræ was classified as terminus controlled, but in 2013 the glacier was classified to behave according to an efficient drainage system. (Moon et al., 2014).

Støre Glacier has been very stable for the last 40 years with a 200 m seasonal oscillation of the front position. Speeds were considered to be stable, but in 2002 and 2005 a sudden deceleration was observed. This deceleration was explained by lake drainage on 17 km inland of the glacier front, which must have led to a quick formation of an efficient drainage system Howat et al. (2010). This seems to be the main driver for this glacier, as it was classified to have an inefficient drainage system (2009, 2013) and an efficient drainage system (2012). The mean velocity between 2009 - 2013 was about 3824 m/yr with only 9% seasonal variation Moon et al. (2014).

Additional research has been performed on Støre by Todd and Christoffersen (2014) using a calving model. A Navier-Stoke simulation was run on the various forcing mechanisms, and it confirmed that terminus position and glacier flow velocity are highly correlated, and that buttressing pressure from the sea-ice melangé is key in seasonal advance and retreat (and confirmed by Walter et al. (2012)).

Table 2.1: Overview of the selected glaciers in the Uummannaq region for this study and the observed speeds from earlier researches. Velocities are given in m/yr.

Glacier	**Latitude**	**Longitude**	$\mathbf{v}_{\text{Rignot}}$	$\mathbf{v}_{\text{Howat}}$	$\mathbf{v}_{\text{Moon}}$	$\mathbf{amp}_{\text{Moon}}$
Inngia Isbræ	72.033	52.611	980	913	-	-
Rink Isbræ	71.759	51.606	4181	4015	4542	10 %
Umiammakku Isbræ	71.744	52.939	1281	1095	-	-
Kangerlussuup Sermersua	71.462	51.318	1649	1642	1763	45%
Sermilik	70.639	50.583	583	-	1483	21%
Lille Gletscher	70.523	50.525	471	-	-	-
Støre Gletscher	70.401	50.549	3678	3650	3824	9%

PRIOR RESEARCH ON FJORD CONDITIONS FOR THE STUDY AREA

The Uummannaq bay is connected to Baffin Bay by a deep channel of approximately 450 m depth (Jakobsson et al., 2012 and Dowdeswell et al., 2014), which provides a direct route to Atlantic Waters (AW) to the fjord (see Figure 2.10 and 2.11).

The subsurface melting process, as described by Jenkins (2011) and Rignot and Mouginot (2012), was observed in at Rink Isbræ and Støre as well by Rignot et al. (2015). It was found that deep, warm Atlantic water was present below 200-250 m and was driving submarine melting at both glaciers. Rignot et al. (2016) performed a bathymetric survey in the Uummannaq Bay, and concluded that fjord conditions vary significantly from fjord to fjord. Some glaciers are located in deep fjords, allowing warm, salty AW to be in contact with

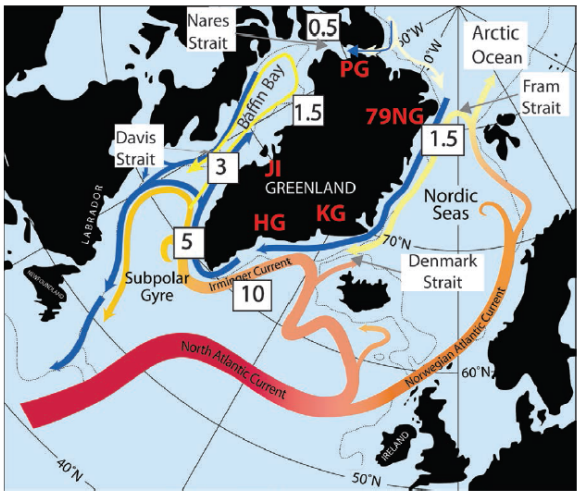

Figure 2.10: The Atlantic ocean currents around Greenland. The numbers indicate the ocean temperature (Straneo et al., 2013).

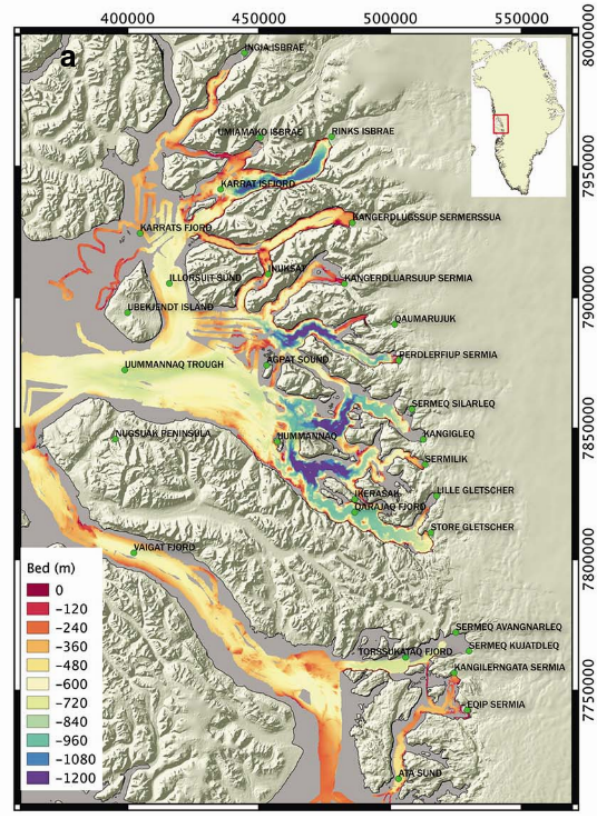

Figure 2.11: The connection of the Uummannaq Bay to the Atlantic Waters and the bathymetry in the fjord obtained from multibeam echo sounding data. It can be seen that the fjord in the South are generally deeper than the fjords in the North. (Rignot et al., 2016)

the glaciers fronts, but some glaciers are located in shallow fjords (> 200m) and are only in contact with PW. Glaciers in contact with AW did not show any retreat, but some shallow glaciers were found to retreat. In the research by Rignot et al. (2015) it became clear that Støre Gletscher only has a periodical floating tongue and that Rink Isbræ has a small floating section. For the other glaciers it is unknown if they have a grounded or floating terminus. Todd and Christoffersen (2014) performed a stability analysis that lead to the conclusion that glacier advance will be limited in a warmer climate, and that submarine melting has a limited effect on Støre. The glacier is very stable due to the front position in a 'bottleneck', but once that position is lost, a rapid retreat of 28 km is predicted due to a wide and deep fjord situation.

This was mainly induced by the forced convection mechanism, allowing inflow of these warmer waters. As Rink Isbræ is deeper (approx 750 m) than Støre Gletscher (500 m), the, a larger portion (approx 75%) of the ice front is affected by submarine melting compared to Støre (approx 40%). This has implications for the calving face, which is flat at Rink Isbræ and crenulated at Støre. Another important effect mentioned by Chauché et al. (2014), is that the height of the convection plume is influenced by the amount of runoff. If there a high runoff, the plume becomes visible at the surface as can be seen in Figure 2.2.

2.2. REMOTE SENSING WITH SAR

In this study, images made by a Synthetic Aperture Radar are used to observe glacier behaviour. Synthetic Aperture Radar (SAR) is an imaging radar system that both emits and receives radio waves, and uses a side-looking antenna to illuminate the Earth surface (Hanssen, 2001). A SAR acquires both the amplitude as well as the phase of the backscattered signal, making it a coherent radar. SAR images are used for many applications, and have shown to be useful for glaciology (Joughin et al., 2010b). Although both amplitude and phase can be used for glaciological applications (Joughin et al., 2010b), in this study only the amplitude is considered due to a limited availability of stable-phase images.

A big advantage of SAR is that it can penetrate clouds and it is not bound to daylight conditions. In this project, this aspect has been key for the decision to use SAR remote sensing to observe the area of interest, as its northern location implicates that daylight is absent during winter.

In this section the remote sensing principles of SAR, relevant for this study, are elaborated. First in Section 2.2.1, a theoretical description of the SAR backscatter properties is given. In Section 2.2.2 an overview is given of the available data and in in Section 2.2.3 an overview is given of SAR processing.

2.2.1. SAR BACKSCATTER

A SAR system observes the reflections from a scene on the Earth's surface. As amplitude SAR images are used in this study, it is important to understand this process. In a natural scene, i.e., mountains, water, snow, ice, there is no single scatterer that dominates a resolution cell, hence a pixel is the combination of many scatterers that are referred to as distributed or partial scatterers (Ogilvy and Ogilvy, 1991, Beckmann and Spizzichino, 1987, Ferretti et al., 2007, Hanssen, 2001). In this case, the reflected signal for each resolution cell is the combined reflection of all the independent scatterers within this resolution cell. As the detailed structure of a scatterer is not known, its properties can only be described statistically. The physical processes behind these scatterers are mainly due to surface or volume scattering, meaning that scattering occurs when an EM wave reaches a surface, or by dielectric discontinuities in a volume(Ulaby et al., 1986, Martınez, 2003).

An image pixel can be described as the summation of many independent scatterers (Beckmann and Spizzichino, 1987). Consider the signal z_i of an individual scatterer:

$$z_i = Ae^{i\phi}, \tag{2.7}$$

where A denotes the amplitude and ϕ the phase. The received signal at the SAR system for each resolution cell is the summation of each individual scatterer (Beckmann and Spizzichino, 1987):

$$z = \sum_{k=1}^{N} A_k e^{i\phi_k}. \tag{2.8}$$

The complex signal can be described by a real part x and a imaginary part y:

$$z = x + iy, \tag{2.9}$$

or:

$$z = \sum_{k=1}^{N} A_k \cos(\phi_k) + i \sum_{k=1}^{N} A_k \sin(\phi_k). \tag{2.10}$$

The statistics of x and y satisfy the Central Limit Theorem and converge to a real valued, zero-mean, Gaussian probability density function (pdf). This only holds under these assumptions (Hanssen, 2001):

- **No dominant scatterer exists**, which generally holds for natural scatterers.

- **The phase of every individual scatterer is uniformly distributed**, which holds as a resolution cell is much larger than the wavelength.
- **The phases of the individual scatterers are uncorrelated**, which should hold as correlated scatterers have different scatter centers.
- **The amplitude and phase of every scatterer must be uncorrelated**, which can be assumed because the phase delay is independent of the scattering magnitude.

This means that the expectation value of x and y is zero:

$$E\{x\} = \sum_{k=1}^{N} E\{A_k \cos(\phi_k)\} = 0, \tag{2.11a}$$

$$E\{y\} = \sum_{k=1}^{N} E\{A_k \sin(\phi_k)\} = 0, \tag{2.11b}$$

and therefore:

$$E\{z\} = \sum_{k=1}^{N} E\{A_k \cos(\phi_k)\} + i \sum_{k=1}^{N} E\{A_k \sin(\phi_k)\} = 0. \tag{2.12}$$

Using the assumption that the sum of the real part x and imaginary part y are uncorrelated and have the same variance, the behaviour of the complex signal z is then defined as a circular Gaussian distribution, visualized as a two-dimensional random walk in Figure 2.12, with an expectation value of zero. The variance of the signal is dependent on the nature of the scatterers (Beckmann and Spizzichino, 1987):

$$D\{x\} = \sum_{k=1}^{N} D\{A_k\} E\{\cos^2(\phi_k)\} = \frac{N}{2} D\{A\}, \tag{2.13a}$$

$$D\{y\} = \sum_{k=1}^{N} D\{A_k\} E\{\sin^2(\phi_k)\} = \frac{N}{2} D\{A\}. \tag{2.13b}$$

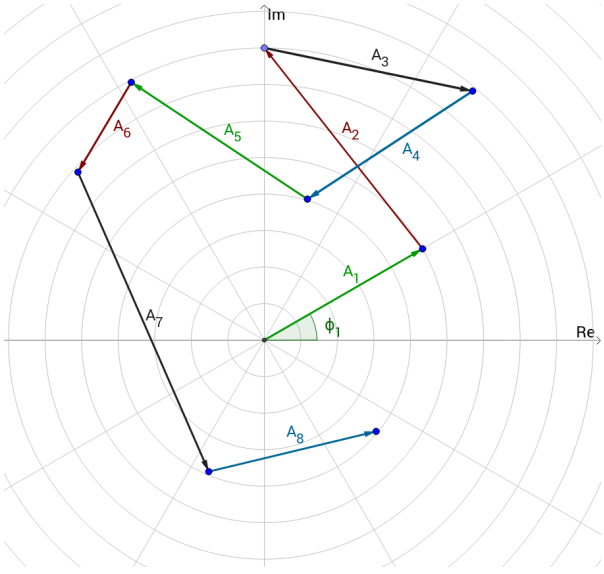

Figure 2.12: Random Walk within a SAR pixel. The length of the arrows denote the amplitude A and the angle is the phase ϕ. The summation of the different scatterers, coherent superposition, can be seen as a random walk in a 2D space.

The variance is defined as $\sigma^2 = \frac{N}{2} D\{A\}$. The variance of the complex signal z can be rewritten as:

$$E\{|z|^2\} = E\{x^2\} + E\{y^2\} = 2\sigma^2. \tag{2.14}$$

And the pdf of the complex signal z can be described by (Beckmann and Spizzichino, 1987):

$$\text{pdf}(x,y) = \frac{1}{2\pi\sigma^2}\exp^{\frac{-(x^2+y^2)}{2\sigma^2}}. \tag{2.15}$$

This pdf describes the signal for a complex sum, but in this form it does not relate to any physical process. The amplitude and phase are described by:

$$A = \sqrt{x^2+y^2}, \tag{2.16a}$$

$$\phi = \arctan2(y/x). \tag{2.16b}$$

Using these relations the pdf of the complex signal can be described as a function of phase and amplitude (Hanssen, 2001):

$$\text{pdf}(A,\phi) = \frac{A}{2\pi\sigma^2}\exp^{-\frac{A^2}{2\sigma^2}}. \tag{2.17}$$

And the marginal pdf's of the amplitude and phase are then (Hanssen, 2001):

$$\text{pdf}(A) = \frac{A}{\sigma^2}\exp^{-\frac{A^2}{2\sigma^2}}, \tag{2.18a}$$

$$\text{pdf}(\phi) = \frac{1}{2\pi}. \tag{2.18b}$$

From these equations it can be stated that the amplitude follows a Rayleigh distribution and the phase is uniformly distributed. The latter is an important conclusion as it shows that the phase of a scatterer does not contain information about the scatterer, and can be regarded independent (Martınez, 2003). When considering the intensity ($I = A^2$), equation 2.18a can be rewritten to:

$$\text{pdf}(I) = \frac{1}{2\sigma^2}\exp^{-\frac{I}{2\sigma^2}}, \tag{2.19}$$

which is an exponential distribution, with a mean value of $E\{I\} = \sigma^2$ and a variance of σ. The variance σ is dependent on the incidence angle and the normalized radar cross section, defined as the fraction of the intensity intercepted and returned (Bamler and Hartl, 1998, Hanssen, 2001). In turn, normalized radar cross section is affected by moist content (i.e., electrical properties of the soil) and surface geometry (i.e., roughness, slope). Consequently, the variance of the amplitude is mainly influenced by the properties of the terrain.

In Figure 2.13 an overview is given of the pdf functions for different types of terrain. It can clearly be seen that a 'dark' terrain type leads to pixels with a low amplitude, while a 'bright' pixel can have amplitude values ranging from low to high. This means that the amplitude of a reflective terrain-type leads to a higher amplitude variance. The relevance for this project is the difference between wet and dry snow, as wet snow has a lower reflectivity than dry snow. A transition from dry to wet snow is therefore likely to influence the amplitude tracking results. The principle between different types of snow in relation to the reflected amplitude is discussed in Section 2.3.2.

The amplitude variations of an image, as described by the pdf, are known as 'speckle' (Hanssen, 2001). This implies that pixels with the same terrain cover will lead to different amplitude reflections. Speckle is regarded as noise in some studies, but the speckle pattern contains information about the subresolution structure of the reflection and in this study that is an important source of information (Bamler and Hartl, 1998). Although it is a random process, speckle patterns are correlated in time and can therefore be used for estimating cross-correlations (Joughin et al., 2010b).

2.2.2. MISSIONS AND DATA

The first European spaceborn SAR was mounted on the European Remote Sensing satellites (ERS-1 and ERS-2) that were launched at the early 90's and mid 90's, respectively. Many successors were launched after, such as Envisat, ALOS, RadarSAT-1 and 2, TerraSAR-X, and the recently launched Sentinel-1 (ESA). The radar frequency they are operating on differs from mission to mission meaning that they will observe different backscattering. Next to this, they also feature different properties such as resolution and swath-width.

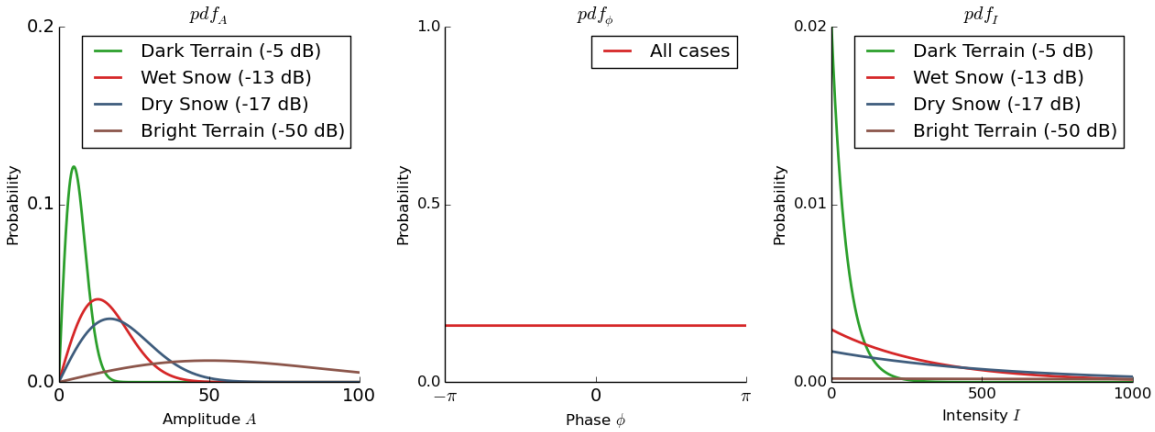

Figure 2.13: PDF functions for phase, amplitude and intensity for different types of snow (Wilson et al., 2005). The dark and bright pixel values are arbitrary values, to highlight the difference of their pdf.

In this project, SLC data was acquired by ERS-1/2, EnviSAT and TerraSAR-X with observations ranging from the early 90's till the end of 2013. The satellite missions that are relevant for this project are listed with their characteristics in Table 2.2. Although launched and operational, Sentinel-1 images are not considered as more advanced processing is required because the images are acquired in a TOPS (Terrain Observation by Progessive Scanning) mode (Oost et al., 2015).

Table 2.2: Selected satellite missions (van Leijen, 2014). Δ az, Δ sr and Δ gr are the azimuth spacing, slant-range spacing and ground-range spacing, respectively. Δ T is the temporal baseline. * Orbital configuration between 14-Apr-1992 to 21-Dec-1993 and 21-Mar-1995 to 10-Mar-2000. During the overlapping periods of ERS-1 and ERS-2 they were in tandem phase (1 day difference).

Satellite	**Period**	**Frequency Band**	**Δ az [m]**	**Δ sr [m]**	**Δ gr [m]**	**Δ T [days]**	**Swath Width [km]**	**Orbit Height [km]**
ERS-1	1991 - 2000	C-Band	4	7.9	20.0	35*	100	785
ERS-2	1995 - 2011	C-Band	4	7.9	20.0	35	100	785
ENVISAT	2002 - 2010	C-Band	4	7.8	20.1	35	105	785
TerraSAR-X	2007 - present	X-Band	1.9	1.3	2.1	11	30	514

In Figures 2.14 and 2.15 an overview is given of the available frames and images used for this thesis. In total, 665 images (≈ 2 TB) were processed of which 76 images failed during coregistration (see Figure 2.16). The selected satellite missions feature different specifications which that might influence the results:

- **Temporal Baseline**, the time between two acquisitions, is important due to decorrelation, loss of similarity, of the glacier in time. Depending on a glaciers speed, decorrelation happens within days to months (Joughin et al., 2010b).
- **Image Resolution**, will influence the accuracy of the estimated glacier velocity and the accuracy of the digitization of the terminus (Gray et al., 2001).
- **Operating Band** influences the reflection as each wavelength is sensitive to other object sizes and properties. Another relevant aspect for glacier studies is the penetration depth, as this will influence where the backscattering comes from (Konig et al., 2001). A larger wavelength will penetrate deeper and will maintain a better temporal stability, but short wavelengths provide more information about the wetness and roughness on the surface (Konig et al., 2001, Floricioiu and Gottwald, 2008, Rignot et al., 2001).
- **Polarization**, the orientation of the electric field vector with respect to the propagation direction of waves, leads to different backscattering for different types of snow and ice. But as all images in this project are made in VV or HH (vertical and horizontal orientation), this aspect is not relevant (Xu et al., 2012, König et al., 2000).

The images of ERS and EnviSAT have comparable resolution, swath width and are made with C-band. TerraSAR-X images have a higher resolution, a smaller swath width and are made with X-band. This means

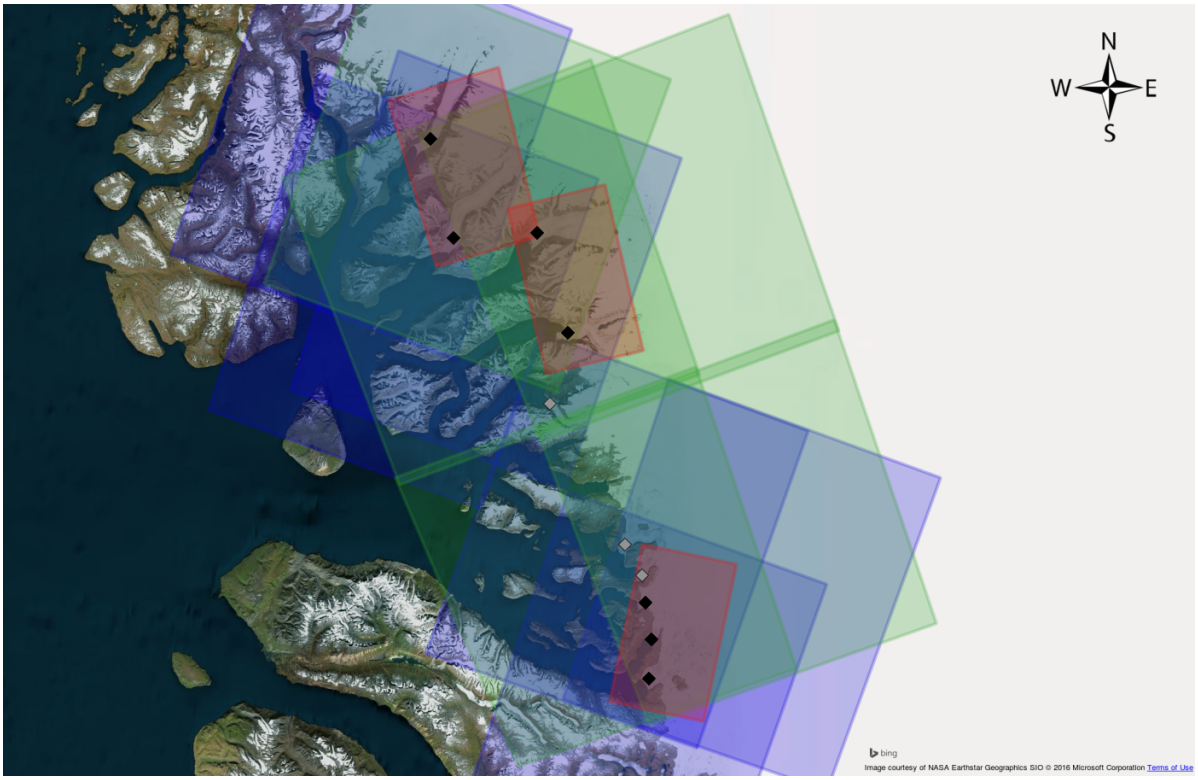

Figure 2.14: An overview of the frame locations and glaciers. The blue frames are made by ERS1/2, green frames are made by EnviSAT and red frames are made by TerraSAR-X. Black points indicate the glaciers studies in this thesis, gray points indicate glaciers that are not considered because they are not covered by TerraSAR-X. From North to South, the glaciers are Inngia Isbræ, Umiammakku Isbræ, Rink Isbræ, Kangerlussuup Sermersua, Sermilik, Lille Gletscher and Støre Gletscher.

that the amplitude of the images is different due to different backscatter properties. Fortunately, there is an overlap between the different missions, meaning that their estimates can be compared.

It should be noted that ERS-2, which operated until 2011, had a gyroscope failure in January 2001 meaning that its yaw angle could not be controlled. In Figure 2.17 an overview of the situation of the gyroscope is given with the corresponding orbital tube, where it can be seen that there is a 2 year period in which the satellite was in a significantly wider orbital tube. Using advanced orbital calculations a new yaw control mode (YCM) was introduced, where the mean yaw per orbit is used to control satellite yaw in the next orbit, that made it relatively stable (Miranda et al., 2003). In the processing, most coregistration problems were encountered during the first year after the gyroscope failure. The amplitude signal is a little degraded and for interferometric purposes the phase instability was too significant. The implications for this project are that the coregistration of these images requires more coregistration windows.

2.2.3. SAR IMAGE PRODUCTS

In order to make use of SAR images, several processing steps are applied. Raw SAR images that are acquired have to be focussed in order to obtain a Single Look Complex (SLC) image which is useful for (In)SAR processing. For this process the instrument properties have to be known in detail and this process is commonly done by the satellite operators themselves (ESA).

SLC products are images with complex information (amplitude and phase). Their 2D spacing is not based on ground range geometry but on slant range geometry (pixel: range to the scatterer, line: interval of observations in azimuth). This implies that there is varying ground range spacing between pixels. These products have to be coregistrated on top of each other to create a stack, a series of images, where each pixel is resampled to match the pixel in the other images. Normally this is done to an accuracy of 0.1 pixel for stripmap products (Scheiber et al., 2015). Coregistration can be done by image matching techniques and/or by geometric processing using a Digital Elevation Model (DEM).

For this project, also Ground Range Detection (GRD) images were needed for digitization of the terminus

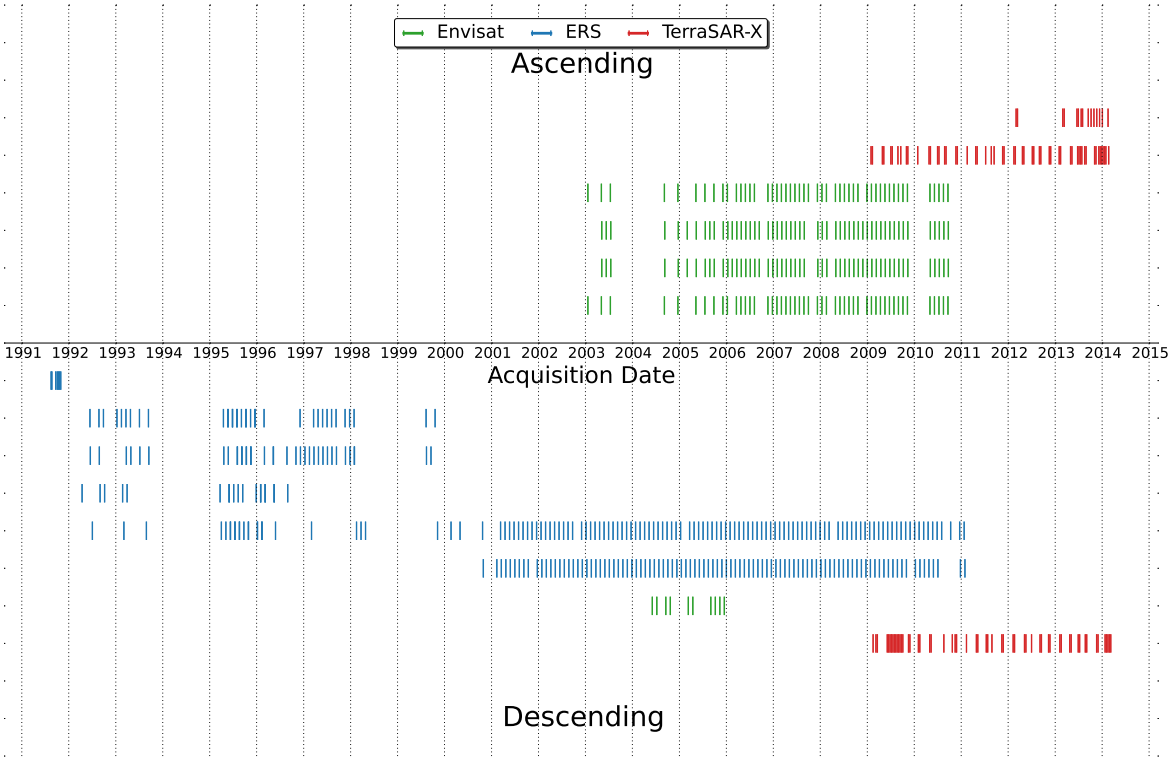

Figure 2.15: An overview of the available images in the project. The red images are made by TerraSAR-X, green images are made by EnviSAT and blue images are made by ERS1/2. The upper part ones shows the ascending images and the lower part shows the descending images.

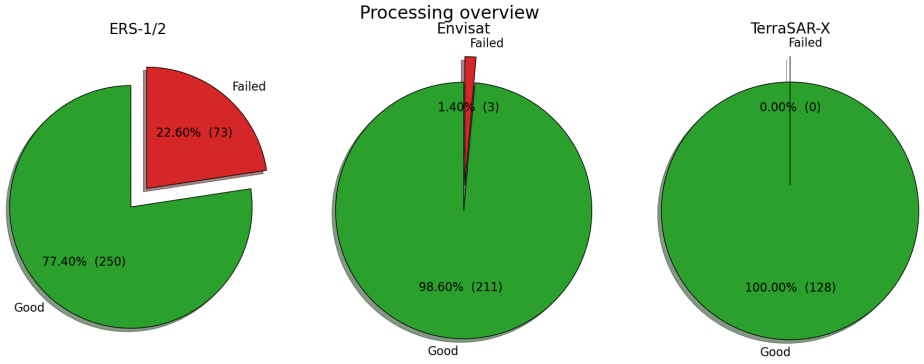

Figure 2.16: An overview of the successful and failed images during the project. All failed images failed during coregistration. Most images that failed were ERS-1/2 images, and this was due to the gyroscope failure. One stack was discarded (15 images) because no proper geocoding could be performed.

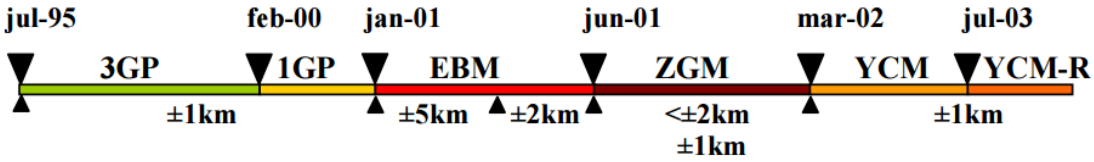

Figure 2.17: Configuration of the ERS-2 piloting modes and corresponding orbit dead-band evoluation (Miranda et al., 2003).

line. Here the amplitude information is geocoded based on a DEM and reprojected on a equidistant grid.

2.3. GLACIOLOGICAL OBSERVATION WITH SAR

In this section the observations of glaciers and ice-caps using SAR are described. In Section 2.3.1 the estimation of velocity is described and discussed, followed by the amplitude properties of snow and ice in Section 2.3.2. In Section 2.3.3 an overview is given of the SAR acquisition geometry and concluded by the terminus position estimates in Section 2.3.4.

2.3.1. OVERVIEW OF DISPLACEMENT ESTIMATION TECHNIQUES

To observe velocity in a SAR-image there are several methods available, all with their own capabilities and limits. Offset tracking, as described in Section 2.3.1, relies on tracking patches of pixels using their specific properties. Interferometry and spectral diversity uses phase difference information to estimate displacements.

OFFSET TRACKING

With offset tracking, one tries to estimate displacements in the image. This can be done by tracking features, such as crevasses, speckle patterns etc, using either coherent or incoherent cross-correlations.

Estimating cross-correlations, in radar processing also known as 'speckle tracking', uses amplitude information in a radar image to estimate a cross-correlation function between two images to estimate displacements. The accuracy is about 0.1 pixel for radar images (using oversampling) and the technique still works over featureless areas (Joughin et al., 2010b), such as ice sheets. The technique has proven to work for fast-flowing glaciers with a quick decorrelation (Gray et al., 2001).

The cross-correlation can be estimated both coherent (CCC, using phase and magnitude information) or incoherent (ICC, solely magnitude information). When the coherence γ is maximum, $\gamma = 1$, the variance of CCC is theoretically regarded better with a factor 1.8 compared to ICC (De Zan, 2014), and for lower values of γ the variance of CCC with respect to ICC is even better. Although it is theoretically more accurate than ICC, CCC requires the phase signal to be stable and both the reference phase as well as the topographic phase has to be removed. As most available data consists of old images (ERS-1/2, EnviSAT), with large temporal and perpendicular baselines and gyroscope malfunctioning, applied on a remote and dynamic region, ICC is the regarded most reliable and feasible method. For this project this technique is therefore the most suitable technique. Although a matter of definition, ICC can be described as 'amplitude tracking' and CCC can be described as 'coherent tacking'.

Normally amplitude tracking is used for the coregistration of an image pair, as orbit information alone is generally not accurate enough. To obtain glacier velocities, one is interested in the residual displacements that remain after a proper coregistration of two images. It should be noted though, that the non-stationary (i.e. water, glaciers) areas should not influence this coregistration to avoid a misregistration.

Although very similar, texture tracking is based on a statistical description of the amplitude signal and not on (complex) cross-correlations. Using a Fisher distribution the pdf of the amplitude signal of a SAR image is calculated, and using a maximum likelihood method the offset between two images can be calculated. The accuracy is similar or better to ICC, but the method has not been used on broad scale. The main advantage of this method is that it has the potential to combine information from different polarizations. As there is no multi-polarized SAR data available in this project, this method is discarded. For future mission with multi-polarized capabilities (Sentinel-1) this might be an interesting method (Harant et al., 2011, Erten et al., 2009).

INTERFEROMETRY

Interferometry uses the phase-difference between two radar images to estimate displacement. This difference is only known modulo 2π, which is represented in the form of fringes throughout the image. One observes the topography as well as deformation. As one merely wants to observe deformation, the topography should be removed properly. In order to obtain usable information about the phase, the image pair should be sufficiently coherent. As glaciers are moving objects, decorrelation is inevitable. Temporal decorrelation happens once the relative position of individual scatterers within a pixel change on the scale of half of the wavelength, in the timeframe between two acquired images. If applied properly, this method can be very accurate (millimeter precision). In figure 2.18 an example is shown of the Rutford Ice Stream(Joughin et al., 2010b).

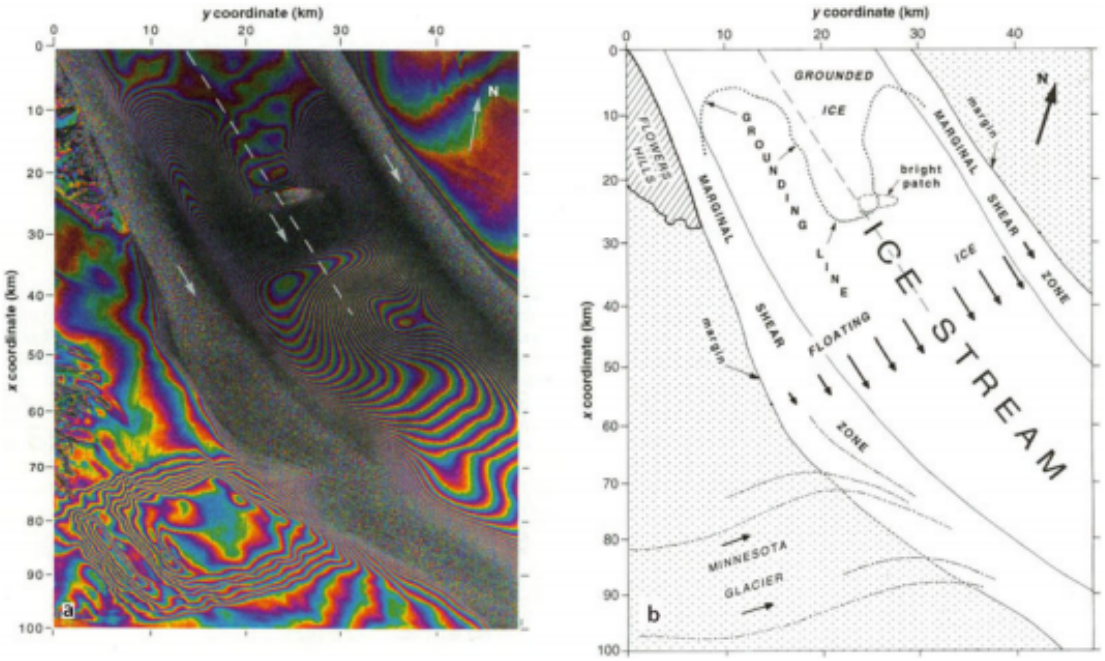

Figure 2.18: An ERS-1 SAR interferogram (a) and the corresponding ice stream zones for Rutford Ice Stream (b) as created by Goldstein and others (Joughin et al., 2010b).

Depending on the outflow speed of a glacier, decorrelation happens within days to months. Although the surface of a glacier moves with the glacier, its appearance does not necessarily have to change. As long as the scatterers undergo small changes relative to the wavelength, coherence can be maintained. In practice this is a complex process, as the glacier experiences friction on its base (basal drag) and on the sides (side drag). The side drag induces shear forces, causing quicker changes leading to tight fringes, aliasing or decorrelation. Another dominant source of decorrelation is accumulation. These effects can be seen in figure 2.18b. Using interferometry to estimate glacier displacement is, with a 35 day baseline, limited to glacier speeds up to 125 m/yr (Gray et al., 2001), which is exceeded by all the glaciers in the Uummannaq region.

Observations are done in the line-of-sight (LOS) direction of the satellite, so a phase-difference contains both horizontal and vertical deformation. For glacial studies, an assumption can be made that the deformations perpendicular to the slope are zero. This holds that the measured displacement in LOS is actually surface-parallel. With this assumption it is possible to obtain a solution in two orientation dependent directions, stated that there is enough knowledge about the slope. If this assumption does not hold, i.e. submergence/subsidence, then this method can lead to errors. Another solution would be to obtain 3D velocity vectors by having multiple observations from different look angles (Joughin et al., 2010b).

SPECTRAL DIVERSITY

Originally developed as coregistration method, spectral diversity observes motion by estimating the misregistration (similar to cross-correlations) (Van Oostveen, 2014). Two inferograms can be generated from two SAR-images by using a band pass filter. Summarized, the differential phases can be converted into a timing error that, in turn, can be converted into an offset. This process has to be performed in both azimuth and range direction in order to obtain a 2D velocity estimate and implies that the topography and orbit are known (Van Oostveen, 2014).

The main advantage of this method is that it can be more accurate than cross-correlations and requires no phase unwrapping (in contrast to interferometry), so it can also be applied on high ice speeds. However, it less accurate than interferometry and requires a stable phase. As a stable phase signal might not be present in a big part of the ERS-1/2 data, see Section 2.2.2, this method is discarded for this project.

COMPARISON OF METHODS

The methods discussed in the previous sections have different characteristics and properties. In order to make a proper assessment on which set to use, a trade off is performed by comparing the different properties in Table 2.3. For this project four aspects are important considerations: implementation, accuracy, maximum traceable velocity, sensitivity to decorrelation and dependency on a stable phase. The latter three aspects are specifically important for this project, as high velocity marine terminating glaciers are considered, with a quick decorrelation and with old ERS data as described in Section 2.2.2. Implementation refers to the availability in DORIS and the feasibility to implement it in DORIS.

Table 2.3: Trade-off of the discussed Velocity Estimation methods. *The accuracy of texture tracking increases when multiple polarizations are available (Harant et al., 2011, Erten et al., 2009).

Method	Accuracy	Implementation	Maximum Traceable Velocity	Decorrelation Sensitivity	Stable Phase Dependency
Amplitude Tracking (ICC)	-	++	++	+	++
Coherent Tracking (CCC)	o	o	++	++	–
Texture Tracking	-	–	++	++*	++
Interferometry	++	++	–	–	–
Spectral Diversity	o	+	++	++	–

Based on the dependency of calibrated phase, three methods are discarded: 1) coherent tracking, interferometry and spectral diversity. They are discarded because the best timeseries are ERS images, which (partially) consists of an unstable phase (see Section 2.2.2). ICC is therefore regarded to be the best method for this project. Texture tracking is theoretically a better method, but it is not implemented in DORIS and will require a lot of resources to do so. Next to this, it is a new method that is only applied once in Erten et al. (2009), and its main extra benefit is in multi-polarized data (which is not available in this project). The added value of texture tracking with respect to ICC is not big enough to use resources on implementing it, although it is recommended to explore this method for future research with Sentinel-1.

2.3.2. AMPLITUDE PROPERTIES OF SNOW AND ICE

The amplitude is a representation of the amount of signal that is reflected, as discussed in Section 2.2.1. As the amplitude is used for estimating offsets with ICC offset tracking, the terrain properties of the reflected amplitude from ice and snow are important considerations. Although the reflection is also dependent on the incidence angle, a dominant factor is the state at which the ice or snow is in (Fahnestock et al., 1993, König et al., 2000). As one can see in Figure 2.19 the SAR amplitude reflections are varying with the seasons.

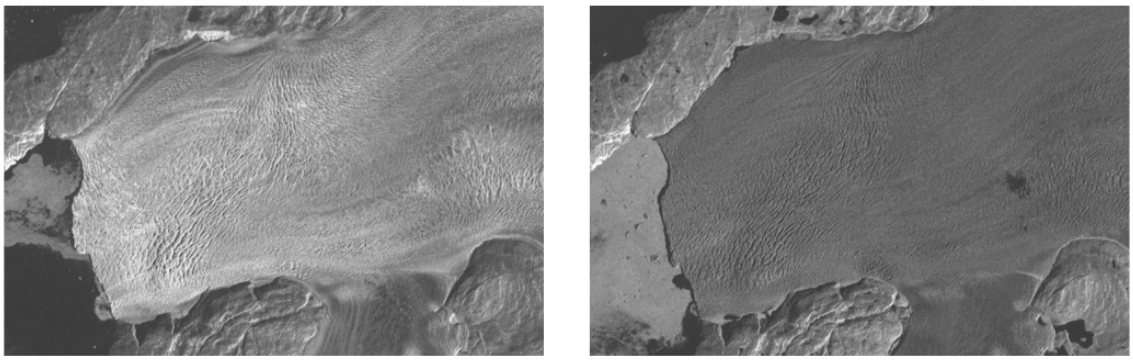

Figure 2.19: Two TerraSAR-X acquisitions of Støre Gletscher acquired with the same incidence angle. Left one can see an image from 10-11-2011 and right one can see an image from 29-06-2011. Apart from the changes in amplitude, also small lakes are visible.

Fahnestock et al. (1993) defined four different facies in ice sheets based amplitude differences found in ERS-1 data, that appear from high to low altitude:

- **Dry-snow** can be found in the high interior of the ice sheet and is unaffected by meltwater. The uniform fine grain structure and low density produce little backscatter, and therefore it appears dark in SAR image.

- **Percolation** facies are found a bit lower than dry snow, and occurs in zones where the meltwater percolates down. Freezing of this meltwater in the cold snow firn leads to 'ice lenses' that produces a bright reflection in radar images.
- **Wet-snow** facies are found on places where the snow has reached the melting point due to latent heat released by refreezing of meltwater. Compaction is enhanced, resulting in a denser firn, resulting in a reduced penetration of radar signals. This zone is observed a bright during the winter, but becomes dark when the firn is water-soaked in summer.
- **Bare-ice** is a combination of glacier ice formed by compacted snow of higher elevations and refrozen ice from meltwater. The main difference with the wet-snow facies is that its surface is smoother and thus produces less backscatter than wet-snow facies in winter, but is brighter during summer due to melt in the wet-snow zone.

These different facies will vary throughout the season and will influence the amplitude, hence it can be expected that decorrelation occurs quicker during spring and summer when the snow melts and bare-ice becomes visible. In addition, Konig et al. (2001) also stated that SAR images (made by C-band) are not observing the equilibrium line (line between ablation and accumulation) but a firn line, an area where old snow is compacted for many years. Meaning that C-band is not sensitive to new snow, but to older, more compacted layers.

2.3.3. ACQUISITION GEOMETRY

The Uummannaq region consists of many narrow and deep fjords with a height difference ranging up to 2 km from valley to top. This topographic situation has important consequences for the SAR geometry in the fjords, leading to geometric effects as layover, shadowing and foreshortening.

As a SAR is sending and receiving pulses, it can only observe the time (and thus range) in a slant-range geometry. As depicted in Figure 2.20, an upward (as seen by the platform) mountain slope will be compressed in the image as its length in slant-range is smaller compared to a flat surface, and the reverse effect happens on the downward slope. This effect is called foreshortening, and it also means that the reflections from the upward slope are compressed in a limited number of pixels resulting in very bright features, whereas the reflections from the downward slope are stretched in many pixels resulting in a darker downward slope. When there is a shadow, so no reflection from the downward slope at all, they appear completely dark.

For steep slopes the top of the mountain might be closer to the platform than its foot, leading to 'layover' for upward slopes (see Figure 2.20). In the image the reflection from the valley and from the mountain itself cannot be distinguished as the signal is received at the same moment. This effect leads to noise parts in the image where the mountain is projected on top of its foot.

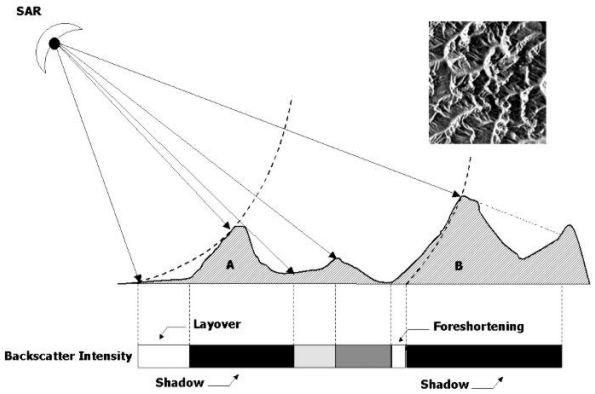

Figure 2.20: An overview of layover, foreshortening and shadow in a mountainous terrain. These effects are also observed in the Uummannaq region.

For some glaciers in the Uummannaq region, especially in the Northern part, this effect is big enough to distort half of the Fjord. The fjords in the North are relatively narrow and high, and their orientation is unfavourable for acquisitions made from a descending orbit, leading to layover and foreshortening effects.

This effect is observed in all the descending images of the Inngia Isbræ, as depicted in Figure 2.21, resulting in a part of the image that cannot be used.

Figure 2.21: Layover effects, marked by red circles, on Inngia Isbræ and Umiammakku Isbræ.

2.3.4. GEOLOCALIZATION OF TERMINUS POSITION

As discussed in Section 2.1, the terminus position, or in other words the front of the glacier, is an important characteristic for the glacier. Melt, either at the surface or at the base, causes ice at the terminus to weaken, crack and eventually to calve (break) from the glacier. Its position varies in time and it's retreat or advance tells something about the climatic stability of the glacier.

The implementation of the digitization is discussed in Section 3.3.2, but the mechanism and influence of the SAR-viewing geometry and geocoding on the position of the terminus is elaborated in this section.

As highlighted before in Section 2.2 the complex SLC image data has to be projected on the Earth using a DEM. This holds that the relation of range and height leads to a representative point on the Earth and that an error in the DEM-height leads to an incorrect geolocalization. As the DEM has its own fixed terminus line, an inconsistent geocoding is applied around this terminus position. This is also dependant on the viewing geometry, i.e., orbital mode and incidence angle, of the satellite. See Figure 2.22 for an illustration of this problem.

Suppose a glacier running from east to west, as depicted in Figure 2.22, and imaged from both a descending as well as a ascending orbit. Three situations are possible, the terminus as defined in the DEM is underestimated or overestimated or exactly the same as the real terminus line. Given the variation along the terminus line the latter is very unlikely.

For the glaciers in the Uummannaq regions, descending images will observe the glacier from the landside, and therefore look over the terminus and generate a shadow behind the terminus. Ascending images will look onto the terminus and also view the front side of the terminus, meaning that a strong reflection from the terminus base might be expected. In this case, the descending image will lead to a false geocoding on locations where the DEM underestimated the terminus line, as these points are projected on sea level.

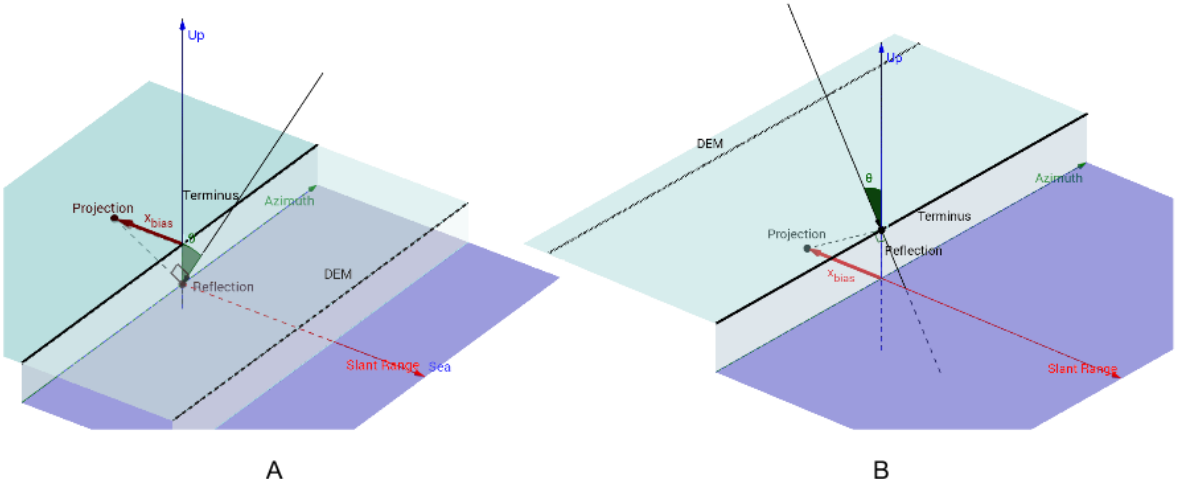

Figure 2.22: The SAR geometry around a terminus for two situations. A) An ascending orbit is considered. The main reflectivity comes from the base of the terminus and a geocoding error can occur if the DEM overestimates the actual terminus position. B) A descending orbit is considered. The main reflectivity comes from the terminus top and also a geocoding error can occur if the DEM underestimates the actual terminus position.

For an ascending image the opposite is the case, where overestimation leads to a false projection. The main reflection comes from the terminus base, but will be projected on the glacier.

The maximum bias x_{bias} in terminus position that is caused by this geometric effect can be estimated using the incidence angle and the height of the terminus:

$$x_{\text{bias}} = \frac{z_{\text{term}}}{\tan(\theta_{\text{inc}})}. \tag{2.20}$$

With z_{term} as the terminus height and θ_{inc} as the incidence angle. A graphical display of the relation is given in Figure 2.23, where it can be seen that a high incidence angle is preferable to reduce a terminus bias. The terminus position in the DEM will influence the geolocalization of the glacier terminus by projecting it either at sea or glacier level. This will lead to a bias when digitizing this position, which is dependant on the orbital mode and incidence angle of the satellite.Therefore it is decided to fill the fjord at glacier level, in order to consequently overestimate the real terminus position, resulting in an expected bias in ascending frames. Equation 2.20 gives however a theoretical maximum and will, depending on the local terminus geometry and water reflection, not be the same in each frame.

2.4. EXTERNAL DATASETS

In this section the external datasets are elaborated and discussed. These external data is required for two purposes: 1) assisting the SAR-data processing and 2) to allow a synthesis of the results. Both climate data (Air Temperature, Sea Surface Temperature, Sea Ice Fraction) as discussed in Section 2.1 and glacier specific data (DEM, bedrock, bathymetry) is used.

2.4.1. DIGITAL ELEVATION MODEL

A Digital Elevation Model (DEM) is crucial for SAR processing, as it is an important input for coregistration and geocoding. For this project there were three DEM's available

- Viewfinder Panoramas DEM (de Ferranti)
- Intermediate TanDEM-X DEM
- Greenland Ice Mapping Project (GIMP) DEM (Howat et al., 2014)

The three DEMs are visualized in Figure 2.24. An important absent in this overview is the SRTM DEM, which is only acquired below 60° N. The Viewfinder Panoramas DEM features a SRTM alternative, but is compiled from different sources, such as topographic maps, Landsat imagery and reprojected ICESat data,

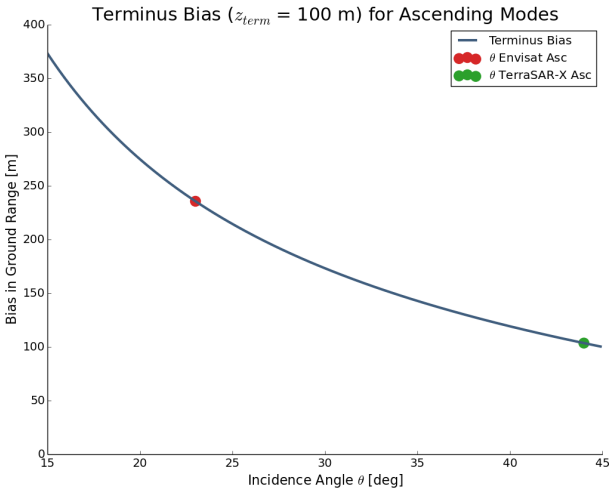

Figure 2.23: The relation between the incidence angle θ and the terminus geolocalization bias x_{bias}, based on a terminus height z_{term} of 100 meter. The bias scales linearly with the terminus bias. The red and green dot indicate the incidence angles of ascending Envisat and TerraSAR-X acquisitions, respectively.

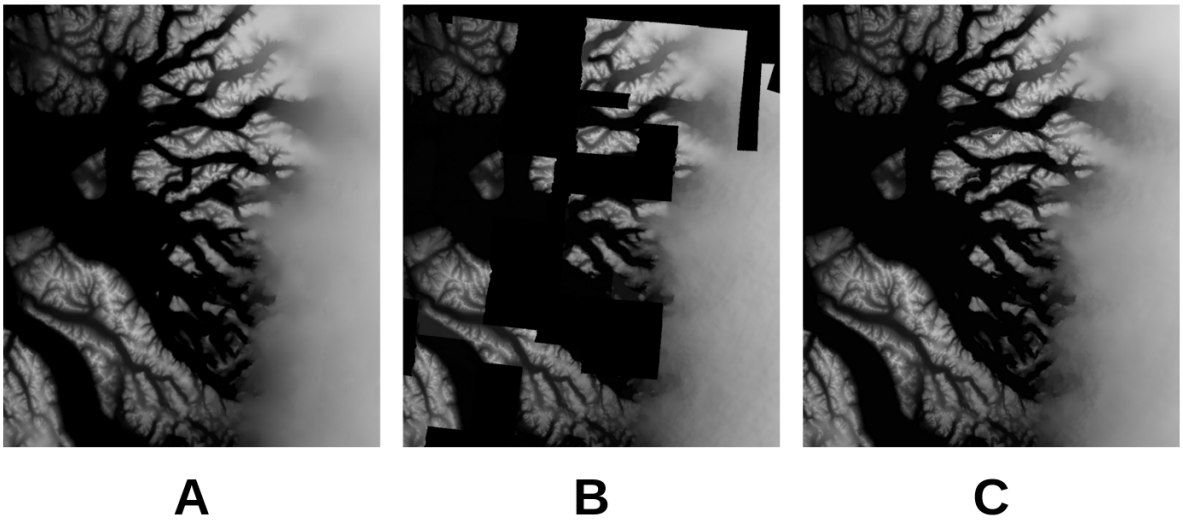

Figure 2.24: Comparison of the three available DEM's. A) Viewfinder Panoramas, B) TamDEM-X IDEM, C) GIMP DEM.

and resampled at 3" SRTM-resolution (90 x 30 m), although the real solution is mostly lower. The Intermediate TanDEM-X DEM features a high resolution (15x15 to 30x30 meter) and is made by Airbus, but it contains big gaps (see Figure 2.24) that are also located above glaciers. As this is only an intermediate product, a final version of the DEM might be interesting for future research. The GIMP DEM also consists of multiple datasources, which includes PEB (Photo Enhanced Bamler), GDEM2 and SPIRIT, that are merged and resampled to a grid of 30 x 30 m. The resolution of this DEM is higher than Viewfinder Panoramas, which becomes clear in the simulated amplitudes (Figure 2.25). The processing in this project is done using this GIMP DEM, because of its higher resolution.

As described in Section 2.3.4, the DEM has an influence on the terminus projection. Therefore it is chosen to manually fill the fjord, as if there was a glacier, using a simple IDW technique followed by smoothing to avoid large height jumps. This 'fjord filled'-DEM is used for geocoding, while the coregistration uses the original DEM. The 'fjord filled'-DEM is referred to as DEM+.

In addition to a DEM, the GIMP project also used LandSAT-7 ETM+ images for a land-classification, leading to ice and sea masks resampled to a 15 x 15 m grid. These masks are useful as auxiliary input during the coregistration of the SAR images, as described in Section 3.2.1.

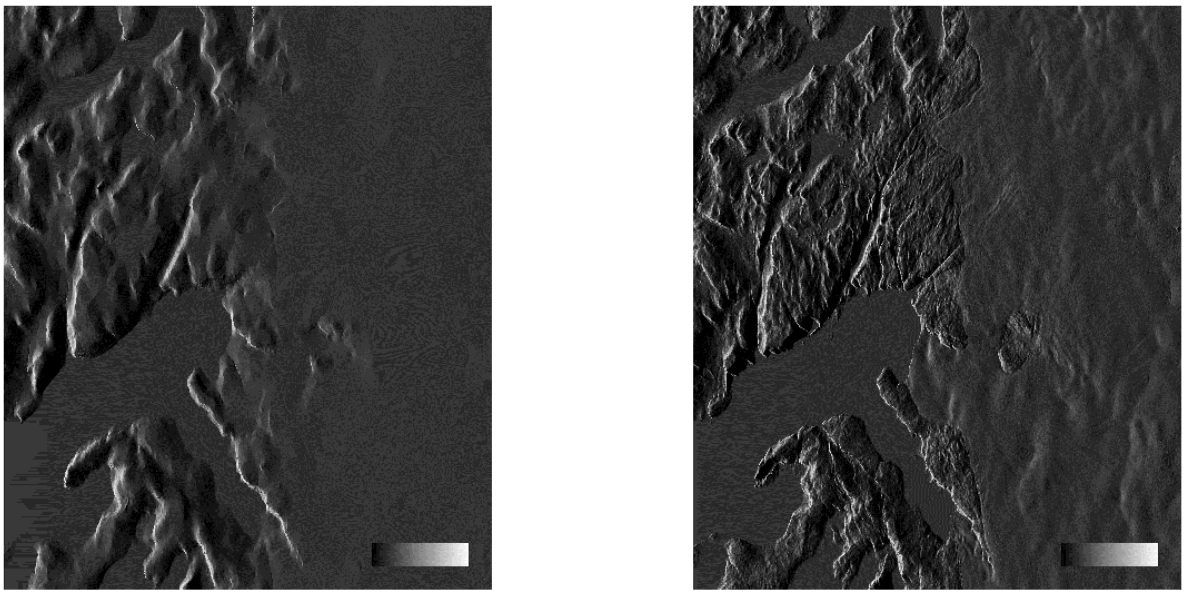

Figure 2.25: Comparison of the simulated amplitude between A) Viewfinder Panoramas and B) GIMP DEM.

2.4.2. WEATHER OBSERVATIONS

In order to link the glacier evolution in the AOI to climate forcing, Surface Air Temperature is used as paramater to describe the atmospheric contribution. Data is used from the Danish Meteorological Institute (DMI) that gathers multi-diurnal weather observations in Greenland from 1958 using synoptic stations (Cappelen, 2014). In the AOI there are three stations, see Table 2.4, but they have been operating in different places and different timespans. The similarity between the sets is high (correlation 0.96, median difference: 0.0°C) and they also show similar trends. Especially the observations from station 04213 and 04214 are relevant to compare with the SAR datasets, as station 04212 has only two years of observations within the timespan of SAR images. Data taken from station 04214 are located on the outer west of the Uummannaq Bay, 500 km away from the glaciers. Therefore data from 4213 is considered more representative for the atmospheric conditions on the glaciers.

Table 2.4: An overview of the weather stations in the Uummannaq-region. DMI is the Danish Meteorological Institute and MIT is the Greenlandic Airports (Mittarfeqarfiit).

Station ID	Station Name	Owner	Timespan	Location	Elevation
04212	Uummannaq	DMI	01-01-1961 to 21-08-1989	70.40, 52.07	39
04212	Uummannaq Heli.	MIT	23-01-2004 to 30-06-2006	70.41, 52.07	2
04213	Mitt. Qaarsut	DMI	23-11-2000 to 23-10-2005	70.44, 52.42	88
04213	Mitt. Qaarsut	MIT	01-02-2006 to present	70.44, 52.42	88
04214	Qullitsat	DMI	01-01-1961 to 31-08-1972	70.05, 52.07	2
04214	Qullitsat	DMI	18-09-1982 to present	70.41, 54.37	27

Using a least-square estimation a multi-annual trend can be estimated for the datasets. It is shown that station 04214 observed a trend of approximately 0.27°C between 1990 and 2010, in line with estimations from Carr et al. (2013a). The trend which has been observed between 2000 and 2013 in station 04213 and 04214 is quite similar: 0.08°C and 0.10°C respectively.

2.4.3. SEA SURFACE TEMPERATURE AND SEA ICE FRACTION

As discussed in Section 2.1.2, Sea Surface Temperature (SST) and Sea Ice Fraction (SIF) are important climatic parameters that have a potential influence on the seasonal behaviour of glaciers. One would actually like to know the temperature of the subsurface layers, i.e. Atlantic Water (AW). However, it is not possible

with modern techniques to measure these temperatures on a spatial scale and temporal interval that would be required to use these parameters in an analysis. As an alternative, SST is used to represent the oceanic forcing on a glacier.

SST is obtained from the AVHRR Pathfinder Version 5.2 Level 3 data from the NOAA (Kenneth et al., 2011), a 4 km grid with SST and SIF obtained twice per day by Polar Operational Environmental Satellites (POES) from the NOAA. Data are available from 1982 to 2012. It can be easily accessed using Google Earth Engine and an average value of the Uummannaq fjord-system is used as representative value for the entire region.

2.4.4. BEDROCK AND BATHYMETRY

One of the glacier-specific factors discussed in Section 2.1.2, is the fjord topography. In order to describe the topography, bedrock and bathymetry data was obtained from operation IceBridge by the NASA. The goal of operation IceBridge is to "better understand processes that connect the polar regions with global climate change". For this operation all observations are made airborne, thereby bridging the gap between different satellite missions. Several observations are acquired, ranging from laser altimetry to gravimetry, and several L3 and L4 products are made available to the scientific community. For this thesis, the bedrock and bathymetry data was used to compare the different fjord-geometries.

The bedrock data was obtained using radar-derived thickness data and satellite radar data (Morlighem et al., 2015). Based on the thickness and motion of the ice, the bedrock topography can be modelled. The data has been reviewed by Morlighem et al. (2014) and it was discovered that there are deep subglacial channels under the GrIS. As a reference the GIMP DEM, as described in Section 2.4.1, is used. The bathymetry data was acquired using gravimetry and has an accuracy of about 50 to 200 meters (Cochran et al., 2015). Although not very accurate, no other data sources exists that have mapped fjords in the Uummannaq region. The estimated bathymetry will give an idea about what types of water are able to interact with the glacier front.

3

METHODOLOGY

In this chapter the implementation of the theoretical concepts, as described in Chapter 2, are elaborated in detail. At first, an overview is given on the workflow applied in Section 3.1. In the sections thereafter the processing phases are described, starting with the SAR processing by DORIS in Section 3.2, followed by the post-processing of these data, in Section 3.3.

3.1. OVERVIEW

The workflow applied in this study consists of three distinctive phases as depicted in Figure 3.1: SAR processing, Post-Processing and Analysis. The phases are distinctive in their implementation, meaning that they are connected via data-products.

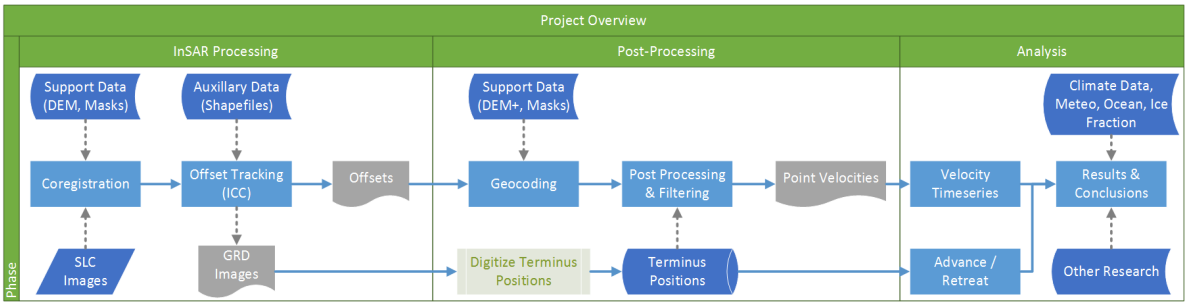

Figure 3.1: Overview of the project consisting of three phases.

The design of the implementation, mainly in terms of coding, has been made by both a product approach (top-down) as well as a processing approach (bottom-up), as depicted in Figure 3.2. From a product point of view the implementation is approached from top-down, where the final product is leading in the design, and products lower in the chain are considered intermediate products between the final product and the raw data. In this approach the focus lies on a 'product to product' chain rather than the processing steps.

From a data point of view the processing chain is considered bottom-up, thereby following the data. During this approach the focus lies on the processing steps needed to get to derived data products.

The three phases are implemented such that only data products are transferred between the different phases. The software is object-oriented to allow different parts to be designed separately, both the I/O interface as internal subdivisions. To efficiently use auxiliary tools, such as reading slc-images, output files, etc, a toolbox is created to exchange data between DORIS and other packages.

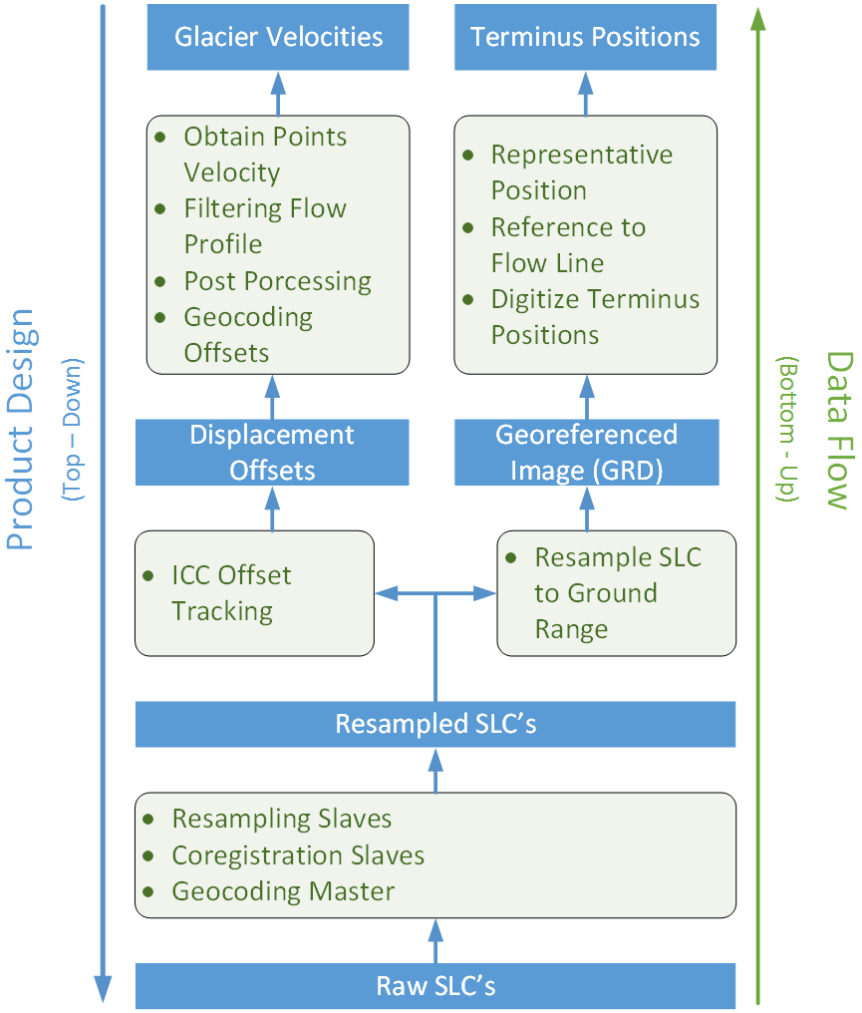

Figure 3.2: An overview of the Top-Down, product to product, approach and the Bottom-Up, data-flow, approach. The processes in the data-flow approach are always between two products.

3.2. SAR PROCESSING BY DORIS

The first processing stage of this project is the SAR processing performed by Delft Object-oriented Radar Interferometric Software (DORIS) and consists of four processes (see Figure 3.3): 1) initial processing of the master image, 2) coregistration of the original Single Look Complex images (SLC) to resampled SLC images, 3) Incoherent Cross-Correlation (ICC) offset tracking and 4) resampling into a Ground-Range Detection (GRD).

A wrapper called DorisStack is designed (as a python package) to pilot DORIS for organising, executing and logging of DORIS processes, but also to perform additional processing, such as contextual input, preparation of input files. For the initial processing and coregistration steps the InSAR-processor module of DorisStack is used, that prepares the master and starts a centralized coregistration. The other steps are specific for this thesis and therefore performed in the newly developed SIMONE-processor module (see Figure 3.3), that manages ICC offset tracking in a consecutive sequence and generates GRD's based on the stack geocoding.

The four processing steps are elaborated separately; the initial processing is discussed in Section 3.2.1 followed by the coregistration, in Section 3.2.2. ICC Offset Tracking and GRD resampling are addressed in Sections 3.2.3 and 3.2.4, respectively.

3.2.1. INITIAL PROCESSING

The initial processing is needed to prepare the coregistration of the entire SLC-stack, by geocoding the master and thereby allowing contextual input at this stage. As all the images are resampled onto the same reference-image geometry, by a centralized coregistration of all slaves with respect to one master, the most suitable

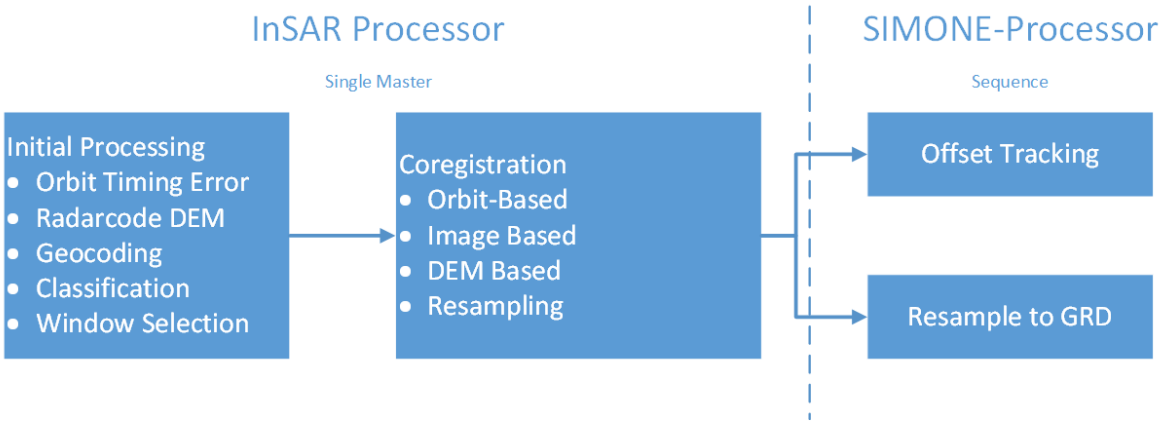

Figure 3.3: Flowchart of the SAR processing. In the first phase, operated by the InSAR Processor, the images are coregistration to a single master. In the second phase, operated by SIMONE-Processor, the images are considered in a sequence to find offsets and to resample a GRD.

image in terms of the perpendicular and temporal baseline is chosen as master to minimize temporal decorrelation.

An exception is made for ERS-2 YCM images, as discussed in Section 2.2.2, their geocoding is unreliable as result of the gyroscope failure. Although not optimal, the master image has to be before Jan 2001 and cannot always be chosen such that its temporal distance to all the slaves is minimal.

During the initial processing all images are read, their precise orbits are retrieved, their baselines are calculated and the most suitable image is selected as master. Preparation is then performed on the master image before coregistering each slave, using the following sequence:

1. Simulation of an amplitude image using a Digital Elevation Model (DEM).
2. Calculation of the orbit timing error based on the simulated amplitude.
3. Creation of the radarcoded DEM (based on the DEM+, see Section 2.4.1).
4. Geocoding based on the radarcoded DEM.

First, the master (orbital) timing error is computed using a coarse coregistration to a simulated amplitude of the DEM using DORIS. This step is important for ERS-1/2 and EnviSAT, as their orbit timing is not known with sufficient precision to directly start geocoding them. This step is not applied on TerraSAR-X frames, as the timing in their delivered science orbits are sufficiently accurate enough (Yoon et al., 2009). The precision of the orbits, both for TerraSAR-X as well as for ERS/Envisat is known within 0.2 m (Yoon et al., 2009, Scharroo and Visser, 1998). When the orbit timing is corrected, a radarcoded DEM is produced to obtain a height for each pixel in the master image. As discussed before in Sections 2.3.4 and 2.4.1, a modified DEM is used (DEM+) to overcome issues around the terminus line.

Using the radarcoded heights the image pixels are geocoded to obtain a latitude and longitude for each pixel. As discussed in Section 2.2.3, SLC images are sampled in slant range, meaning that there is no constant ground spacing between pixels. Elevated features in the terrain such as mountains will, depending on their geometry with respect to the satellite, influence their position in the image. This can be seen in Figure 3.4, where the spacing between pixels (in degree) is varying along with the topography in the image.

Finally, after the initial processing, a master image is selected and geocoded. Using the master image and the geocoded information, all other slaves can now be coregistrated onto the same frame.

3.2.2. STACK COREGISTRATION

Once the master image is geocoded, external information can be inserted to improve the processing. This contextual processing with external data sources is performed to improve the accuracy, reliability and speed of the coregistration of each slave. The coregistration in DORIS consists of five different steps:

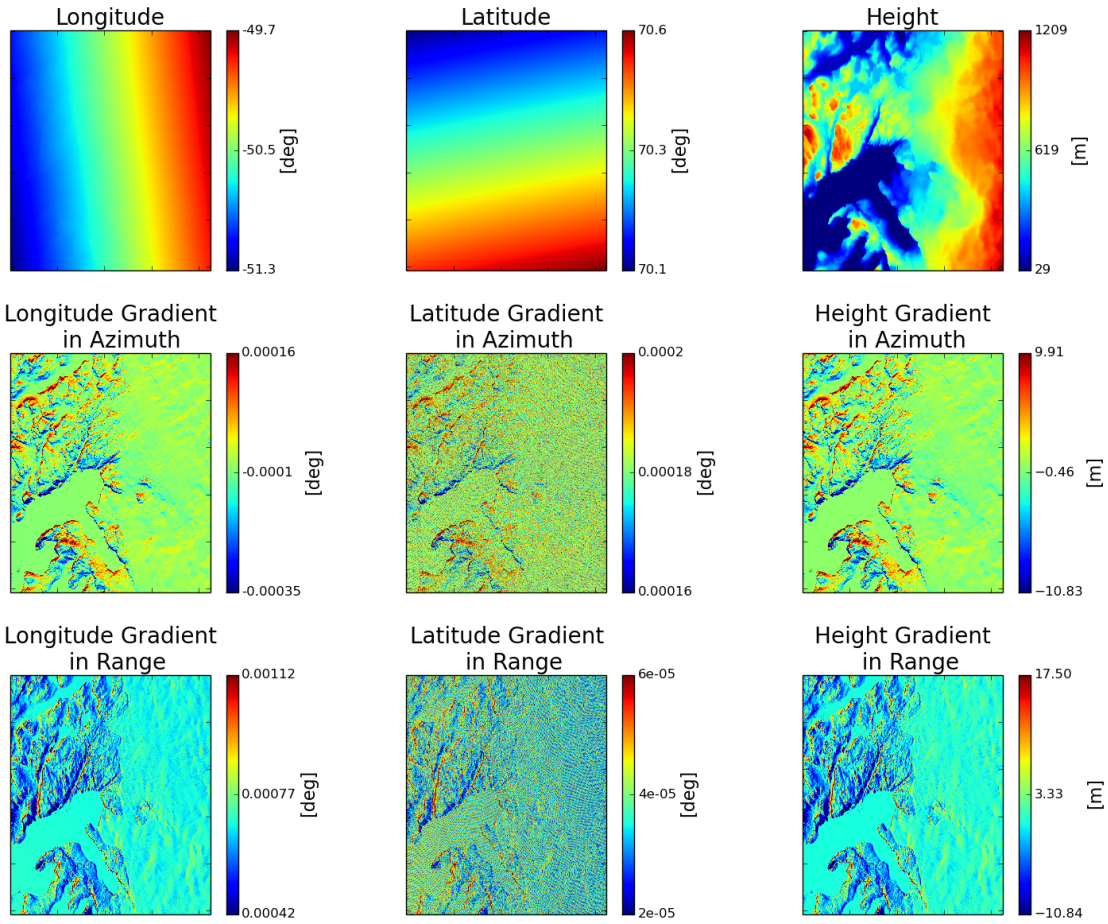

Figure 3.4: A visualization of the latitude and longitude steps between the pixels in a SAR-image. The top 3 images are the longitude, latitude and radarcoded height. The middle three images are the gradients in azimuth, the lower three images are gradients in range. It can be seen that there topography makes the image to be non-uniform in pixel-spacing.

1. **Orbit-based** coregistration (about 30 pixels accuracy (Kampes and Usai, 1999)).
2. **Course cross-correlation (ICC)** based coregistration (about 1 pixel accuracy).
3. **Fine cross-correlation (ICC)** based coregistration (about 0.1 pixel accuracy).
4. **Correction of the relative orbit timing w.r.t. master**.
5. **DEM-assisted** coregistration.

Important in this research is the two-step ICC-based coregistration as velocity estimations are made using the same method. In order to have proper, unbiased velocity estimates, the stationary areas are used for coregistration and the non-stationary areas are considered for velocity estimation. Water (including sea-ice) and glacial areas are not considered to be stationary and these areas are therefore discarded for coregistration. An ocean/ice mask, as provided by the GIMP project (described in Section 2.4.1), can be used to mask out these non-stationary areas and to create stationary coregistration windows. In this way computational power is focussed on the stationary areas, in order to find the patches of ground that potentially remain correlated in time. In order to ensure that sufficient windows are present and processing speed is maintained, an algorithm makes sure that between 6000 and 8000 windows are generated by widening or densifying a grid of generated windows.

Another issue of ICC-based coregistration in glacial areas is that there is a quick temporal decorrelation due to the ice and snow cover, hence the coregistration steps are challenging. Rocky areas are stationary, but might (partially) be covered by snow during parts of the year resulting in a varying correlation from image

to image. Even in this masked stationary region, a lot of decorrelated windows are found. Therefore, a new selection approach is developed, to improve the coregistration in these areas, thereby maintaining the same processing speed as much as possible. An empirical selection is made by the 'best slave' with respect to the master. The 'best slave' features a small temporal and perpendicular baseline, and can be used to filter out windows that are uncorrelated even in the most ideal situation. In this way, the number of coregistration windows is reduced and the processing speed is increased.

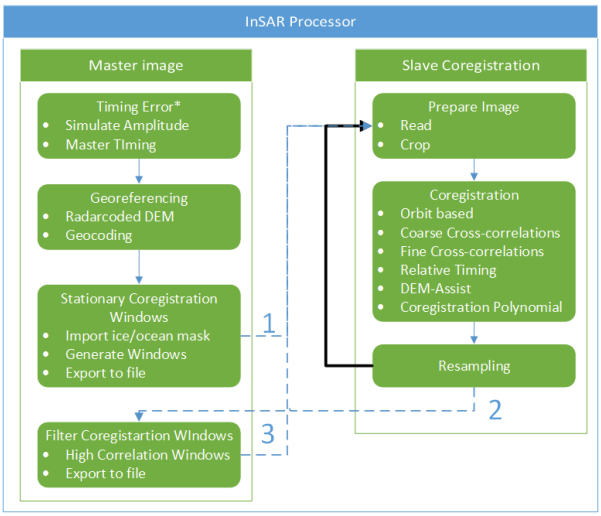

Figure 3.5: Overview of the coregistration processes. The numbers indicate the flow during the coregistration of the 'best slave': 1) coregistration of the best slave, 2) window selection based on high correlated windows and 3) start coregistration of all the other slaves.

When preparations are finalized, the slaves are coregistrated with the scheme in Figure 3.5 with respect to the master image. Evaluation showed that large temporal baselines can not be coregistrated without a geometrical coregistration (Relative Timing error and DEM-assist). The distinctive fjord-features in the images are key in coregistrating images with a large temporal baseline, where only a fine ICC-based coregistration might not be sufficient. An issue due to the window selection solely on 'stationary' areas is that only a certain part of the image is used for coregistration. By using a geometrical coregistration the high frequency elements of the coregistration warping function are estimated geometrically, while the image-based coregistration is only used to estimate a first order offset. After the coregistration the original slave images are resampled onto the grid of the master image.

After the coregistration the entire stack is resampled onto the same grid as the master image. This process is crucial in the project, as coregistration errors will lead to false results. As depicted in Figure 3.3, the processing flow now separates into two components: offset tracking (using to obtain flow velocities) and resampling to a GRD (used to digitize the terminus positions).

3.2.3. OFFSET ESTIMATION

When all the images are coregistrated onto the same frame, the residual motion in an image should be related to ground motion. Here we will elaborate how amplitude offset estimation is used to estimate displacement vectors on glaciers. This is performed using the SIMONE-processor module from DorisStack. As described in Section 2.3.1, various techniques are available for estimating displacements. It is chosen to work with ICC offset tracking that is normally used as fine coregistration step for DORIS. In contrast to the coregistration, images are now considered in a cascade order.

Similar to the coregistration first some preparations are required. As not the entire ice sheet is of interest, but only the glacier outlets, buffer zones are defined on the ends of the glacier. For each of the glaciers that appear in an image, these buffer zones are used to create gridded window locations (as line/pixel coordinates) as input for DORIS.

DORIS will then apply a fine coregistration to these windows and estimate offsets for each successive image (images with a failed coregistration are discarded here). Based on the temporal baseline between the consecutive images, DORIS refers to an input file with a window size, a search accuracy and an oversampling

factor. Larger temporal baselines means that the displacement of the glacier has been larger, resulting in larger estimated offsets. Therefore, the windows are chosen wider for longer temporal baselines. An overview of these settings is given in Table 3.1.

As stated in Section 3.1, only data products are transferred between the distinctive phases of the processing flow. Here, DORIS will export the estimated offsets to a file that is then the considered as final product of the SAR-processing stage. For glacier flow estimation, this is the point where the SAR-processing ends and where post-processing starts.

Table 3.1: Overview of the chosen ICC settings for amplitude offset tracking for different satellites and different temporal baselines.

Satellite	Temporal Baselines	Search Window [line/pixel]	Correlation Window [line/pixel]
ERS-1/2	1 to 3 days	64/16	16/8
ERS-1/2	34 days or more	256/128	16/8
Envisat	35 days or more	256/128	16/8
TerraSAR-X	11 days	256/256	16/16

3.2.4. GROUND RANGE DETECTION

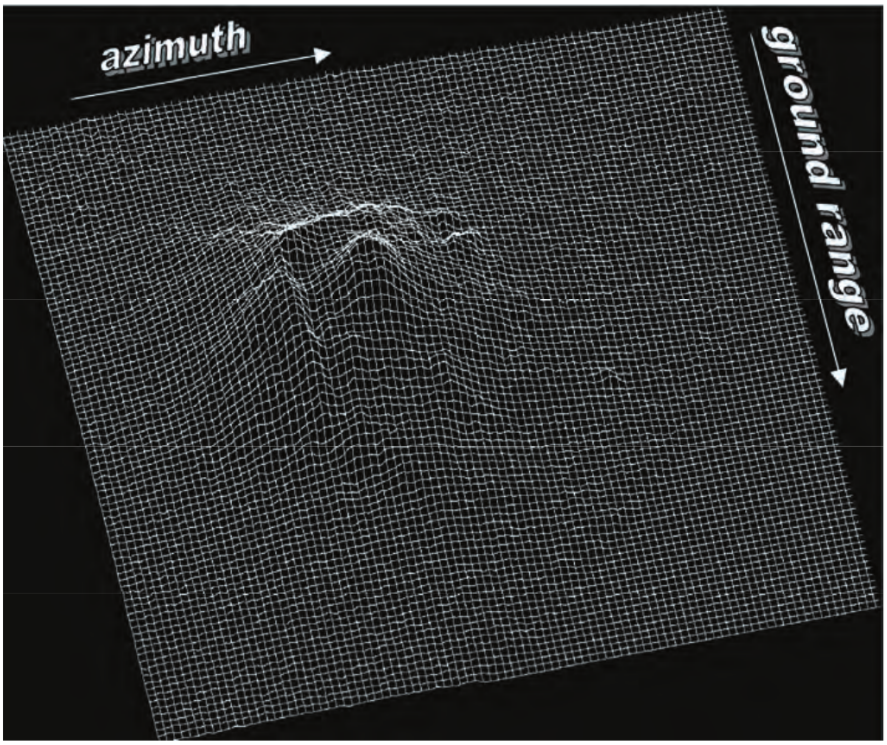

Figure 3.6: Slant range pixel spacing as projected on a ground range map. The spacing on the ground is not equal for each pixel and requires resampling into a Ground Range Detection product (GRD) (Ferretti et al., 2007)

In order to digitize the terminus position, the images have to be resampled into a geocoded grid. As described in Section 2.2.3, this is called Ground Range Detection. The goal of GRD images in this research is to digitize the terminus position of each glacier in each image, not to create a nice looking GRD created with sophisticated interpolation techniques and speckle filtering. Therefore a pragmatic approach is chosen by simply stacking SLC pixels, using their geolocation, in a predefined latitude-longitude grid, and then calculating the average amplitude value per gridcell. Small cells are chosen such that only a few pixels are stacked and resolution is maintained. Due to the small cells and the topographic effects, as depicted in Figure 3.6, it can happen that some gridcells are not filled by any pixel and are therefore empty. Normally one would like

to fill these pixels (for example by interpolation), but here there is no need for this.

It is favourable to have approximate square gridcells in terms of meters, but geocoding is done in latitude/longitude and spacing on latitude arcs is not constant to spacing in meters, but is dependent on the latitude of the arc. The central latitude of the image is used to calculate a square latitude/longitude spacing in terms of meters. Within one SAR image (acquired above the Uummannaq region, 70° N), there is a latitude different of 1 degree at most. This holds that the error made by taking the central latitude is around half a meter maximum.

Finally, the GRD is then saved as geotiff, that can be used for terminus digitization. This is where the SAR-processing ends. As terminus digitization is done manually, post-processing starts with the digitized positions. For terminus positions, the link between SAR-processing and post-processing is a manual one.

3.3. POST-PROCESSING

Post-processing is crucial in translating the data extracted from SAR-images to information that can be used for analysis. During the previous step, SAR-processing, offsets are estimated in the images and SAR-images are resampled on a geocoded grid. The latter is translated to terminus position by a manual digitization process. At this point, the post-processing comes in to convert the extracted data to useful information, that will be used for analysis. In order to process in an efficient way, a generic processing flow is introduced with an object-oriented structure, as depicted in Figure 3.7 and 3.8. The process is managed in a top-down approach, where the process is activated per glacier, that will activate processes regarding the stacks covering that glacier, that in turn will activate processes regarding the estimated offsets that are obtained in each stack. As an additional source of information the digitized terminus positions are loaded and processed per glacier.

In Section 3.3.1, a flowline reference system is introduced. This flowline reference system has been used throughout the post-processing. This flowline reference system is also used to find a representative point of the terminus position, which is elaborated in Section 3.3.2, and extended with an analysis on the error sources on the digitization process.

The processing of the estimated offsets, as visualized in Figure 3.7, is described in Sections 3.3.3 to 3.3.6. During the initialization the estimated offsets are read and imported. Then, processing can begin by geocoding the offsets under the assumption of a surface parallel flow, which is described in Section 3.3.3. Thirdly, the offsets are related to the glacier flowline, this is elaborated in Section 3.3.4. In Section 3.3.5, it is described how outliers are filtered out using a glacier along-track flow profile. Then finally, in Section 3.3.6, it is elaborated how the glacier flow is summarized as the equivalent glacier velocity.

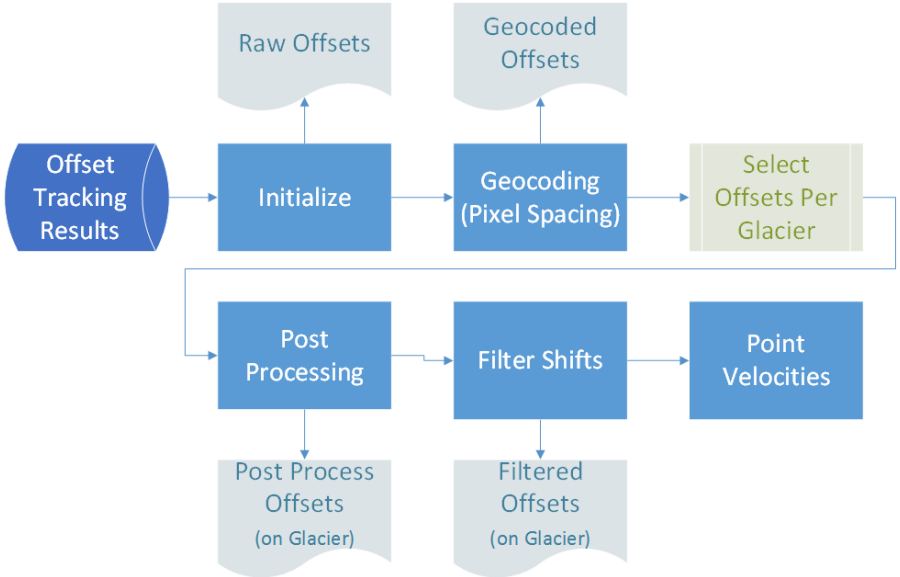

Figure 3.7: The five processing steps as performed during post-processing: initialize, geocoding, post-processing, filter shifts and point velocities. Initialize and geocoding are applied for all the offsets, after geocoding the offsets per glacier are selected and processing is continued glacier-specific.

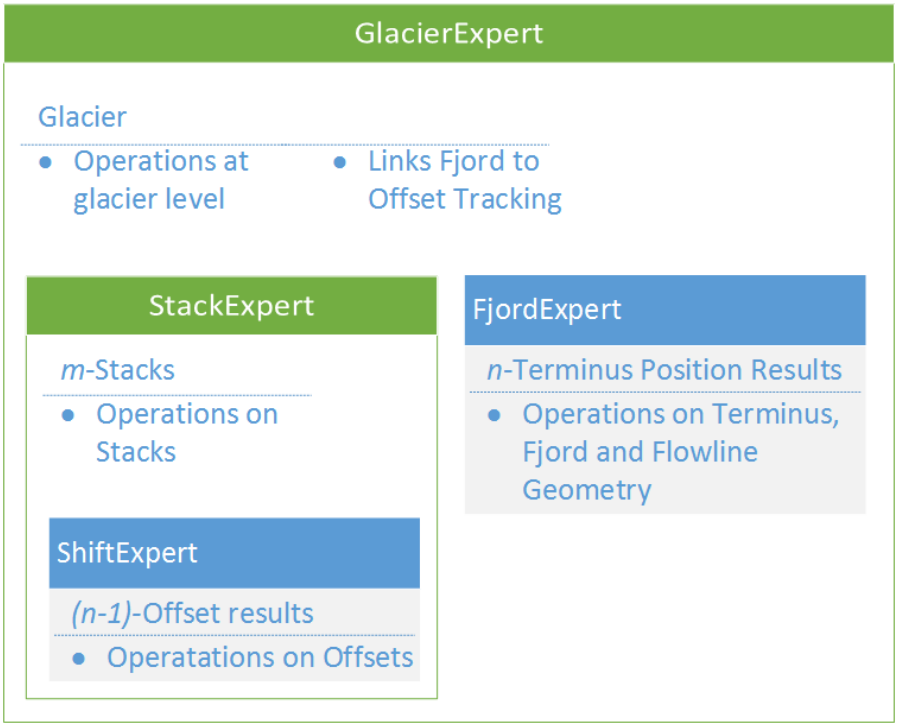

Figure 3.8: The post-processing structure. Each glacier is covered by m stacks, that in turn has n images (leading to $n-1$ shifts). As a side branch the information of the terminus-position is used to filter out shifts in the sea.

3.3.1. FLOWLINE REFERENCE SYSTEM

During the post-processing, the extracted data is converted to useful information. As outlet glaciers are observed, one would like to work in a reference system that is optimal when describing glaciers and their behaviour. As elaborated in Section 3.3.2, it is difficult to measure retreat when a glacier is situated in a curved fjord. For the post-processing of the velocity estimates, it is also convenient to refer to a along-track and across-track component and to filter out shifts that are not following the flow. It is therefore chosen to work with a FRS, that enables to refer to an along-track (parallel) and across-track (perpendicular) position relative to the flowline.

As most data is given in latitude and longitude, i.e., georeferencing of radar coordinates, terminus positions etc, the spacing is not spatially equal and distances first have to be converted to meters. It is chosen to work with three reference systems during the post-processing:

- **WGS84 (EPSG:4326)** in latitude and longitude. This is the system where DORIS provides geocoding, as the orbits are also given in WGS84.
- **Greenland Polar Stereographic (EPSG:5938)**. This system is defined in meters and can be considered as the local Greenlandic Coordinate Reference System (CRS).
- **Flowline Reference System (FRS)**, which is based on the flowline of the glacier. Coordinates are given in parallel and perpendicular position with respect to the flowline.

The ICC offset tracking results and terminus digitizations are delivered in latitude and longitude. They are then converted to meters by converting them to a polar stereographic system (EPSG:5938), that has a spacing in meters. Based on this CRS the distance can be measured with respect to a pre-defined flowline, with parallel and perpendicular distances as axes. In this way the glacier is projected straight, as depicted in Figure 3.9. Parallel distance can be determined by projecting each coordinate on the flowline, and in similar fashion the perpendicular position is the distance the point has relative to the line.

In order to determine the flowline of a glacier, 11-day TerraSAR-X data are used since they enable the estimation of a detailed velocity field (they have little to no outliers). Using IDW interpolation this velocity field is gridded to determine the streamlines. The maximum streamline is considered to be the flowline that

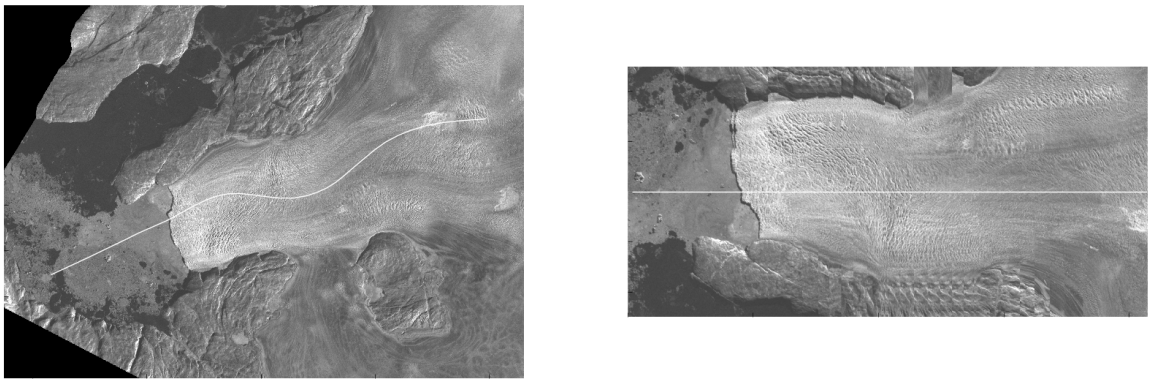

Figure 3.9: The flowline reference system. Left the Støre Gletscher is projected on a stereographic CRS and with the flowline visualized by the white line. The right image shows a flowline reference system, in which the white line is set to be the x-axis of the system. The glacier now appears to be straight.

represents the main ice flow along the glacier. In Figure 3.10 the process is visualized.

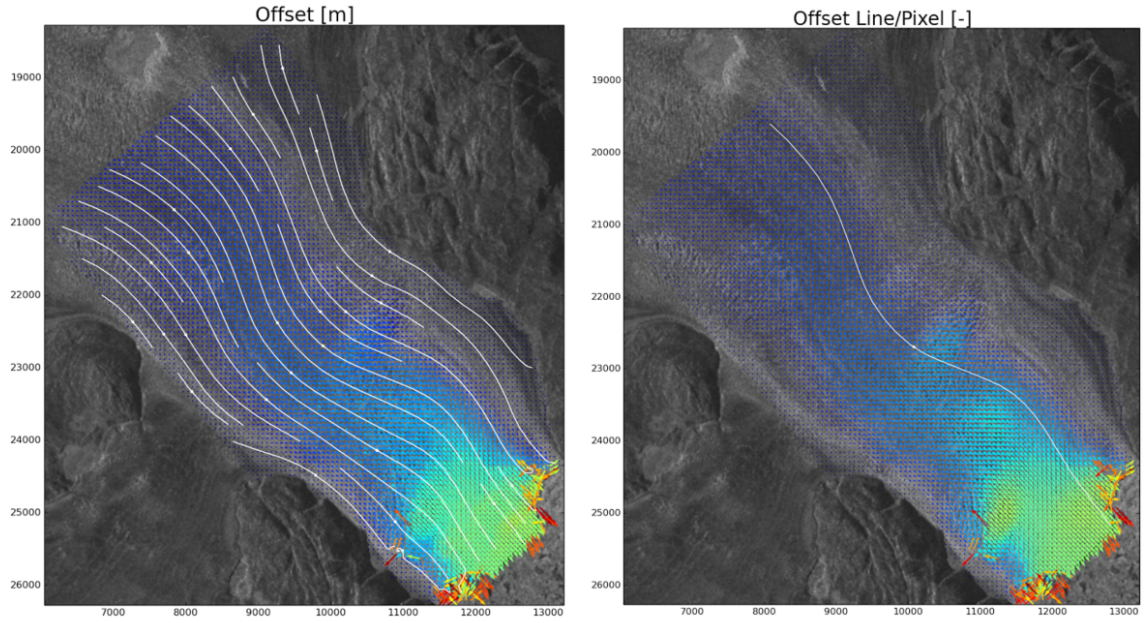

Figure 3.10: A streamline estimation of Støre Gletscher using a 11-day TerraSAR-X pair. Left one can see the streamlines that are found on the glacier, on the right the streamline with the highest velocity is determined. The latter will be used as reference flowline.

The FRS is used throughout all of the post-processing and allows an optimized processing for outlet glaciers.

3.3.2. TERMINUS POSITION

The terminus line is manually digitized for each of the resampled GRD images, that are described in Section 3.2.4. Here we elaborate how the terminus line is converted to a representative position, and we discuss the accuracy of digitization process. The terminus position is not only important to analyse the retreat/advance of a glacier, but they also act as input during the post-processing of the estimated offsets. The digitized line allows to classify which offsets are located on the glacier and which ones are located on the water.

As the terminus position is defined by a line, it can be hard to express retreat/advance due to an irregular geometry. Therefore, an Equivalent Terminus Position (ETP) is introduced that represents the terminus line.

In literature (Carr et al., 2013a, Moon and Joughin, 2008, Moon et al., 2014) the box-method is the common method to express such a ETP, using a geometric method based on a rectangular box that is fitted by the fjord (see Figure 3.11). By calculating the area covered by ice and dividing this by the box width, a ETP is obtained. This can be seen as the geometrical equivalent of calculating the mean, thereby accounting for the inconsistent sampling of the digitized terminus line.

However, it is chosen not to use the box method because it has two important disadvantages: 1) the box-method does not allow to define a curved centerline and 2) information outside the rectangular box is not taken into account in estimating a representative point. Both disadvantages are negligible for straight fjords but become a bigger error source for curved fjords. As most fjords in the North (Rink Isbræ, Inngia Isbræ, Umiammakku Isbræ) have a curved topography, this method will not lead to a proper ETP. A more accurate approach is to reference the terminus position to the curved flowline discussed in Section 3.3.1. By interpolating the inconsistent sampling to an equal-interval sampling of the terminus line, the mean along-track position of the terminus line is used as ETP. An illustration is given in Figure 3.11, and the results are compared in Figure 3.12. For a straight fjord, the box method and flowline method are similar, but in curved fjords the flowline method is taking into account the curvature. For Lille Gletscher, the flowline method estimated a larger retreat of the ETP was found (up to 200%) with respect to the box method. However, the difference between the two methods is not a constant factor, but dependent on the geometry of the terminus line and the curvature of the fjord. The flowline improves the estimated ETP up to a factor two.

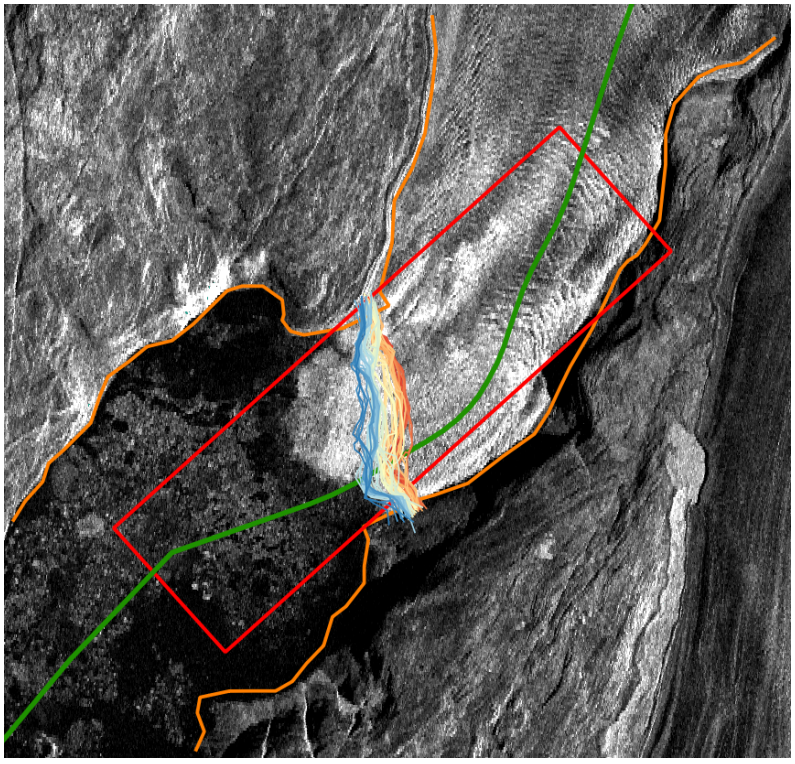

Figure 3.11: An overview of Støre Gletscher. Red is the reference box, used for the box method, and black is the flowline. The digitized terminus positions are blue. In the box method the area of ice is calculated and divided by the width of the reference box, that leads to a representative point with respect to the 'arbitrary' start line. With the flowline method, the average position is calculated on the flowline (black line). This means that also the areas outside the red box are taken into account and the the orientation is not fixed.

ERROR SOURCES OF DIGITIZATION PROCESS

Manual digitization is required to digitize the terminus position. Although water and ice can be distinguished clearly, sea ice and glacier ice cannot be distinguished easily. This makes it difficult for automated computer estimations, and therefore this process is commonly done manually by drawing a line along the terminus line. Even manually this process can be difficult, especially in spring (April/May) when both the sea ice as well as the glacier ice are melting and they both appear dark in the image. To improve this process a false color image (assigning different images to rgb-bands) can be used by combining the current image with the

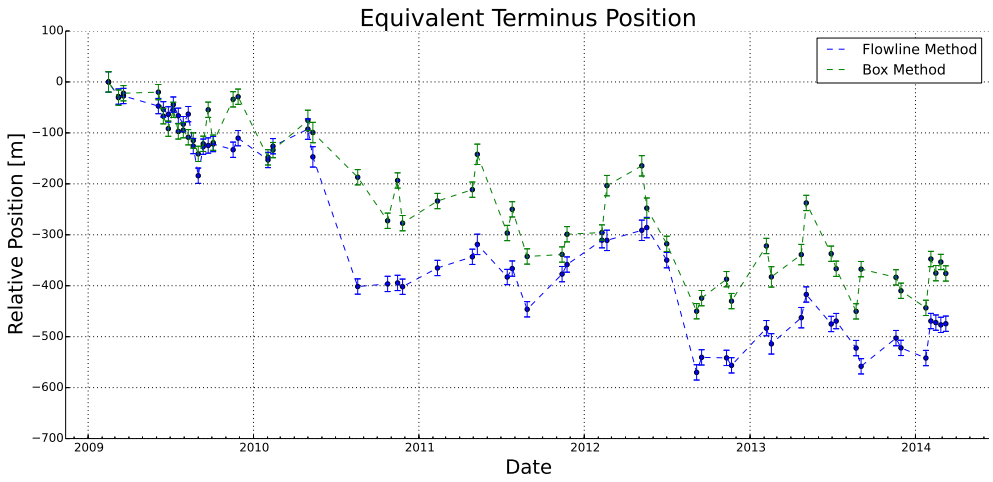

Figure 3.12: A comparison between the results of the box method and the flowline method of the digitization of TerraSAR-X on Lille Gletscher. Blue denotes the flowline method, while green denotes the box method. There is a difference because Lille Gletscher lies in a curved fjord, meaning that is difficult to define a representative box for the box-method.

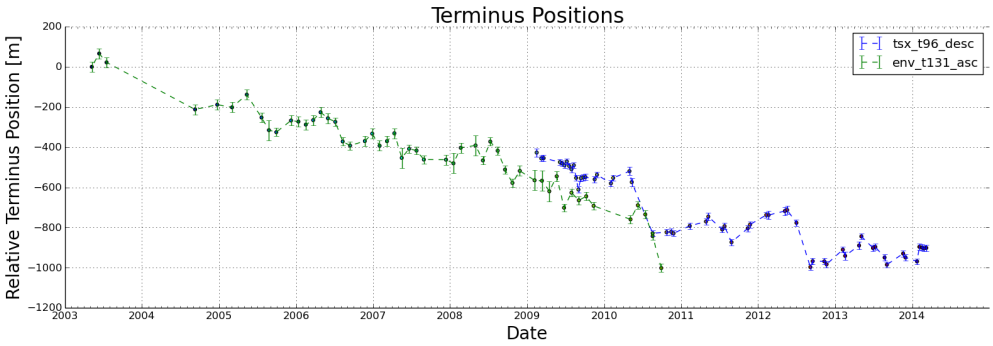

Figure 3.13: The terminus position record of Lille Gletscher. Here it can be seen that there is a bias between Envisat and TerraSAR-X observations, and that is not a constant bias in time.

previous image. This helps to distinguish the new terminus position using the old one. During digitization a grade expressing the difficulty of the digitization is noted:

- **Grade 1:** perfect conditions, accurate digitization possible.
- **Grade 2:** difficult conditions, but terminus line was visible.
- **Grade 3:** no clear line was visible, a part had to be digitized using input from older/newer images.
- **Grade 4:** overlay was making digitization difficult, only gives an rough idea where the terminus is located.

The digitized positions are saved, per stack and per glacier.

As the terminus positions are digitized manually, this process might be subject to human digitization errors. In order to analyse and quantify the error made in this process, three tests were done:

1. **Resolution related errors** are tested by digitizing a stable mountain section using two different satellites (TSX and Envisat).
2. **Person-related errors** were tested by digitizing a stable mountain section by two different persons (using TSX).

3. **Condition-related errors** are tested by digitizing a terminus position twice using the same satellite (done for both TSX and Envisat).

In test 1 a mountain section, without overlay effects, is digitized with a descending TSX stack and an ascending Envisat stack. As a rigid mountain section is digitized, and not a moving terminus, the different orbit modes should not influence the position of the mountain section in the image due to DEM related bias as discussed in Section 2.3.4. The ETP is then calculated and the results are compared in table 3.2. As expected, the standard deviation of TSX (≈ 14 m) is better than that of Envisat (≈ 21), and the observed difference (≈ 12 m) falls within the standard deviation. The standard deviation of TSX is approximately 2 times better than for Envisat, but its spatial resolution several factors better (see Table 2.2) A coarser resolution decreases the ETP accuracy, but not on a one to one ratio.

Table 3.2: Results of digitization test 1: a comparison of two different resolutions. The ETP position is referenced to the first ETP for both digitization sets. The mean ETP position is therefore with respect to the first digitization.

Digitization Set	Mean ETP position [m]	Standard Deviation [m]
TSX t96 desc	24.0	13.9
ENV t131 asc	11.9	20.9

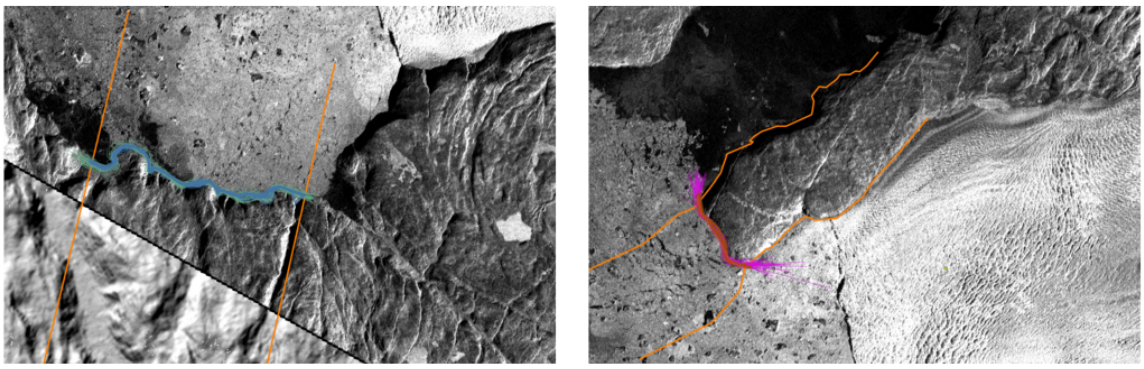

Figure 3.14: The digitization of a stationary scenery, in this case two mountains. The left is test 1, digitized using both TerraSAR-X and Envisat and right is test 2, digitized three times from TerraSAR-X images.

The second test is done by digitization another mountain section with TSX by two different persons. The results can be found in Table 3.3 and show that there is little difference between the two persons.

Table 3.3: Results of digitization test 2: comparison between ETP digitized by two persons. The ETP position is referenced to the first ETP for both digitization sets. The mean ETP position is therefore with respect to the first digitization.

Digitization Set	Mean ETP position [m]	Standard Deviation [m]
TSX t96 desc Person 1	-3.6	16.9
TSX t96 desc Person 2	-5.71	14.7

The third test is done by digitizing a glacier twice, by the same satellite. For Envisat this is done on Rink Isbræ with two stacks (one with and one without layover effects) and for TSX this is done for Støre Gletscher with one stack. The results can be found in Table 3.4 and show that a high difficulty or layover significantly increase the digitization, while grade 1 and 2 have relatively the same accuracy.

In order to quantify the accuracy of a terminus digitization, the statistics from Table 3.2, 3.3 and 3.4 are used. The grades that are assigned during digitization, listed in Section 3.3.2, are converted to accuracy using Table 3.5.

In conclusion, the terminus position is represented by the Equivalent Terminus Position (ETP) using a flowline. This method represents the terminus position better than the box-method, up to a factor two. The error sources of the manual digitization have been assessed, and have shown to be accurate with respect to the expected variations.

Table 3.4: Results of digitization test 3: comparison of repeated digitizations. The ETP position is referenced to the first ETP for both digitization sets. The mean ETP position is therefore with respect to the first digitization.

Digitization Set	Glacier	Mean ETP Difference [m]	Mean ETP Difference Grade 1 [m]	Mean ETP Difference Grade 2 [m]	Mean ETP Difference Grade 3 [m]	Mean ETP Difference Grade 4 [m]
ENV t131 asc	Rink Isbræ	20.85	18.66	26.37	45.23	-
ENV t254 desc	Rink Isbræ	55.97	-	-	-	55.97
TSX t96 dec	Støre Gletscher	18.96	14.49	18.54	40.12	55.97

Table 3.5: The accuracy of the digitization per satellite. *No overlay is present in TerraSAR-X images above glaciers terminus positions, this is mainly due to suitable orbit modes.

Satellite	Accuracy Grade 1 [m]	Accuracy Grade 2 [m]	Accuracy Grade 3 [m]	Accuracy Grade 4 [m]
ERS	20	25	50	60
Envisat	20	25	50	60
TerraSAR-X	15	20	40	-*

3.3.3. GEOCODING OFFSETS

During the post-processing, the estimated offsets are translated to a representative glacier velocity. This is done using the flow as depicted in Figure 3.7. In order to estimate glacier flow velocity, the estimated offsets from Section 3.2.3 have to be processed. The second step is to geocode the estimated offsets.

The ICC offset tracking in DORIS estimates offsets in line and pixel. These offsets have to be converted to offsets in meters. In order to calculate the offsets in meters, the acquisition geometry and pixel spacing is used to project the offsets on the Earth. This is the same approach as used by Gray et al. (2001).

Consider a 3D surface displacement δ, as depicted in Figure 3.15 and 3.16. Using SAR data, this displacement is estimated by two components, that is, an offset in azimuth δ_{az} and an offset in slant range δ_{sr}. So a 2D offset in radar coordinates represents a 3D surface motion, which leads to the following system of equations:

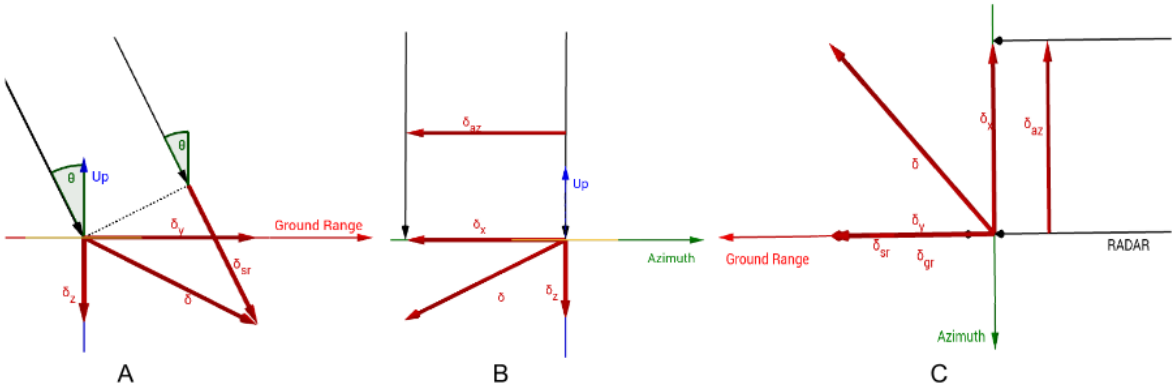

Figure 3.15: Three 2D overviews of the offset geometry. A) ground range vs up, B) azimuth vs .up and C) ground range vs azimuth. In A it is clear that slant range contains both a y (ground range) and an upward component. Based on the incidence angle and slope, one is able to decompose the estimated offset.

$$\begin{pmatrix} \delta_{sr} \\ \delta_{az} \end{pmatrix} = \begin{pmatrix} 0 & \sin(\theta) & -\cos(\theta) \\ 1 & 0 & 0 \end{pmatrix} \begin{pmatrix} \delta_x \\ \delta_y \\ \delta_z \end{pmatrix}. \tag{3.1}$$

Here θ is the local incidence angle and δ_x, δ_y denote offsets parallel to the azimuth and range direction within a radar frame, and δ_z the local vertical component. As this is a system with 2 knowns and 3 unknowns, it cannot be solved. Either one should obtain more measurements to obtain a 3D motion, or an assumption has to be made. A common assumption is to assume a 'surface parallel flow', by using the slope information from the DEM+:

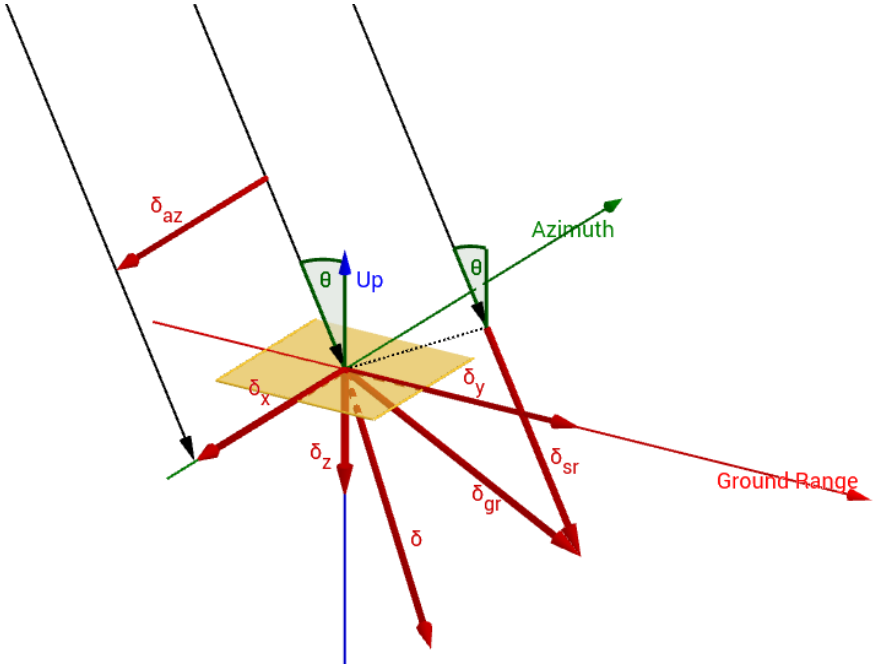

Figure 3.16: A 3D overview of the offset geometry. The ground motion δ can be decomposed into a ground motion in azimuth δ_x, a ground motion in range(δ_y and a vertical motion δ_z. In radar coordinates this 3D motion is decomposed in to azimuth δ_{az} and range δ_{sr}.

$$\delta_z = \delta_x S_{\text{az}} + \delta_y S_{\text{sr}}, \tag{3.2}$$

where S_{az} and S_{sr} represent the local azimuth and range slopes, which are determined using:

$$S_{\text{az}} = \frac{\delta_z}{\Delta_{\text{az}}}, \tag{3.3a}$$

$$S_{\text{sr}} = \frac{\delta_z}{\Delta_{\text{sr}}}. \tag{3.3b}$$

Here Δ_{az} and Δ_{sr} are the spacing in azimuth and slant range respectively. In order to determine the height component δ_z, the radarcoded DEM+ is interpolated using the old and new position of the offset:

$$\delta_z = f_{\text{DEM+}}(L_{\text{new}}, P_{\text{new}}) - f_{\text{DEM+}}(L_{\text{old}}, P_{\text{old}}), \tag{3.4}$$

where $f_{\text{DEM+}}$ is an interpolation function of the radarcoded DEM+. The new system of equations now becomes:

$$\begin{pmatrix} \delta_{sr} \\ \delta_{az} \end{pmatrix} = \begin{pmatrix} S_{\text{az}} \sin(\theta) & \sin(\theta) - S_{\text{sr}} \cos(\theta) \\ 1 & 0 \end{pmatrix} \begin{pmatrix} \delta_x \\ \delta_y \end{pmatrix}. \tag{3.5}$$

This system can be solved to obtain offsets in x and y directions, hence $\delta_{az} = \delta_x$ and δ_{sr} can be calculated based on δ_x and δ_y. These offsets are in azimuth and range directions, hence the satellite heading has to be used in order to calculate offsets in North and East components:

$$\begin{pmatrix} \delta_x \\ \delta_y \end{pmatrix} = \begin{pmatrix} \cos(\psi) & -\sin(\psi) \\ \sin(\psi) & \cos(\psi) \end{pmatrix} \begin{pmatrix} \delta_N \\ \delta_E \end{pmatrix}. \tag{3.6}$$

The advantage of this method is that it allows for (zero-order) error propagation and takes into account the slope geometry. When the slope is unfavourably with respect to the incidence angle of the satellite, the $\sin(\theta) - S_r \cos(\theta) \approx 0$ and the ground range δ_y becomes poorly conditioned, resulting in large values (up to infinity). A disadvantage of this uniquely determined system is that errors in the slope estimate, directly

propagate to the calculated offsets. Hence, a good assessment of this slope estimation quality is required to provide a representative quality description.

Finally, the total offset can be calculated using:

$$\delta = \sqrt{\delta_x^2 + \delta_y^2 + \delta_z^2}. \tag{3.7}$$

ERROR PROPAGATION

Error propagation is used to provide a quality description of the results. This quality description is subsequently used in a filtering step of the offsets, where outliers are removed. In Section 3.3.5, the theoretical accuracy of ICC tracking was given as (De Zan, 2014):

$$\sigma_{\tilde{\text{ICC}}} = \sqrt{\frac{3}{10N}} \sqrt{\frac{2+5\gamma^2-7\gamma^4}{\pi\gamma^2}}, \tag{3.8}$$

where N is the number of independent samples per window and γ is the interferometric coherence. More samples means a better accuracy. In order to obtain a standard deviation with the same unit as pixel spacing, one has to consider the pixel size and oversampling ratio (Gray et al., 2001):

$$\sigma_{\text{ICC}} = \sigma_{\tilde{\text{ICC}}} osf^{3/2} \Delta, \tag{3.9}$$

where osf is the oversampling ratio and Δ is the pixel spacing in range or in azimuth, meaning that the offset in line and in range is different depending on their pixel spacing. There is a different accuracy in range and azimuth, and this also holds that the direction of a displacement vector is an important factor for its accuracy. The theoretical accuracy that is achieved by amplitude tracking for ERS, Envisat and TerraSAR-X using the windows from Table 3.1 is depicted in Figure 3.17.

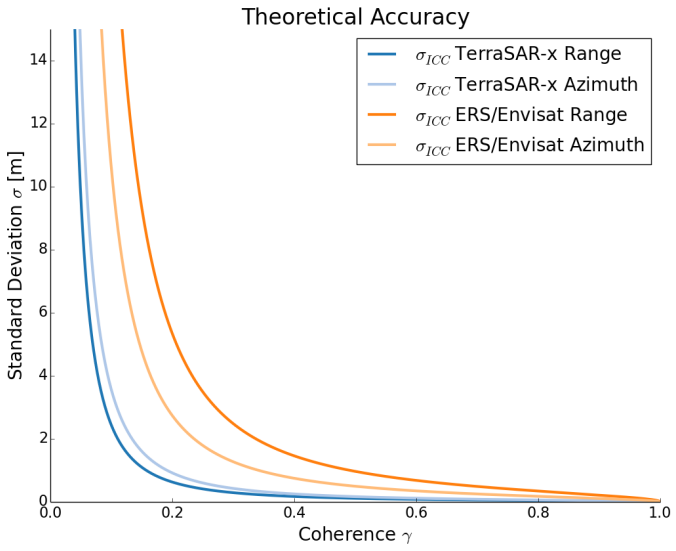

Figure 3.17: Theoretical accuracy of ICC offset tracking for ERS, Envisat and TerraSAR-X. As ERS and Envisat have comparable specifications, their theoretical accuracy is almost the same.

Using Equation 3.5 error propagation can be applied using:

$$Q_{\hat{x}\hat{x}} = (A^T Q_{yy}^{-1} A)^{-1}, \tag{3.10}$$

where Q_{yy} is the covariance matrix of the observed pixel and line offsets and $Q_{\hat{x}\hat{x}}$ the covariance matrix of the calculated offsets in x and y. Similarly, error propagation can be applied on Equation 3.6.

In this approach it is assumed that the derivation of slope, using an interpolation, is deterministic and does not introduce errors. This error is probably smaller than the standard deviation of the amplitude tracking itself. A constant absolute error of the DEM is cancelled out because the slope is a relative measure (difference between original and new location of the displacement), hence only relative height errors are important. The assumption is made that relative errors at close distance are relatively small (Reeh et al., 1999). The error is divided by the estimated offset to obtain a slope, meaning a relatively small slope error for large offsets.

The geocoding of the estimated offsets is the second step of five to translate the estimated offsets to a representative glacier velocity (see Figure 3.7). With the geocoded offsets, a more glacier-specific processing can be performed.

3.3.4. POST-PROCESSING OFFSETS

Post-processing of the offsets is the third step of five (see Figure 3.7), where the estimated offsets per glacier are selected, referenced to the FRS and a quality assessment of the coregistration is performed. This step can be seen as an administrative one, one which the next steps can continue.

The offsets are selected at a specific glacier (using the buffer box that is used to generate the offset windows, see Section 3.2.3). Then they are referenced to the FRS and classified based on the GIMP land-classification. To assess the quality of the coregistration, a selection is made of offsets that are located on the mountains, based on the land-classification, and that show a high correlation (>0.4). These points should, as they are stationary and highly correlated, show a small motion in the order of $\tilde{0}.1$ pixel. Based on these points an analysis is performed on the quality of the coregistration of the image. Images that are not properly coregistrated can be discarded.

As mentioned before, this step is more an administrative one to tell which offsets are on which glacier, and to see if the image has been coregistrated properly.

3.3.5. FILTERING OFFSETS

Filtering is the fourth step to translate the estimated offsets into a representative glacier velocity (see Figure 3.7). Here the outliers are detected and removed from the datasets. If this step would be skipped, the representative glacier velocity would contain a lot of noise. For TerraSAR-X this step is unnecessary as the offset estimates from 11-day, 22-day and 33-day pairs show hardly any outliers. But for ERS-1/2 and Envisat this is not the case, and many outliers are found. This can be explained by some factors:

- **The larger temporal baseline (11-days vs 35-days)** leads to more temporal decorrelation.
- **C-band might be more sensitive to decorrelation** than X-band, although its penetration depth is larger.

In order to filter out bad observations, a filtering operation is implemented. As the goal is to estimate a representative velocity at a point along the flowline, as described in Section 3.3.6, the problem is simplified to a 1D velocity profile along-track, see Figure 3.18. Observations within 500 m from the flowline are considered for this purpose. Although outside the scope of this study, the principle could also be extended on the entire spatial coverage of the glacier by taking both the along-track and across-track velocity profile.

The filtering algorithm is considered in three stages. At first, the accuracy of the offset tracking is discussed. Thereafter, the concept of idealisation precision is used to account for the glaciers variability next to the measurement variability. Finally, the outlier detection and removal is considered.

ACCURACY OF ICC OFFSET TRACKING

The theoretical accuracy of ICC is described by De Zan (2014) according to Equation 3.8. Conclusively, the accuracy of ICC offset tracking is related to the coherence of the fit and the number of samples. A higher coherence or a larger number of samples will both lead to an higher accuracy of the offset. Complex coherence is described by (Kampes and Usai, 1999):

$$\gamma = \frac{E\{M \cdot S^*\}}{\sqrt{E\{M \cdot M^*\}\dot{E}\{S \cdot S^*\}}}. \tag{3.11}$$

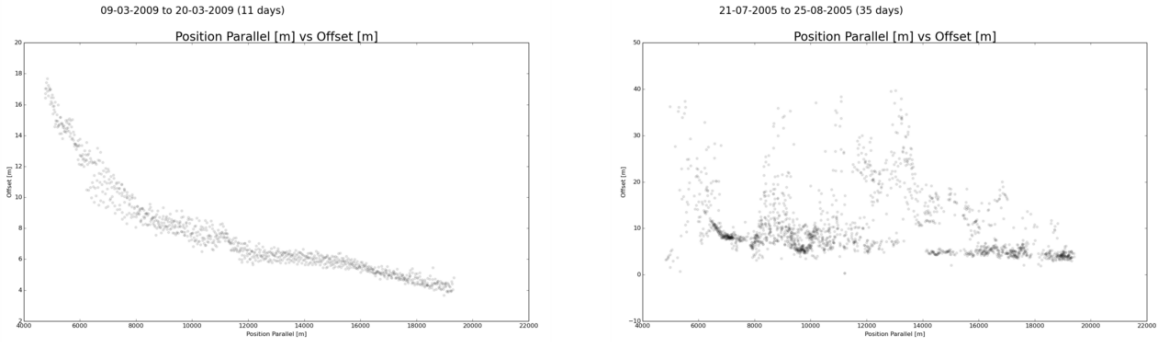

Figure 3.18: The along-track velocity profile for TerraSAR-X (left) and Envisat (right). The Envisat estimates show much more noise, but the same signal is visible.

Here M and S denote the complex master and slave respectively and M^* and S^* denote the complex master and slave conjugates. DORIS calculates for each window the correlation instead of the coherence. According to the manual the correlation per window is described by:

$$\Gamma = \frac{E\{M \cdot S^*\} - E\{M\}E\{S^*\}}{\sqrt{(E\{M \cdot M^*\} - E\{M\}E\{M^*\}) \cdot (E\{S \cdot S^*\} - E\{S\}E\{S^*\})}}. \tag{3.12}$$

So the difference between coherence and correlation is that the mean values are subtracted first. Coherence and correlation are equal when $E\{M\} = E\{S\} = 0$. According to equation 2.12 this is the case, if one assumes that N is sufficiently large to comply to the central limit theorem. For windows with only a few independent samples this will not be the case.

MODEL, SIGNAL AND NOISE

Here the concept of idealisation precision is used for filtering outliers. Observations can be very precise, but the nature of the observed target determines the maximum achievable precision. The ice flow varies both in time and in space, but it is a natural and unpredictable process. The implication of this unpredictable boundary is that outliers are more difficult to identify, as abnormal observations can both be related to a physical process or to an outlier. In order to remove outliers, an outlier detection is applied that allows for ice flow variability by differentiating between model, signal and noise. The flow variability is estimated by using 'ideal' TerraSAR-X estimations, that have little to no outliers.

The model used during this filtering step is not based on a physical model, as too many factors and processes are influencing the glacier, but on a statistical relation between along-track position and off-track position. Although glacier flow can be modelled to a certain extend, there will be a factor of model imperfection and randomness of natural processes. The better this profile is modelled and described, the lower this variability with respect to the model will be. All variations outside this model are captured in a signal-model, based on a covariance function. The estimated offsets can then be described by (Teunissen et al., 2004):

$$y = Ax + s + n, \tag{3.13}$$

where y are the observations, Ax is the model consisting of design matrix A and parameter vector x, and n is the measurements noise. The vector s is the defined as a stochastic signal that is added to the deterministic model Ax. When the covariance matrix of the signal Q_{ss} is known, the model parameters can be estimated:

$$\hat{x} = (A^T(Q_{ss} + Q_{nn})^{-1}A)^{-1}A^T(Q_{ss} + Q_{nn})^{-1}y. \tag{3.14}$$

Hence, the model evaluated at the observation locations is then described by:

$$\hat{y} = A\hat{x}, \tag{3.15}$$

and the residuals are defined as:

$$\hat{e} = y - \hat{y} = y - A\hat{x}. \tag{3.16}$$

The signal s can be predicted by:

$$\hat{s} = Q_{s's}(Q_{ss} + Q_{nn})^{-1}\hat{e}, \tag{3.17}$$

where $Q_{s's}$ is the covariance matrix between a point of interest with respect to observation points (Teunissen et al., 2004).

Using this system, the glacier variability that is not captured by the model is described by a signal component. If the signal component is left out, there is a chance that too many observations are marked as outlier because the noise level of the estimated offsets, i.e., the measurements, is not sufficient to allow these variations.

The signal variations will differ per glacier and might also change in time, but have to be quantified in order to take them into account. It is chosen to consider the 11-day TerraSAR-X observations as representative to determine the covariance of the signal for each glaciers (no temporal variation of the coveriance is taken into account). Hence, the glaciers studied in this research are limited to the glaciers in the Uummannaq-region that are covered by TerraSAR-X.

A covariance model can be estimated by fitting the experimental covariance, by comparing the covariance between two (detrended) observations to their relative distance. The experimental covariance c between two observations can be calculated using (Lindenbergh, 2012):

$$c_{ij} = (z_i - \mu)(z_j - \mu), \tag{3.18}$$

where z_i is observation i that is compared to z_j (observation j), and μ is the average of all observations. As this will give a scattered result, see Figure 3.19, covariance is averaged in bins in order to obtain an average result per distance (Lindenbergh, 2012):

$$c_{h_k} = \frac{1}{N_k}\sum_{\epsilon h_k}(z_i - \mu)(z_j - \mu), \tag{3.19}$$

where h_k is the distance interval ($h_1 = [0, w], h_2 = [w, 2w], ...$). Using these binned values a covariance function can be fitted. An exponential and Gaussian function are considered for estimation (Lindenbergh, 2012):

$$c_{\text{exp}}(h) = \sigma^2(e^{-\frac{3h}{R}}), \tag{3.20a}$$

$$c_{\text{gauss}}(h) = \sigma^2(e^{-\frac{(3h)^2}{R^2}}). \tag{3.20b}$$

Here σ is the sill, equal to the variance, and R is the range at which observations are considered uncorrelated. Both models are considered and tested, but the exponential models gives better results. In Figure 3.19 an example of the exponential covariance fit is given.

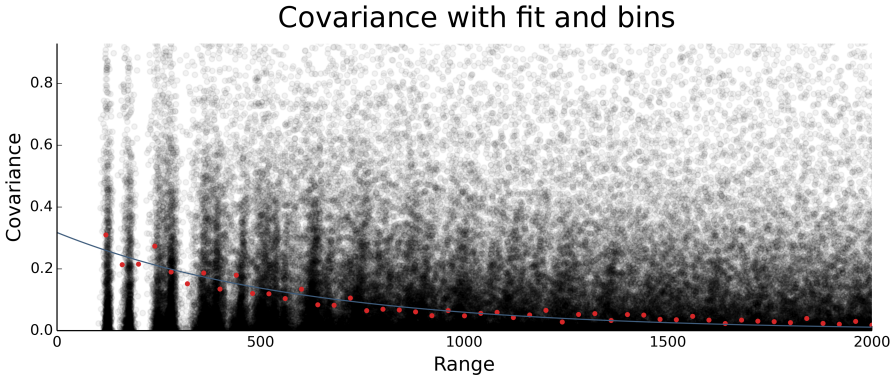

Figure 3.19: The covariance for an 11-day TerraSAR-X pair of Støre Gletscher.

The covariance models are an important characteristic of each glacier, they tell what the along-track flow variability is of the glacier.

MODEL TESTING AND OUTLIER REMOVAL

Using the measurement accuracy and the covariance model, the signal-model from Equation 3.13 is defined. The outliers can now be detected and removed based on knowledge on the flow variability along the flowline. The covariance model estimated before, allows to take the signal and noise (co)variance into account during filtering. As a filter, the w-test is implemented to filter outliers based on a glacier velocity model (Teunissen et al., 2004). The filtering is performed in a iterative process to validate the model fit based on a test statistic and, if rejected, to detect outliers based on their w-test value. First, a model is fitted using a BLUE (Best Linear Unbiased Estimator):

$$\hat{x} = (A^T Q_{yy}^{-1} A)^{-1} A^T Q_{yy}^{-1} y, \tag{3.21}$$

where y are the observed velocities, A is the design matrix (defining the model) and Q_{yy} is the covariance matrix defined as $Q_{yy} = Q_{ss} + Q_{nn}$ (Equation 3.14) with the σ^2_{ICC} on the diagonal of Q_{nn} (see equation 3.9). After this an overall model test is applied to test if the model is accepted. This is done by comparing the test statistic T to a critical value k_α (Teunissen et al., 2004):

$$T = \hat{e}^T Q_{yy}^{-1} \hat{e} \tag{3.22}$$

$$k_\alpha = \chi^2(1-\alpha, b), \tag{3.23}$$

wwhere b is the redundancy and α the level of significance. When the test is rejected ($T > k_\alpha$), an outlier detection is applied using the w-test:

$$w = \frac{c_y^T Q_{yy}^{-1} \hat{e}}{\sqrt{c_y^T Q_{yy}^{-1} Q_{\hat{e}\hat{e}}^{-1} Q_{yy}^{-1} c_y}}. \tag{3.24}$$

The value with the largest w-value is rejected and the sequence starts again with an overall model test, until the model is accepted.

The implementation of this process is done in the following order. First for each 11-day TerraSAR-X pair the following scheme is applied:

1. BLUE estimation without signal covariance: $\hat{x} = (A^T Q_{nn}^{-1} A)^{-1} A^T Q_{nn}^{-1} y$
2. Calculation of experimental covariance based on residuals: $\hat{e} = y - A\hat{x}$
3. Covariance model estimation by fitting the experimental covariance bins
4. Apply model test
   (a) If rejected: outlier detection and removal, go back to step 1
   (b) If accepted: accept covariance model

When this process is applied for all 11-day TerraSAR-X observations, there are several estimated covariance functions. The median sill and range is then used as 'representative' for the covariance function of the glacier, see Figure 3.20. The results for Sermilik are depicted in Figure 3.21.

After estimating a covariance model using estimated offsets from the 11-day TerraSAR-X pairs, the estimated offsets from the other pairs can be filtered. This is done using the following sequence:

1. Apply model test
   (a) If rejected: outlier detection and removal, go back to step 1
   (b) If accepted: accept covariance model

With this way of filtering, the velocity profile of the ERS and Envisat data becomes better. Unfortunately, some pairs simply a lot of outliers that lead to gaps in the velocity profile.

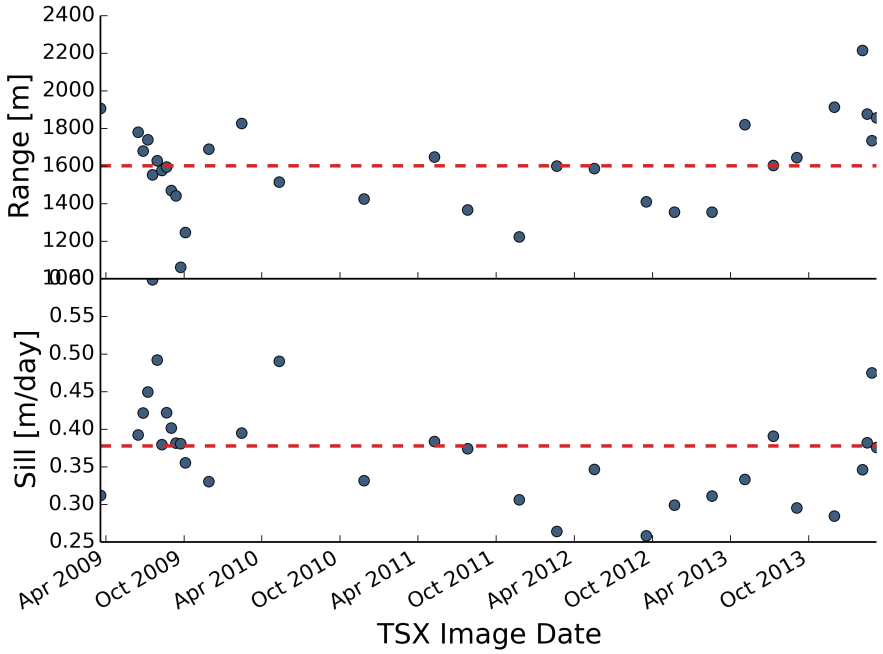

Figure 3.20: The range and sill estimated for each 11-day TerraSAR-X pair. The red line indicated the median value that is used as representative covariance function of Støre Gletscher.

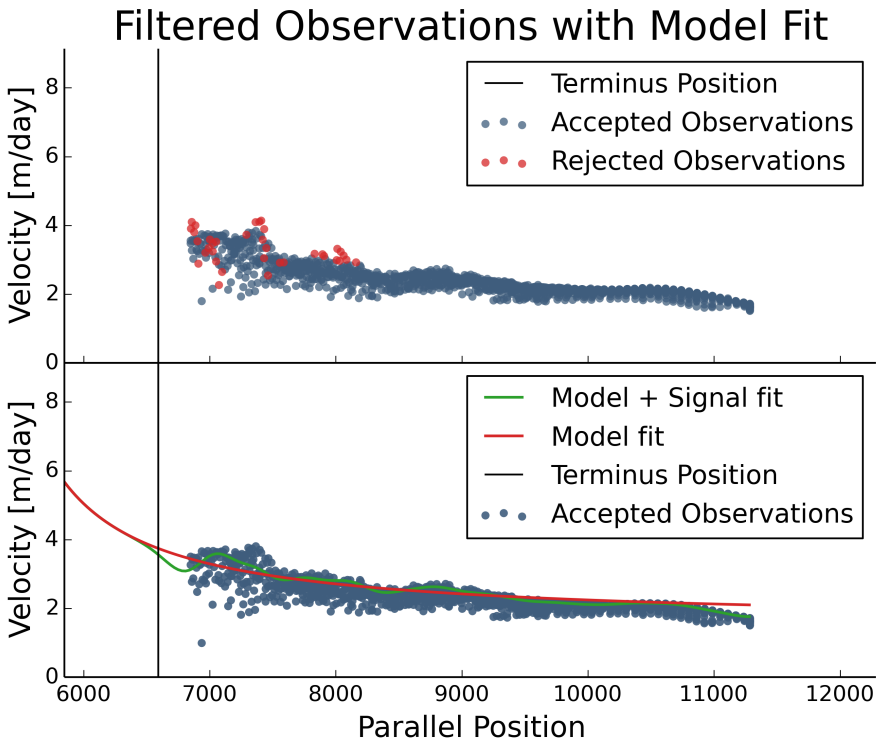

Figure 3.21: Estimated model parameters for a 11-day TerraSAR-X pair above Sermilik. The upper graph shows the raw observations, with blue the accepted and red the rejected ones. Below a model fit is shown, in red the model and in the green is the predicted signal.

3.3.6. EQUIVALENT GLACIER VELOCITY

The last step in translating the estimated offsets to useful information, is by summarizing the glacier flow velocity as one value. sAt this point, the glacier flow velocity is estimated and filtered, but the goal of the research is to compare different glaciers and their velocities over time. A representative velocity value has to

be found so the glaciers can be compared, which is here defined as the Equivalent Glacier Velocity (EGV). Different authors have used different points to estimate this representative velocity:

- **Moon et al. (2014):** "Measurements were taken at a fixed location roughly one half width from the terminus, with adjustments to minimize missing data and account for changing terminus position"
- **Howat et al. (2010):** "... the median speed value within a 1 km^2 area of the center of each glacier trunk, 4–6 km from the ice front, ..."
- **Carr et al. (2013a):** uses the Measures dataset from Joughin et al. (2010a): "Mean ice velocities were sampled within a 1 km^2 box, which was centered on and orientated parallel to the glacier centerlines and located 1 km from the glacier terminus."
- **Rignot and Mouginot (2012):** "Speed is reported at the ice front for tidewater and lake-terminating glaciers"

So in conclusion, there are 4 different points considered where a representative value is considered, but the questions remains whether this EGV is comparable between glaciers, between different literature sources, and if it remains comparable in time. Although this will not be answered in this project, the need for a generally accepted method for determining a EGV is underlined. This could be a point estimate, but maybe a non-parametric value or a properly defined flux estimate can be defined.

Here we have chosen to use the width of the terminus to find a representative point on the glacier, as used by Moon et al. (2014). The advantage of this method that there is a form of scaling, that helps to compare glacier to glacier velocity. However, ERS and Envisat velocity estimates are noisy and have gaps in their coverage. This holds that there is not always a choice of where a velocity box is placed, but it is limited to a location where most estimates can found. In Table 3.6 an overview is given of which locations are used for the seven glaciers in this study. The estimated offsets in this velocity box are used to estimate the mean velocity and standard deviation.

Table 3.6: The position along-track and area of the velocity box for the different glaciers. The along-track position is expressed as a factor of the terminus width. *At Umiammakku Isbræ, layover effects made it difficult to find a location close to the glacier front.

Glacier	**Position** [-]	**Area** [km^2]
Støre Gletscher	1	25
Lille Gletscher	1.5	0.25
Sermilik	0.75	1
Kangerlussuup Sermersua	0.75	1
Rink Isbræ	0.5	1
Umiammakku Isbræ	2*	1
Inngia Isbræ	0.5	1

In Figure 3.22 an overview is given of the velocity at different along-track positions for Støre Gletscher, in order to assess the consequence of along track velocity variations. It can be observed that observations at the terminus front are more likely to have outliers, and that error bars not necessarily decrease when lower velocities are considered. This is because there are two processes that influence the error bar:

- A high velocity area means that the ICC offset tracking estimates large offsets. A large offset is relatively more accurate compared to a smaller offset with the same correlation, and thus the same standard deviation. This means that small offsets, within the region of the error bar, are difficult to capture. This is a problem for ERS and Envisat at locations where the velocity is low.
- A high velocity area means that decorrelation is likely to occur quicker, thereby increasing the standard deviation of the estimated offsets.

The ideal position would be where the velocities are high, but the decorrelation occurs slowly.

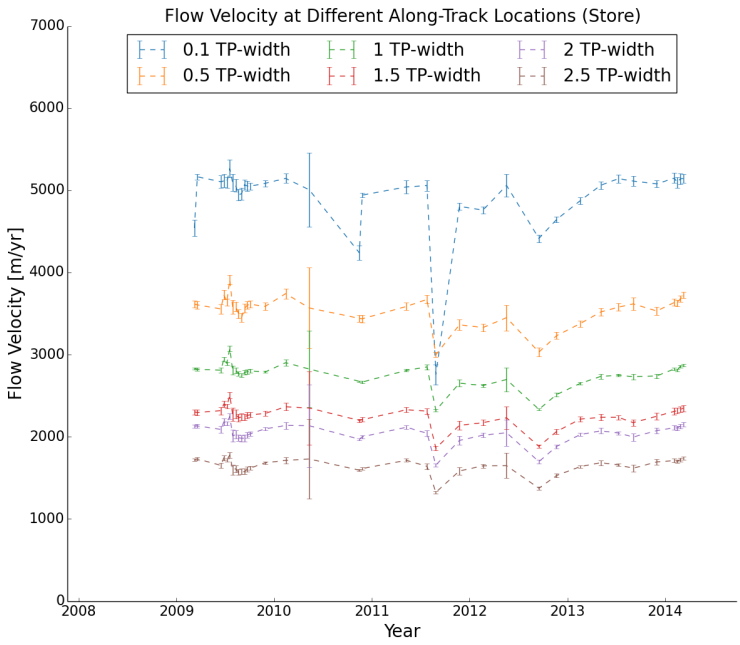

Figure 3.22: The estimated velocities for Støre Gletscher at different locations along the flowline. The location is determined based on the terminus-width.

4

RESULTS AND ANALYSIS

In this chapter the results are presented and analysed. The observed glacier evolution in Section 4.1 is presented, followed by an analysis of the climatic forcing of SST, SAT and SIF in Section 4.2 and a description of the glacier-specific factors in Section 4.3. In Section 4.4 a synthesis is given, where glacier evolution is evaluated based on climate forcing and glacier-specific factors.

4.1. GLACIER EVOLUTION

Here the observed glacier records of terminus position and flow velocity, are described. All the detailed glacier records can be found in Appendix A.

In Figure 4.1 the digitized terminus positions are visualized for all glaciers. It is observed that none of the glaciers shows long-term advance, four glaciers (Støre Gletscher, Sermilik, Kangerlussuup Sermersua and Rink Isbræ) stay relatively stable and three glaciers show a long term retreat (Lille Gletscher, Umiammakku Isbræ and Inngia Isbræ). During the 1990's, all the terminus positions of all glaciers are observed to be stable, although there are big data gaps during this period. It can be suggested that Inngia Isbræ shows a slight advance during this period, although there are only sparse observations. Lille Gletscher is the first that shows retreat, starting around 2001 and with increasing pace after 2003. Umiammakku Isbræ and Inngia Isbræ start their retreat in 2003, and Umiammakku Isbræ finds a stable position in 2010, whereas Inngia Isbræ keeps retreating until the last record in 2014. It is observed that the Inngia Isbræ also accelerated it's retreat around 2011.

A seasonal motion of the terminus position is observed at all glaciers, with advance during winter periods and retreat during summer periods. Rink Isbræ shows the strongest seasonal signal with a seasonal amplitude of about 500 m. Støre Gletscher also shows a seasonal signal, although there are more fluctuations during the season. The retreating glaciers, Lille Gletscher, Umiammakku Isbræ and Inngia Isbræ, all have a seasonal signal, but not more or less than stable glaciers.

The observed velocity profiles are depicted in Figure 4.2. Rink Isbræ and Støre Gletscher are the fastest glaciers, and their velocities are in agreement with earlier results (see Table 2.1). Here it should be noted that the EGV of Støre Gletscher is lower compared to literature because a point further from the terminus position was used. A long-term acceleration is observed at Inngia Isbræ: around 500 m/yr in the early 90's to around 1500 m/yr in 2010. The acceleration coincides with the retreat in 2003 and shows a linear trend. The estimated velocities at Sermilik and Lille Gletscher indicate to have slightly accelerated from 500 m/yr in the 90's to almost 1000 m/yr in 2003 and 400 m/yr in the 90's to 500 m/yr in 2010. It should be noted that the estimated velocity on Umiammakku Isbræ is determined at two times the width of the terminus (approx 6 to 9 km) due to layover effects.

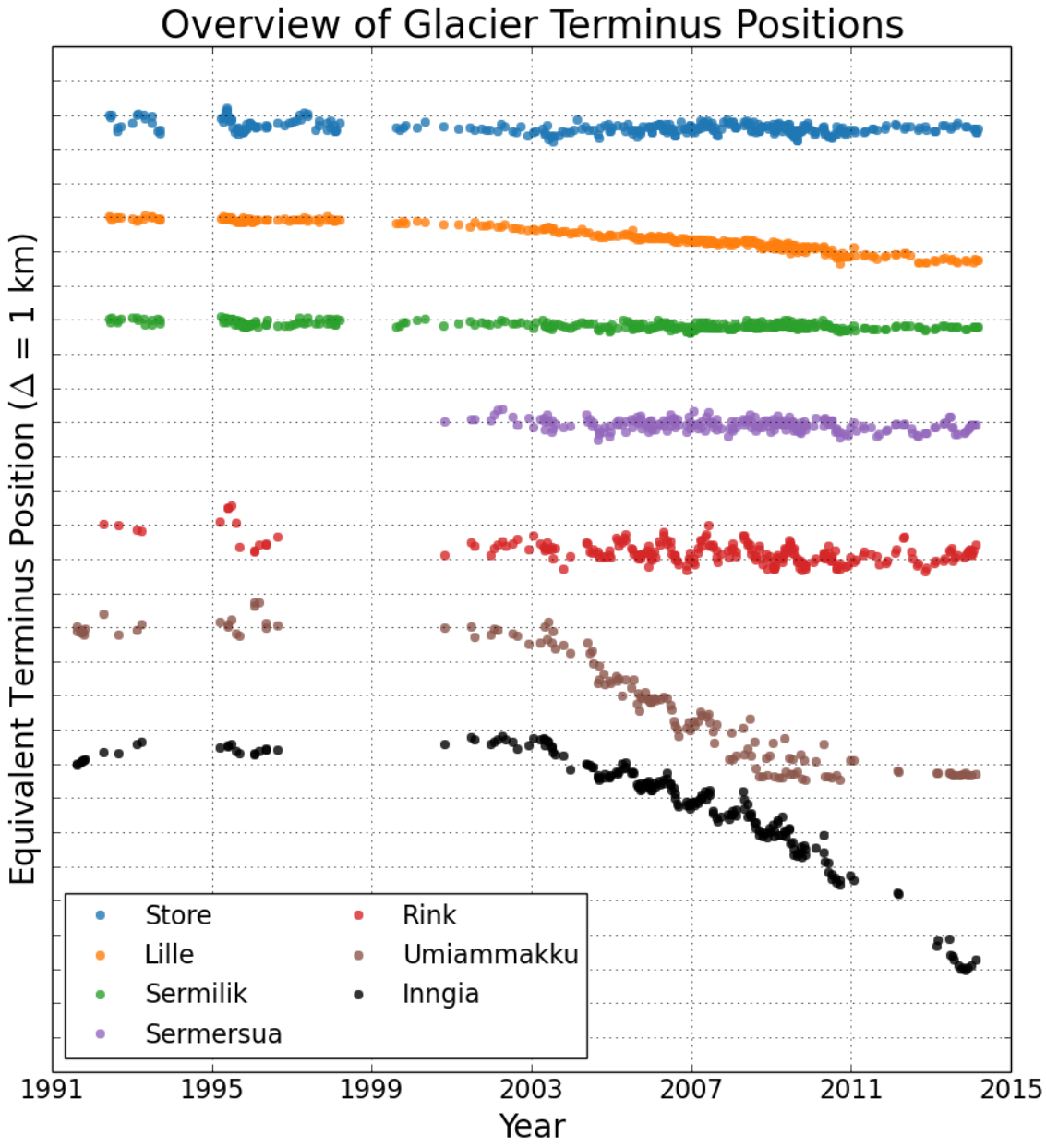

Figure 4.1: An overview of the ETP of seven glaciers in the Uummannaq Bay. From top to bottom Støre Gletscher, Lille Gletscher, Sermilik, Kangerlussuup Sermersua, Rink Isbræ, Umiammakku Isbræ and Inngia Isbræ are shown, and the vertical lines indicate a 1 km step. Error bars are not included, as they are too small to be considered on this scale (see Section 3.3.2). In Appendix A an detailed overview can be found of the observed terminus positions and their location in the fjords.

4.2. CLIMATE FORCING

In this section the climate forcing parameters are elaborated. An overview is given on timeseries SAT, SST and SIF and a trend is estimated.

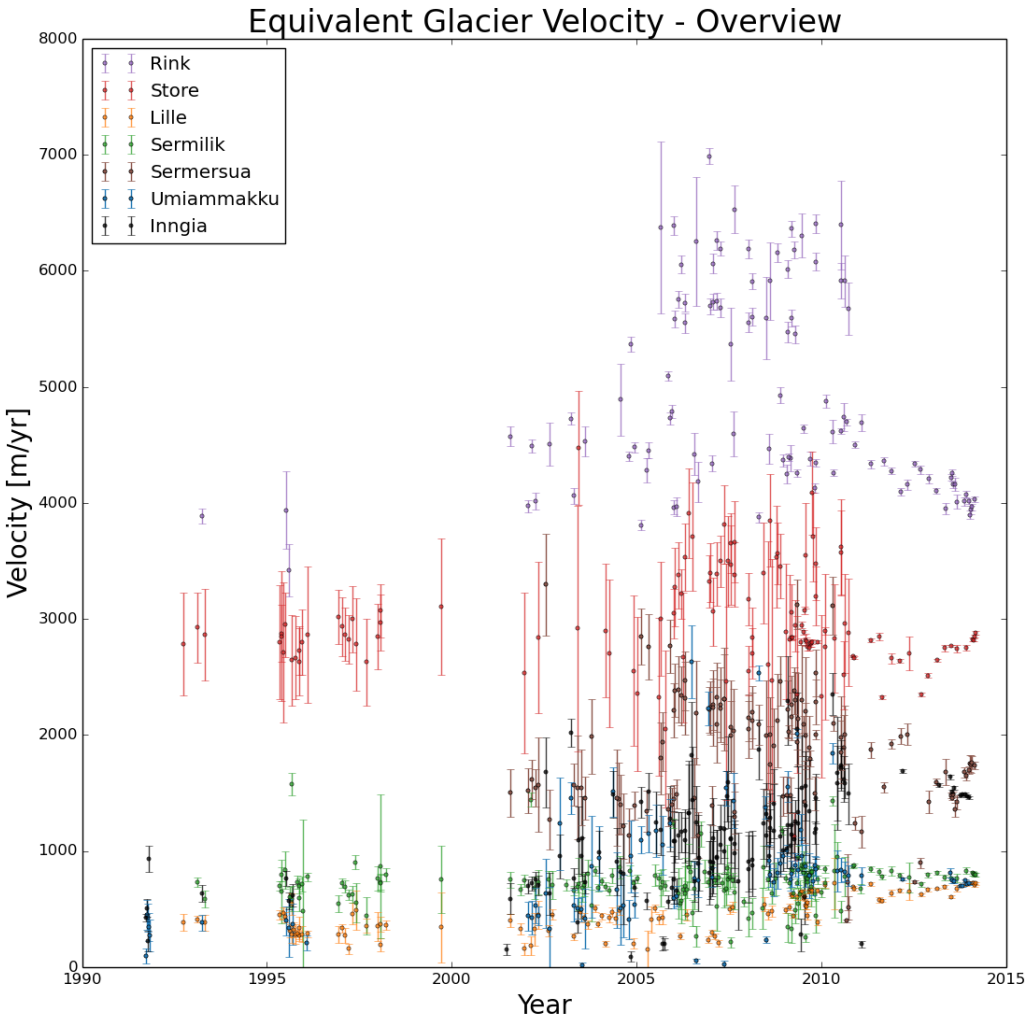

Figure 4.2: An overview of the EGV of seven glaciers in the Uummannaq Bay estimated from different satellites.

4.2.1. SURFACE AIR TEMPERATURE

The Surface Air Temperature (SAT), as obtained from the DMI datasets (see Section 2.4.2), is observed in four different locations that are not directly at the glaciers. No other temperature timeseries were available due to the remoteness of the area. Therefore, temperature data is especially interesting to consider long-term trends that are likely to be spread region-wide, such as a warm period, and not to consider daily variations or absolute values. The closest stations are Mitt. Qaarsut and Uummannaq, roughly 200 - 300 km away from the outlet glaciers, and Qullitsat (1982 to present) roughly 400 - 500 km away from the glaciers (see Table 2.4 for an overview of the stations). In Carr et al. (2013b) a similar situation was found and spatial variation was considered small.

The observed trends at Nussauq show that between 1980 and 2010 there was a 0.19° C/yr increase and that between 1990 and 2010 this trend was 0.27° C/yr (confirmed by Carr et al. (2013b). When the data for Nussauq and Mitt. Qaarsut are compared a trend of 0.10° C/yr and 0.08° C/yr is estimated, respectively. An overview of the three longer timeseries that have been observed is depicted in Figure 4.4.

In order to investigate the influence of SAT, an overview is made of seasonal temperatures in order to identify periods of relatively warm or cold weather. An overview of average seasonal temperatures at Nussauq and

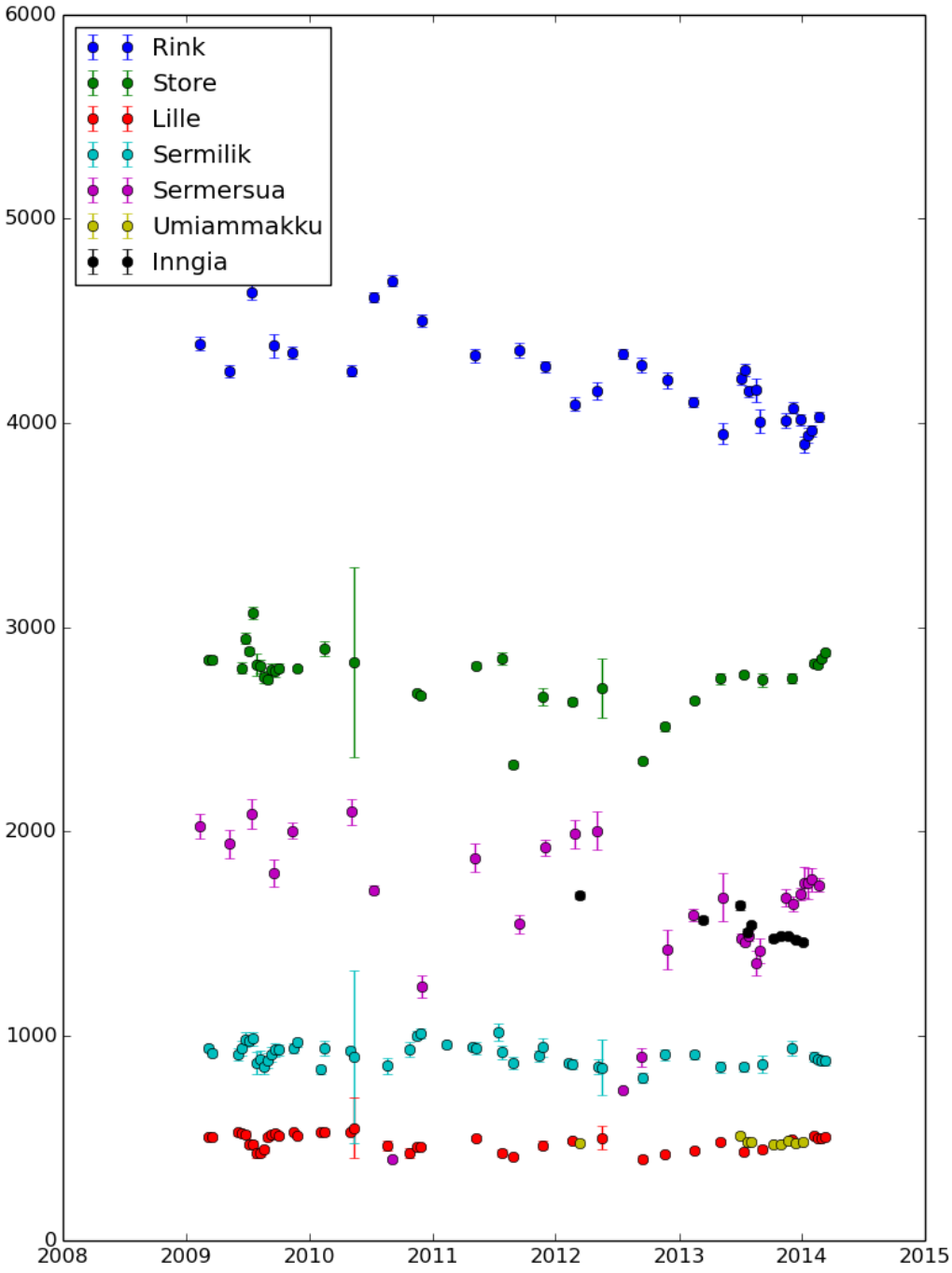

Figure 4.3: An overview of the EGV of seven glaciers in the Uummannaq Bay estimated from TerraSAR-X.

Mitt. Qaarsut is given in Figure 4.5 and 4.6, respectively. The seasonal averages are obtained from monthly

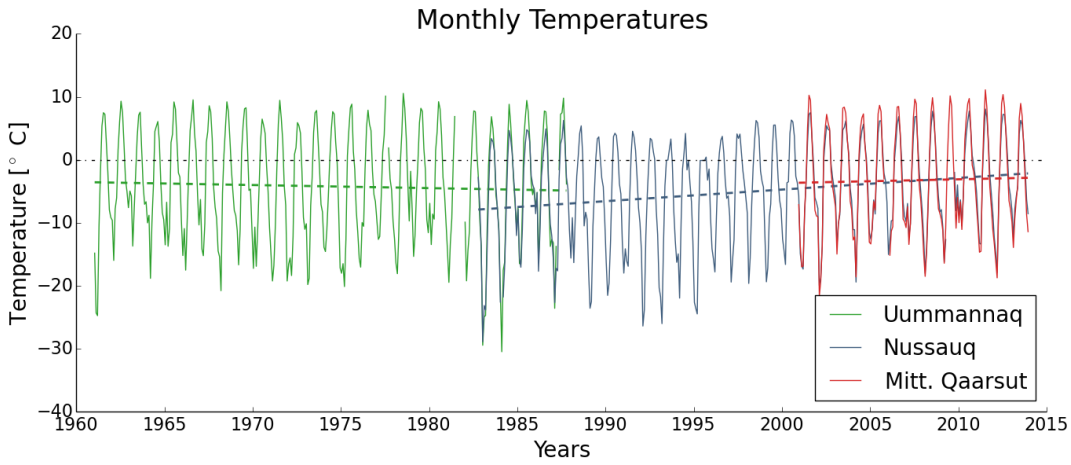

Figure 4.4: Monthly average temperatures found for three different meteo-stations. The dashed line indicates the linear trend as observed for the entire timeserie. The trend observed in Uummannaq is −0.05° C/yr, for Nussauq the observed trend is 0.19° C/yr and for Mitt. Qaarsut the trend is 0.08° C/yr. Interesting to note is that the temperatures in summer are higher for the Uummannaq and Mitt. Qaarsut stations. This is very likely to be an influence of the ocean, as Nussauq is located outside the shielded bay.

averages, that are composed of at least 22 daily averages, that in turn are made up of at least 2 observations. This is in line with the methodology Carr et al. (2013b) applied, and avoids biases due to improper sampling.

Both temperature records are in relative terms showing the same signal. The seasonal temperatures records show that there is especially a lot of year-to-year variability in winter and spring. For this research the periods between 1990 and 2012 are of special interest. The first 5 years of the 1990's are relatively cold, but from 1996 both winter and spring temperatures increase. Moreover, it can be seen that in 2003 and 2010 both the winter and spring temperatures were high, while 1998, 2000, 2005 and 2008 had a warm spring after a colder winter. 2009 and 2011 are the only years that showed a warmer winter than spring, and in 2007 the temperatures were approximately the same.

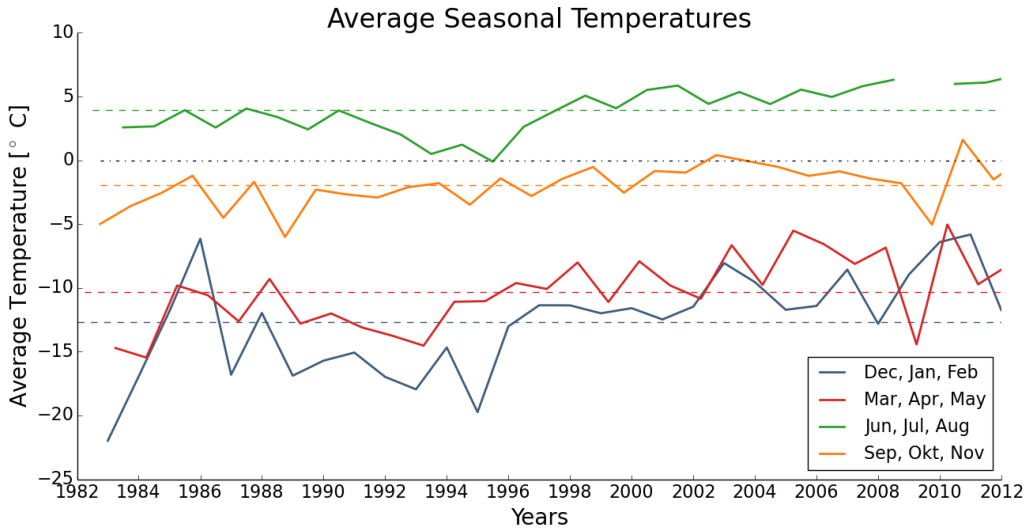

Figure 4.5: Seasonal average temperatures found for Nussauq. The dashed line indicates the average temperature of the entire timeseries per season. It can be seen that the spring temperatures and winter temperatures are quite similar, and it is often (but not always) observed that a warm winter also indicates a warm spring.

4.2.2. SEA SURFACE TEMPERATURE

The Sea Surface Temperature (SST) is, as discussed in 2.1, a mixture of ocean water and meltwater and its temperature is depending on meltwater flux, icebergs and solar radiation. As discussed in Section 2.1.2, SST

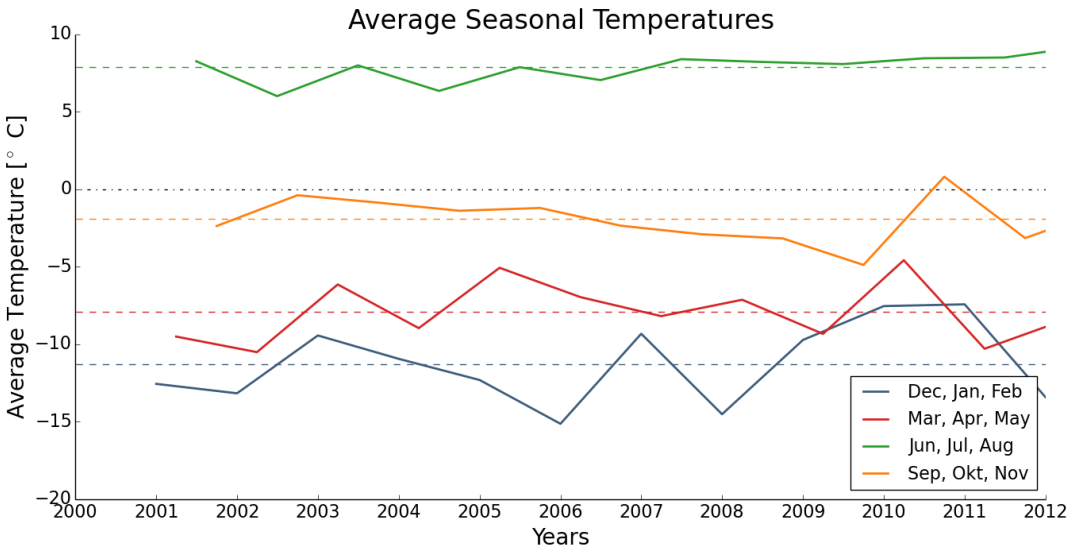

Figure 4.6: Seasonal average temperatures found for Mitt. Qaarsut. The dashed line indicates the average temperature of the entire timeseries per season. It can be seen that the spring temperatures and winter temperatures are quite similar, and it is often (but not always) observed that a warm winter also indicates a warm spring.

and DOT were identified as two different oceanic forcing parameters. DOT are related to submarine melting at the terminus grounding, whereas SST is important for processes at the top of the terminus. In this research, SST is therefore used to represent oceanic forcing. The SST data is obtained from AVHRR Pathfinder Version 5.2 Level 3 data (see Section 2.4.3) and is available for the period 1982 - 2012.

In Figure 4.7 the timeseries of the average SST is depicted. It can be seen that many SST observations are missing during winter times, and this can be caused by 1) sea ice covering the sea surface or 2) problems related to separating ice cover and SST. Remarkably, from 2003 on there are SST observations during the winter. Either there is no complete sea ice cover in the Uummannaq Bay during winter or there the observation techniques improved such that it can be distinguished from sea ice. Based on the fact that the gap in winter observations is decreasing in time, it is suggested that there is no complete sea ice cover from 2003.

It is also observed that there is a positive trend of 0.085° C/yr over 30 years of SST. In Figure 4.8 the seasonal patterns are separated, and it is observed that there is especially an increasing trend of summer temperatures. Summer and fall temperatures seem to be correlated to some extend, and show high values in 2000, 2003, 2007 and 2009. As seasonal temperatures in time are compared, the same selection of months should be compared (without gaps). Therefore, December and May are considered to represent winter and spring temperatures. Moreover, the December and May temperatures are the lowest, but are slightly increasing. 2003 and 2010 are especially warm in May and December was considerably warmer in 2004, 2009 and 2012.

4.2.3. SEA ICE FRACTION

The Sea Ice Fraction (SIF) is obtained from AVHRR Pathfinder Version 5.2 Level 3 data (see Section 2.4.3) and is available for the period 1982 - 2012. In Figure 4.9 a timeseries is given of the SIF. Howat et al. (2010) identified that the ice clearance date is regarded the most important seasonal phenomena, as it determines the duration that the ice can give 'back-stress' to the glaciers. The SIF cleareance date is defined to be the first day that the SIF percentage drops below 60%, and the SIF forming date is defined to be the first day that the SIF rises above 60 %. The results are depicted in Figure 4.10 and the clearance dates are in line with the values observed by Howat et al. (2010). The ice clearance date is estimated to be earlier with a linear trend of 1.4 day per year, the forming date comes in later with a linear trend of 2.3 day per year.

4.2.4. INTERACTION OF FORCING PARAMETERS

The climate forcing parameters are not isolated parameters but also interact together. SAT can be influenced by SST, depending on wind conditions and the topographic situation, similarly sea ice interacts with SST

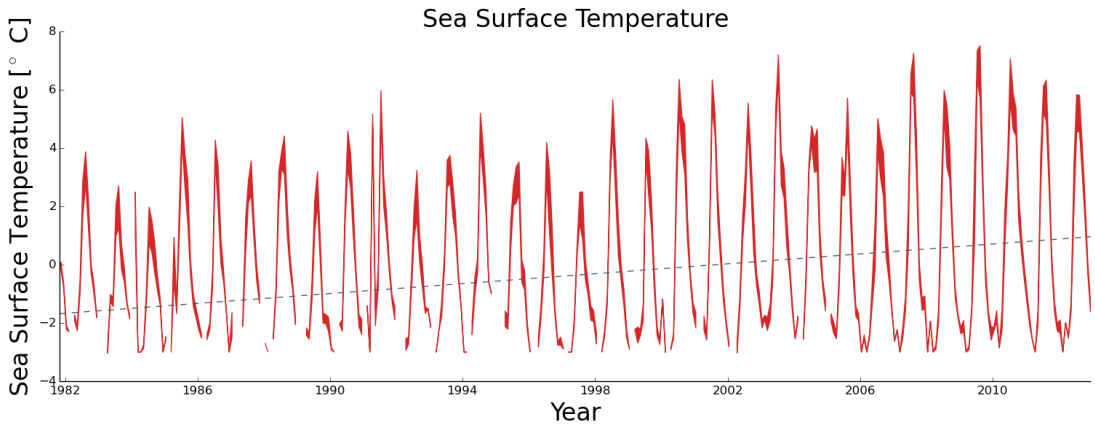

Figure 4.7: The average seasonal temperatures of the SST.

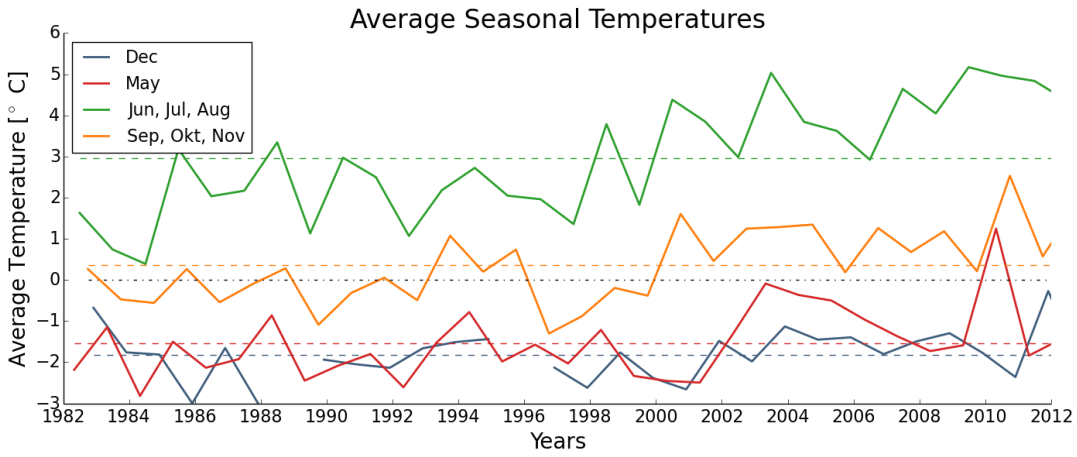

Figure 4.8: The average seasonal temperatures of the SST.

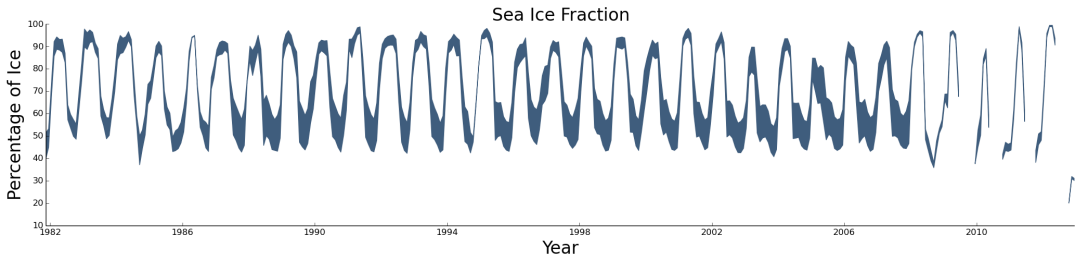

Figure 4.9: The mean SIF in the fjords between 1982 and 2012. The filled blue indicates the standard deviation.

(subsurface) and SAT (surface). However, based on the records shown before, the conclusion can be drawn that:

- SAT is increasing, but its year to year variability is high.
- SST is increasing, especially the summer temperatures.
- SIF is decreasing, especially the duration of high SIF concentrations is decreasing. Sea formation occurs later, clearance earlier.

A question remains to what extent climate forcing parameters influence each other and what triggers seasonal variations. Examining 2003 and 2010, it can be seen that the SAT was high in the winter, but the December SST was not. During the spring, both SAT and SST were significantly higher and during summer, the

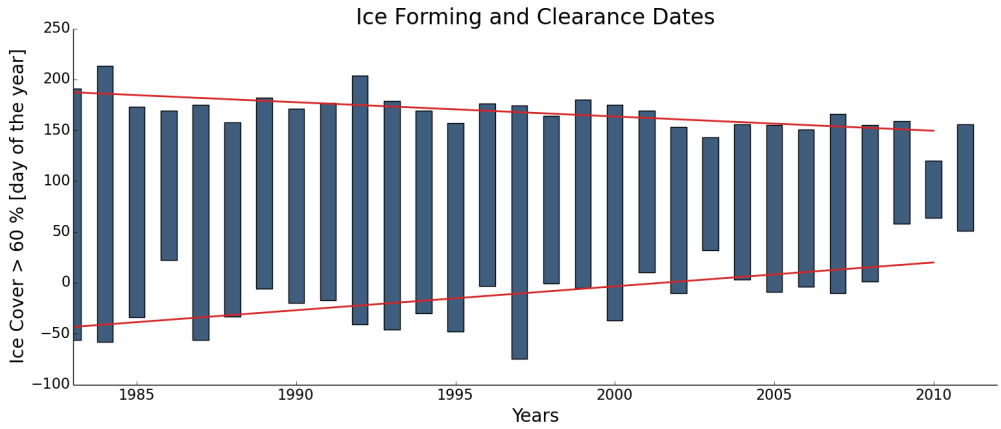

Figure 4.10: The ice clearing and forming dates given as day of the year in the fjords between 1982 and 2012. The duration of SIF levels between 60 % is getting shorter. The last three years also have data gaps (as visible in Figure 4.9 that might have influenced the results.

SST was still high while SAT was not. This might be an indication that SST follows SAT, but with a few months delay. This might also influence the SIF, as 2003 and 2010 were years in which the ice formed significantly later and cleared significantly earlier.

Other factors that are not considered in this thesis, i.e., sunshine duration, wind, albedo change, katabatic wind, might also influence the external forcing.

4.3. GLACIER-SPECIFIC FACTORS

In this section the glacier specific factors are discussed and analysed. As described in Section 2.4.4, the bedrock and bathymetry are obtained from operation IceBridge, and that the bathymetry is regarded less accurate than the bedrock. In Figure 4.11 the bedrock and ice-thickness are visualized, and they show that the central interior of Greenland is actually below sea level.

The bedrock structure of the Uummannaq-region, a detailed subsection can be found in Figure 4.12, is different in the North and the South. The Northern glaciers (Inngia Isbræ, Umiammakku Isbræ) originate from a higher bedrock plateau, in contrast it is observed that in the Southern part the glaciers (Støre Gletscher, Lille Gletscher and Sermilik) originate from a lower bedrock. This might explain why the Southern glaciers are generally shorter and wider compared to the Northern glaciers. The thickness of the ice at the base of the glaciers also differs between the glaciers in the North and in the South. Støre Gletscher, Lille Gletscher and Sermilik are relatively close to the 1500 m line of the ice thickness, while Kangerlussuup Sermersua, Rink Isbræ and especially Umiammakku Isbræ and Inngia Isbræ are further away.

In Table 4.1 the fjord geometry of the different glaciers is set out. It can be seen that Støre Gletscher and Rink Isbræ have a deep terminus base, and that there are three glaciers with a shallow terminus base (Lille Gletscher, Sermilik and Inngia Isbræ). Støre Gletscher and Rink Isbræ have both wide fjords and a deep terminus position. Moreover, Støre Gletscher and Rink Isbræ are positioned in a shallow location in the fjord and seem to have a deeper basin behind it. Retreat from its original position means that the glaciers move to a wider and deeper position in the fjord. Similarly, Umiammakku Isbræ has a ETP that is positioned in a narrow fjord with a shallow terminus base, but a retreat would mean that the terminus enters a deeper and wider location.

Sermilik is an special glacier compared to the others, as it has a shallow and narrow terminus position and is relatively thick. The slope at its front is steep, it seems that the terminus is very close to a bedrock formation above sea level. Another interesting geometry is found at Kangerlussuup Sermersua, that has a quite long, non-straight, terminus line. Interestingly, its terminus base is at a shallow location with a deep bedrock basin behind it. Its distinctive shape is likely to be maintained due to this shallow location, and a question remains if this position is formed by basal sediment transport meaning that a glacier 'digs' its terminus base.

Lille Gletscher and Inngia Isbræ are located in a relatively narrow and shallow fjord, although Lille Gletscher

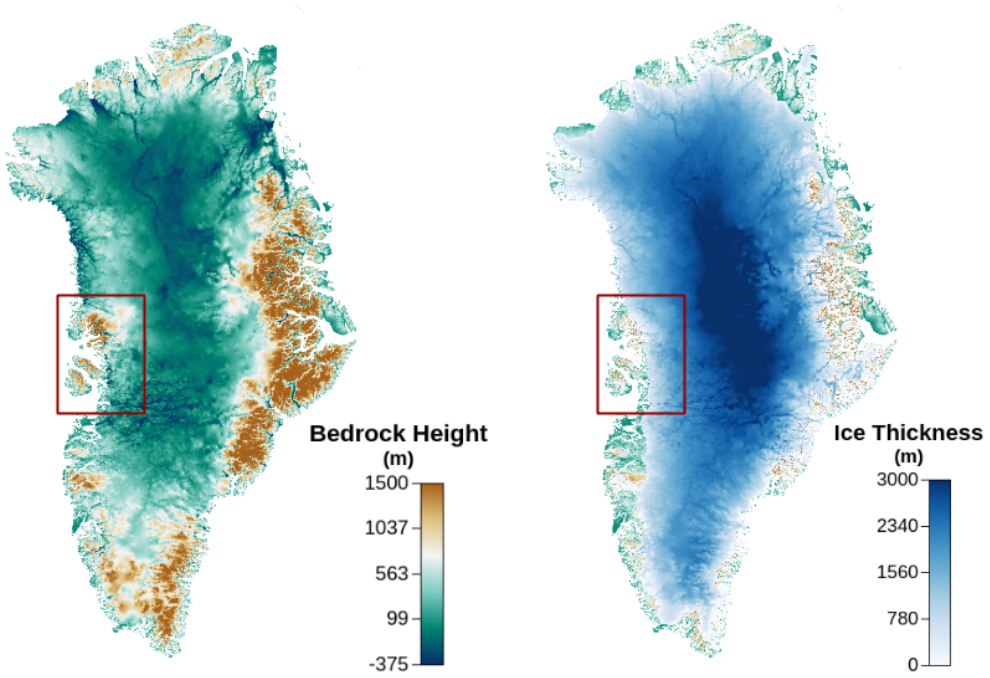

Figure 4.11: An overview of the bedrock and ice thickness of the Greenland Ice Sheet. The left image is the bedrock height and left is the ice thickness.

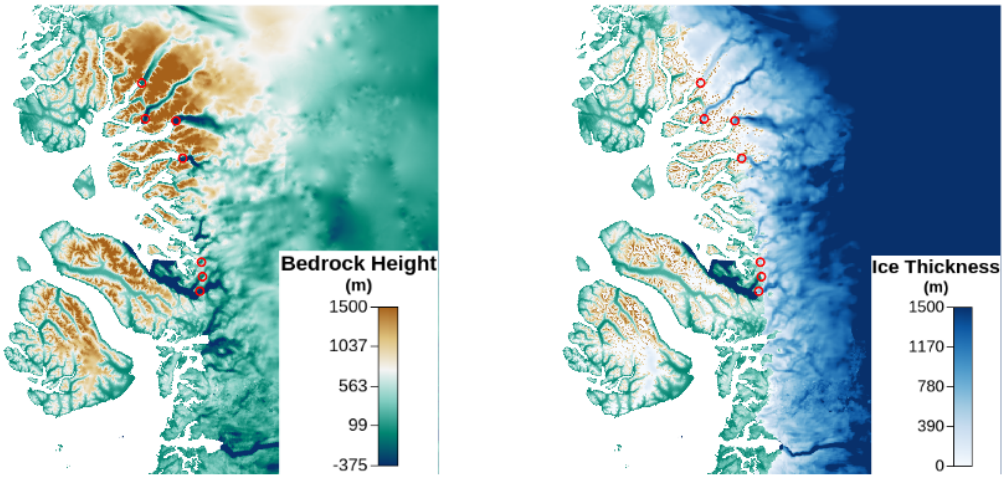

Figure 4.12: An overview of the bedrock and ice thickness of the Uummannaq Bay. The left image is the bedrock height and left is the ice thickness.

is much closer to the ice sheet than Inngia Isbræ. In front of the Lille fjord, a high, flat plateau is found with a wide fjord geometry. It is observed, that glacier is located in slightly deeper water but at a narrow fjord location and the bedrock shows an increasing profile. At Inngia Isbræ a similar situation is found, although bedrock and bathymetry are showing a different depth. Looking at both bathymetry and bedrock profiles, the profiles agree that the terminus position has retreated into a slightly deeper and wider fjord geometry, but after 15 km (of its original position) the bedrock increases significantly.

Table 4.1: An overview of the fjord geometry for the different glaciers. The terminus depth is based on both bedrock and bathymetry (if available), bedrock slope is based on the bedrock profile just behind the terminus position.

Glacier	Fjord Width	Fjord Depth	Ice Thickness	Bedrock Slope
Støre Gletscher	5 km	400 - 500 m	500 - 1000 m	Downward
Lille Gletscher	2 - 3 km	0 - 100 m	100 - 200 m	Downward
Sermilik	2.5 km	100 m	200 - 500 m	Upward
Kangerlussuup Sermersua	5 km	200 - 300 m	200 - 500 m	Downward
Rink Isbræ	5 km	600 - 700 m	600 - 1000 m	Downward
Umiammakku Isbræ	3 - 5 km	200 - 400 m	200 - 700 m	Downward
Inngia Isbræ	3 - 4 km	100 - 300 m	100 - 300 m	Downward

4.4. SYNTHESIS

Here results that are estimated from SAR observtions, as presented in Section 4.1, are put in perspective with climate data from Section 4.2 and glaciers-specific factors from Section 4.3. The results are elaborated based on the glaciological aspects of marine-terminating outlet glaciers as discussed in Section 2.1.

In the SAR-based ETP results it is observed that Umiammakku Isbræ and Inngia Isbræ have shown rapid retreat, Lille Gletscher showed a slow retreat and that the other four glaciers (Støre Gletscher, Sermilik, Kangerlussuup Sermersua and Rink Isbræ) glaciers are relatively stable. Based on Equation 2.2 it can be stated that first 2 glaciers have a sufficient negative MB to initiate a rapid retreat. They both started to retreat in 2003, after a winter in which the duration of high SIF concentrations were shorter than normal and both SST and SAT were higher than normal. Consequently, the glacier experienced less buttressing from the sea ice melange, leading to increased calving. The increased calving caused a negative MB that was sufficient to initiated multi-year retreat.

As discussed in Section 2.1.2, retreat of marine-terminating glaciers can initiate a positive feedback loop in case it retreats into deeper waters. This is observed at Inngia Isbræ, which retreated into a (slightly) deeper and wider fjord. It is also observed that its EGV increased during this period, which could be a consequence of a lower resistive force at the bed and fjord-walls (see Equation 2.3). The resistive forces decrease as a consequence of the terminus retreat, as there is less contact with the bedrock. Additionally, the resistive force of the terminus moraine shoal also decrease with retreat, thereby allowing a positive feedback loop (Fischer and Powell, 1998). The ETP retreat of Inngia Isbræ accelerated after 2008 and did not stop until the end of the timeseries. The combination of a retreat into a deeper fjord and an acceleration of its velocity, is suggested to be an indication that its grounding line is retreating under influence of a positive feedback loop of an increased calving rate C.

Umiammakku Isbræ shows a different evolution. Its initial retreat was quicker than that of Inngia Isbræ, but it ceased in 2009 and it also did not show an increase of its EGV during its 6 year retreat. It also did not retreat along a reverse bedrock, and retreated to a shallow position in the fjord that was actually at a wider position than it's original position. There might be two possible explanations: 1) Umiammakku Isbræ had a floating tongue that collapsed, but it's grounding line did not retreat, or 2) it retreated to a former terminal moraine shoal that was still present and that was shallow enough to restore the MB.

The relative slow retreat of Lille Gletscher is suggested to start in 2001, although there are not enough observations between 1998 and 2000 to rule out that its retreat started earlier. It's retreat is relatively slow compared to Inngia Isbræ and Umiammakku Isbræ and a very subtle acceleration is observed (+100 m/yr in 10 years). The bedrock at Lille Gletscher is shallow compared to other glaciers, and it's calving rate C is therefore likely to be small (see Equation 2.5). Although it did retreat into a narrower part of the fjord, it was not sufficient to stop its retreat. Its initiation does not seem related to a climatic event as for Inngia Isbræ and Umiammakku Isbræ, although its retreat did speed-up after 2003. Another aspect is that Lille Gletscher is originating from a higher bedrock point, and its connection to the ice sheet is relatively weak. As its EGV increases it seems logical that the driving stress in Equation 2.3 is constant and that the friction at the bedrock or the fjord walls is reduced.

The other four glaciers are relatively stable, and do not show long-term terminus advance. This means that the MB, according to Equation 2.2, should be approximate equilibrium. Any surplus of the MB would mean that the glaciers were able show a slow advance, but they do not show this behaviour. As advance is not observed, it can be concluded that none of the glaciers has a positive MB. However, retreat is also not observed. Here it is suggested that there is a retreat threshold MB_T, based on the MB. If the MB is lower than

the this threshold ($B_s + C + B_o < MB_T$), rapid retreat is initiated. As long-term forcing will weaken a glacier by undercutting its terminus, or by an increased ablation area, it is likely that long-term forcing lower the retreat threshold. However, this retreat threshold is hard to quantify, and modelling performed by Morlighem et al. (2016) showed that a surprising high calving flux should occur to initiate a rapid retreat of Støre Gletscher. It is therefore likely that further climatic warming and potentially warm seasons can initiate a negative MB that is low enough to initiate retreat, meaning that a rapid long-term retreat is initiated. Except for Sermilik, all glaciers have a reverse bed that allows such a rapid retreat.

The seasonal evolution of ETP is correlated with the presence of sea ice melange. To analyse this relation, the terminus behaviour with and without sea ice melange is considered in Figures A.3, A.6, A.9, A.12, A.15, A.18 and A.21. Here linear trends are estimated during high SIF concentrations and during low SIF concentrations. The linear trends are estimated per frame, in order to avoid bias related issues as discussed in Section 2.3.4. The average linear trend is visualized in the figures, and they show an interesting pattern. Some glaciers have a clear advance and retreat cycle depending on SIF concentrations. Rink Isbræ, depicted in Figure A.15, shows a clear seasonal pattern in its ETP motion, ranging up to a kilometer. On the contrary, Støre Gletscher, is less sensitive to the presence of sea ice and shows only a minor seasonal signal (see Figure A.3).

However, the terminus evolution during ice-free periods is not a purely linear. The motion of the ETP is characterized by 1) a period of rapid retreat after ice break-up, 2) a period of stabilization in mid-summer and 3) a period of advance during periods with sea ice melange. A terminus collapse has been observed often, for example in the spring of 2006 and 2007 the terminus retreated about 600 m at Rink Isbræ (see Figure A.15). This pattern is also observed Støre Gletscher (for example the clearance in 2009). The quick collapse occurs generally within a month after ice break-up. It is suggested that Rink Isbræ builds up a seasonal floating tongue, that collapses after clearance of the sea ice Rignot et al. (2015). In this study we can not distinguish floating tongues, but the advance rates at Rink Isbræ are too high to be correlated with grounding line advance, as this is expected to be in the order of 30 m/yr Nick (2006).

The retreating glaciers also show this behaviour. At Inngia Isbræ, see Figure A.21, this effect is also observed to be of big influence. As the advance is less than the retreat, Inngia Isbræ shows a multi-year retreat. A similar pattern is found at Umiammakku Isbræ (see Figure A.18), indicating that Inngia Isbræ and Umiammakku Isbræ are both sensitive to the sea ice melange. The short duration of high SIF concentration in the 2003 winter and the quick retreat in 2003 summer mark the start of the long-term retreat of their termini. During their long-term retreat they still showed periods of slow advance, countered by rapid retreat during summer. Umiammakku Isbræ clearly ceased to retreat after the summer of 2008, mainly due to a smaller retreat in summer. At Inngia Isbræ the reverse can be observed, after a very quick retreat in the summer of 2003 its retreat slowed down and it even advanced during winter periods. However, after the winter of 2008 it did not show advance and its retreat accelerated. Seasonal ETP variations are smaller at Lille Gletscher, but they are suggested to influence its retreat (see Figure A.21). In the summer of 2003 it showed a significantly higher retreat than in other years, but its ETP position does not always advance in winter.

When comparing the glacier-specific factors of the retreating glaciers with the stable glaciers, the conclusion can be drawn that all the retreating glaciers are in a shallow fjord. Observations show that two of the retreating glaciers started their retreat after a warm winter with a short duration of high SIF concentrations. It is suggested that, for this region, glaciers with a shallow terminus are more vulnerable to variations in SIF than glaciers with a terminus is deep waters. This seems to be contrasting with Equation 2.5, which predicts that a deep terminus has a higher calving flux. The sensitivity of the calving sensitivity c to seasonal variations in SIF might be larger for glaciers with a shallow terminus, and/or for glaciers with a deep terminus the relative importance of the calving rate C might be lower when considering a large OMB as suggested in Equation 2.6.

4.4.1. DISCUSSION

Here we put the results into perspective with earlier research that has been conducted in the Uummannaq-region (see Section 2.1.3). The retreat of Umiammakku Isbræ and Inngia Isbræ has also been observed by Howat et al. (2010). He also identifies that the winter of 2003 might have initiated this retreat. The results presented in study underline this hypothesis, also by showing that the glaciers were showing a stable ETP during the 1990's. Howat et al. (2010) also reported on a speed-up of Inngia Isbræ and Umiammakku Isbræ. The speed-up of Inngia Isbræ is confirmed by this study, but the speed-up of Umiammakku Isbræ is not observed. This could be related to the velocity box, which is located relatively far upstream to avoid layover effects. This also awakes the discussion whether the speed-up observed by Howat et al. (2010) is only close to

the terminus, and that the flow velocity upstream remained relatively stable.

Carr et al. (2013b) has observed a stepwise retreat of Alison Glacier, where the glacier retreated from narrow section to narrow section. In this study, this behaviour was not observed. On the contrary, it was observed that glaciers retreated did not stop their retreat at a narrow section of the fjord. However, we do observe that Umiammakku Isbræ ceased its retreat at a shallow point. This brings up the discussion what is considered to be of larger influence: fjord width or fjord depth? Or is this different for each glacier? More research will be needed to assess the actual role of glacier-specific factors.

Recent studies by Rignot et al. (2015) and Rignot et al. (2016) have been focussed on the role of submarine-melting. The patterns we see in our study show that glaciers with a terminus in a deep fjord, such as Rink Isbræ and Støre Gletscher, are stable. Moreover, the glaciers in a shallow fjord have observed to show retreat. Given that it is justified to assume that the glaciers in a shallow fjord are unaffected by submarine melt, our results show that there is no relation between submarine-melting and retreat.

4.4.2. QUALITY OF RESULTS

Here the results of the SAR observations are evaluated, and it is elaborated what improvements could still be made. In Section 3.3 it is described how the ETP and EGV are estimated from SAR images, and the results are shown in Section 4.1. They show that the ETP is determined with an accuracy of 15 to 50 m, accurately enough to capture seasonal signals and significant trends. A bigger source of uncertainty for digitization, especially for descending ERS images, is the effect of layover due to a unsuitable orbital mode, which is a mayor disturbing factor for the Northern Glaciers (Inngia Isbræ, Umiammakku Isbræ).

Velocity estimations on glaciers were found to be difficult for ERS and Envisat images, as their 35-day baseline introduces a large decorrelation. Using a model-based filter, outliers were removed and this improved the results. It was found that for each frame many outliers were concentrated on the glaciers, and this sometimes lead to empty patches. Therefore, an appropriate spot for the velocity-box to estimate the EGV had to be found, meaning that is was not possible to use the same point for each glacier.

It is also observed that EGV estimates of ascending Envisat frames are sometimes overestimating it. This is only observed at two glaciers, Rink Isbræ and Støre Gletscher (see Figures A.2 and A.14). For the other glaciers the EGV of ascending Envisat frames is matching the EGV estimated in other frames, and also descending Envisat frames are found to match other frames even at Rink Isbræ and Støre Gletscher. Next to this, ascending TerraSAR-X estimates are matching the other frames, ruling out that this problem is caused by the orbit mode only. It is not clear why this bias comes from, but it is suggested that it has to do with a unfavourable incidence angle at which displacements are estimated. As it only occurs for Rink Isbræ and Støre Gletscher, the relation between large displacements and false EGV estimates seems to be present as well. It could be that the approach described in 3.3.3, using a parallel slope and a DEM to decompose a 2D displacement vector into a 3D component, causes this bias in EGV. The estimated slope S_{az} and S_{sr} can be unfavourable in the particular case of the Envisat ascending frames, meaning that $\sin(\theta) - S_r \cos(\theta) \approx 0$. Another source of the bias could be related to the DORIS geocoding, but this is not expected as the geocoding works well in all the other frames.

When 35-day velocity estimates of ERS and Envisat were compared to TerraSAR-X estimates, it was found that TerraSAR-X estimates were less decorrelated. So with relatively the same baseline, ICC offset tracking with TerraSAR-X gave better results. This can either be due the difference in operating band, or to the difference in resolution. In order to investigate if this problem is related to the different operation bands, the amplitudinal variations on Støre Gletscher were estimated in a 10 km^2 box (see Figure 4.13). A very clear seasonal signal is seen, that is related to the processes described in 2.3.2, and it can be seen that TerraSAR-X shows slightly less seasonal variations. Although the role of resolution is unclear, it can be stated that decorrelation might be less due a lower sensitivity to changes in backscatter properties of snow and ice.

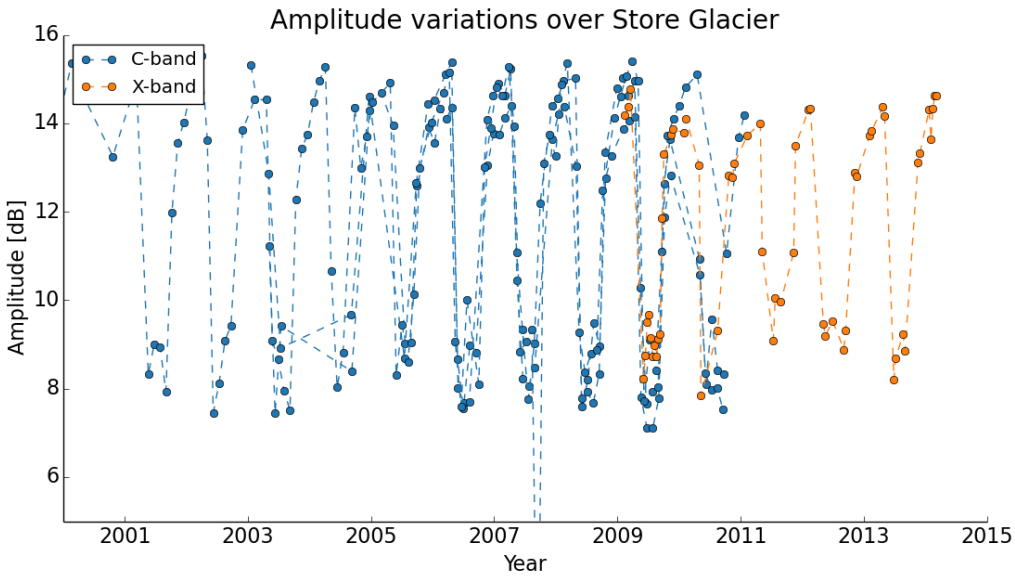

Figure 4.13: Variations of the amplitude as observed on Støre Gletscher.

5

Conclusions and Recommendations

In this thesis the link between climate forcing and glacier behaviour is studied using SAR-based observations. These observations are needed to understand how outlet glaciers react to climate forcing. Especially the calving dynamics of marine-terminating glaciers is poorly understood. It is suggested that each glacier has a different sensitivity to climate forcing due to specific factors, such as fjord width and bedrock topography, and that long-term retreat may be initiated by seasonal variations in climatic parameters, such as Surface Air Temperature (SAT), Sea Surface Temperature (SST) and Sea Ice Fraction (SIF). Seven marine-terminating outlet glaciers in the Uummannaq-bay were studied, because of its shielded topography meaning that the climatic conditions within the bay are assumed to be comparable.

How to observe and interpret glacier behaviour using synthetic aperture radar?

A dataset of 665 SAR images (ERS, Envisat and TerraSAR-X), spanning from 1991 to 2014, was processed and analysed. With this dataset two parameters were estimated: Equivalent Terminus Position (ETP) using manual digitization and Equivalent Glacier Velocity (EGV) using amplitude offset tracking (ICC). It is difficult to coregistrate SAR-images in areas covered by water and ice. Therefore, coregistration windows were created on stationary areas, i.e., mountains, using land-classification data. Using a 'best slave', an emperical selection was made of windows that did not show decorrelation. In this way, coregistration was possible for most images while maintaining processing speed.

It was shown that the terminus projection on the Earth is dependent on the DEM location of the terminus, the reflection location, the orbital mode and incidence angle at which a SAR-image is acquired. This can lead to a bias when digitizing the terminus location, and in order to have a consistent bias it was chosen to modify the DEM location of the terminus to always overestimate the terminus. It was also chosen to use a Flowline Reference System (FRS), which follows the flowline of a glacier. The advantage of a FRS is that a glacier is considered to be straight, allowing a proper projection of the ETP and to reference estimated offsets into a along-track and across-track direction. It was shown that the estimated ETP using the FRS is a better representation than the box-method. The difference between the two methods can be up to a factor two.

The estimated offsets were estimated for each consequential SAR-image pair and converted velocities. The EGV was estimated using a velocity-box, located at a fixed distance from the ETP, in which the mean velocity was estimated and considered representative for the velocity of the glaciers. ERS and Envisat datasets were showed high decorrelation leading to noisy and relatively inaccurate estimations. The estimated offsets of ERS and Envisat were therefore filtered using a model based outlier removal (w-test). The model was based on the along-track velocities and calibrated with 11-day TerraSAR-X results, that showed practically no noise. The filter improved the results, but the estimated velocities were not accurate enough to perform a seasonal analysis on the ERS and Envisat EGV results. The TerraSAR-X results, both EGV and ETP, are comparable with the results obtained by Moon et al. (2014) for 2009 - 2013.

What seasonal and long-term evolution can be observed at the glaciers in the Uummannaq-region?

The observed ETP results show that three glaciers (Lille Gletscher, Umiammakku Isbræ and Inngia Isbræ) showed long-term retreat, of which two (Umiammakku Isbræ and Inngia Isbræ) showed rapid retreat, and that 4 glaciers are stable and that no glacier advanced. All glaciers showed a stable ETP and a stable EGV during the 1990's. Retreat was initiated in 2001 for Lille Gletscher and 2003 for Umiammakku and Inngia Isbræ. Lille Gletscher and Inngia Isbræ retreated 1.3 km and 6 km respectively and the retreat was observed until the end of the timeseries. Umiammakku ceased its 4 km retreat in 2009, and its ETP remained stable for the years after. The retreat of Inngia Isbræ is accompanied by an increase of the EGV, that became three times higher (from 500 m/yr to 1500 m/yr) in 2010 compared to its EGV in the 1990's. Umiammakku also showed a long-term increase of EGV, but a less dramatic change was observed compared to Inngia Isbræ (400 m/yr before retreat to 700 m/yr after retreat). Lille Gletscher only showed a small increase in EGV after its retreat (400 m/yr before retreat to 600 m/yr in 2010). All other glacier did not show long-term accelerations or decelerations.

Regarding intra-annual variations, ETP results showed that some glaciers show strong seasonal terminus variations (advance during winter, retreat during summer) and that the amplitude of these variations are different from glacier to glacier. All glaciers show a sudden retreat in early spring, but the magnitude of this retreat differs from glacier to glacier and from year to year. Rink Isbræ shows the largest retreat after the SIF concentrations drop, up to 1 km retreat is observed in the timespan of a month. The EGV results show that many glaciers have temporal variations in their velocity, but ERS and Envisat results were not accurate and abundant enough to classify these variations as seasonal.

How does climate forcing influence the behaviour of glaciers in the Uummannaq-region?

Surface Air Temperature (SAT) and Sea Surface Temperature (SST) timeseries in the Uummannaq Bay show a increasing trend since the 1980's. Synchronously, the Sea Ice Fraction (SIF) shows a decreasing trend. In order to distinguish periods of vast ice melange in the fjords, a forming and clearing date of sea ice melange is estimated using SIF. The forming date of the sea ice melange is observed to be 2.5 day later each year, while the clearing date is observed to be 1.5 day earlier each year. It was found that there is a link between large SIF concentrations and retreat/advance of the ETP. Periods in which SIF concentrations are high, all glaciers generally show advance, even the ones that show a long-term retreat. The magnitude of this relation is different for each glacier, Rink Isbræ shows variations up to a kilometer whereas Støre Gletscher only shows variations of about 200 m.

The high SAT and SST in 2002/2003 are likely to have caused a late forming date and an early clearance date of the sea ice melange. It is also observed that in the warm summer of 2003, long-term retreat of the ETP was initiated for Umiammakku and Inngia Isbræ. The years after 2003 were less warm, but the retreat did not stop. It is therefore concluded that the exceptional climate forcing in 2002/2003 initiated the long-term retreat of Inngia Isbræ and Umiammakku Isbræ after a decade of stability. Howat et al. (2010) had a similar conclusion, but did not consider the evolution during the 1990's.

How do glacier-specific factors influence the behaviour of different glaciers in the Uummannaq-region?

Glacier specific factors are suggested to be decisive in a glaciers response to climate forcing. Using bedrock and bathymetry data, it is shown that there are big differences in the depth of the fjords. Rink Isbræ and Støre Gletscher are located in deep fjords (500 - 800 m deep), whereas Lille Gletscher and Inngia Isbræ are located in shallow fjords (> 200 m deep). It was also found that most glaciers formed a terminal moraine shoal, as described by Powell (1990), meaning that the terminus is located on a relatively shallow location. This also implies that all glaciers, with exception of Sermilik, have a reversed bedrock slope.

The response to exceptional climate forcing is suggested to be influenced to the fjord-depth. Glaciers in relatively shallow fjords have found to be retreating, and in two of the three cases this was a result of the exceptional climatic conditions in 2002/2003. Glaciers in deeper waters did not show a change in ETP. At Inngia Isbræ it was observed that its terminus retreated into deeper waters, that eventually lead to a positive feedback loop where a retreat in deeper waters increased the calving rate C and caused a speed-up of the glaciers due to a lower basal drag. This was not observed at Umiammakku, where it is suggested that the retreat of

its ETP is related to a break-up of a floating tongue. As the study only focussed on seven glaciers, it can only be suggested that there is a relation between the depth of a fjord and its sensitivity to climate change, more observations are needed to confirm this hypothesis.

How do different marine-terminating outlet glaciers respond to a similar climate forcing?

In conclusion, it was observed that seasonal climatic forcing can initiate rapid retreat of marine-terminating outlet glaciers, if the grounding line retreats into deeper waters. It was also observed that glaciers in a shallow fjord are more sensitive to seasonal variations of the SIF, whereas glaciers in a deeper fjord were observed to be more stable. It is suggested that they are more sensitive because the calving flux is relatively more important than submarine melt, as is the case for glaciers with a deeper grounding line. Both observations confirm that seasonal variations can initiate long-term retreat, and that the sensitivity of a glacier to climate forcing is controlled by glacier specific factors, especially its terminus depth.

5.1. RECOMMENDATIONS AND FUTURE WORK

Although the intention of a scientific study is to find answers to questions, they also generate new questions. During the study, new questions arose and unsolved problems were encountered. In this section an overview is given on where new studies should be focussed on and how the methods used in this study can be improved.

The scientific research to marine-terminating outlet glaciers on Greenland has mainly been focussed on the large glaciers. This study has shown that other, smaller glaciers can provide valuable insight into the relationship between external forcing and glacier evolution. Subsurface processes are suggested to be important for glaciers with a deep grounded terminus, but the size of these processes is not quantified. It is therefore suggested that:

- more regions are studied. Especially the evolution of different glaciers with comparable climatic conditions should be elaborated. When a sufficient number of glaciers is studied, it can be verified if the hypothesis on an increases sensitivity to climatic forcing of shallow glaciers holds.
- long-term submarine observations are made to quantify the amount of submarine melting. Especially quantification of the submarine meltprocesses are important to understand the influence of submarine melting to the MB.
- the retreat threshold, as introduced in Chapter 4, should be defined and be quantified. This allows to identify which glaciers at which a retreat is imminent and predict future response to climate change.

SAR images have been shown to be very suitable for glaciological observations. The value of old ERS and Envisat images is that they are made up to decades ago, and although processing is difficult and results can be noisy, their added contribution is high because they place glacier stability into a long-term perspective. In order to obtain velocity estimations on marine-terminating outlet glaciers, ICC offset tracking was considered to be the best technique to do so when using ERS and Envisat images. With Sentinel-1 providing us new SAR-images in the near future, the decision of using ICC offset tracking should be reconsidered as these images do have a stable phase. It was also observed that TerraSAR-X was less subject to decorrelation, but it remains a question whether this is related to resolution or to operating band. Furthermore, the EGV is a summary of an arbitrary point on a glacier and the comparability between different glaciers is questionable. Although relative variations can be compared between glaciers, absolute variations can not be compared. It is recommended that:

- the use of spectral diversity is explored for Sentinel-1. As the resolution of Sentinel-1 Interferometric Wideswath (IW) is comparable with ERS and Envisat, ICC offset tracking will be limited by the resolution. Spectral Diversity is considered more accurate and is still able to estimate higher velocities compared to interferometry (see Section 2.3.1).
- a proper Equivalent Glacier Velocity (or flux) is defined, as discussed in 3.3.6. The current EGV is based on an average velocity at an arbitrary point. Comparing glaciers is therefore difficult, as the velocity profile of each glaciers different. Some glaciers show a linear acceleration towards the terminus,

some show an exponential acceleration. These velocity profiles should be taken into account when two glaciers are compared.

- the difference between offset tracking with C-band and X-band (and maybe also L-band) is researched. In this study it is suggested that X-band images show less decorrelation than C-band, but it remains unclear how resolution influences decorrelation.

5.2. CONTRIBUTION

The contribution of this study to the scientific community should be placed in the context of the state-of-the-art research within the field of outlet glaciers, and their propositions for further studies. This study extended the current records by using ERS data from the 1990's. Glaciers are observed to be stable during this period, thereby showing that the 2003-retreat should be considered unique. Another contribution of this study is that the glacier evolution was not only considered with respect to climatic forcing, but also with respect to glacier-specific factors.

Furthermore, during the study came up with some improved methodology. A Flowline Reference System (FRS) is introduced. By referencing the terminus position to the FRS, the equivalent terminus position was significantly improved with respect to the box-method (up to a factor two). The FRS also allowed to obtain a along-track velocity profile, that was be used to filter outliers from noisy datasets.

BIBLIOGRAPHY

Synthetic Aperture Radar Missions. 2014. URL http://www.esa.int/Our_Activities/Observing_the_Earth/Copernicus/SAR_missions.

L. J. Bamber, B. R. Alley, and I. Joughin. Rapid response of modern day ice sheets to external forcing. *Earth and Planetary Science Letters*, 257:1–13, 2007. ISSN 0012-821X. URL http://www.sciencedirect.com/science/article/pii/S0012821X07001628.

R. Bamler and P. Hartl. Synthetic aperture radar interferometry. *Inverse problems*, 14, 1998. ISSN 0266-5611. URL http://iopscience.iop.org/article/10.1088/0266-5611/14/4/001/meta.

P. Beckmann and A. Spizzichino. The scattering of electromagnetic waves from rough surfaces. *Norwood, MA, Artech House, Inc., 1987, 511 p.*, 1987. URL http://adsabs.harvard.edu/abs/1987ah...book.....B.

d. M. v. Broeke, J. Bamber, J. Ettema, E. Rignot, E. Schrama, d. W. J. v. Berg, v. E. Meijgaard, I. Velicogna, and B. Wouters. Partitioning recent greenland mass loss. *Science*, 326:984–986, Nov 2009. doi: 10.1126/science.1178176. URL http://dx.doi.org/10.1126/science.1178176.

J. Cappelen. Weather observations from greenland 1958-2013. observation data with description. Technical report, 2014. URL https://scholar.google.nl/scholar.ris?q=info:JXAx_dFLOeYJ:scholar.google.com&output=cite&scirp=0&hl=en.

J. R. Carr, C. R. Stokes, and A. Vieli. Recent progress in understanding marine-terminating arctic outlet glacier response to climatic and oceanic forcing: Twenty years of rapid change. *Progress in Physical Geography*, 37(4):436–467, Apr 2013a. doi: 10.1177/0309133313483163. URL http://dx.doi.org/10.1177/0309133313483163.

J. R. Carr, A. Vieli, and C. Stokes. Influence of sea ice decline, atmospheric warming, and glacier width on marine-terminating outlet glacier behavior in northwest greenland at seasonal to interannual timescales. *J. Geophys. Res. Earth Surf.*, 118(3):1210–1226, Jul 2013b. doi: 10.1002/jgrf.20088. URL http://dx.doi.org/10.1002/jgrf.20088.

N. Chauché, A. Hubbard, J.-C. Gascard, J. E. Box, R. Bates, M. Koppes, A. Sole, P. Christoffersen, and H. Patton. Ice–ocean interaction and calving front morphology at two west greenland tidewater outlet glaciers. *The Cryosphere*, 8(4):1457–1468, 2014. ISSN 19940416. URL http://www.the-cryosphere.net/8/1457/2014/tc-8-1457-2014.html.

J. Cochran, K. J. Tinto, and R. Bell. Icebridge sander airgrav l4 bathymetry. 2015. URL http://dx.doi.org/10.5067/DQVUVQCRYAM4.

J. de Ferranti. chapter The Greenland DEM, viewfinderpanoramas.org. Apr 2009.

F. De Zan. Accuracy of incoherent speckle tracking for circular gaussian signals. *IEEE Geosci. Remote Sensing Lett.*, 11(1):264–267, 2014. URL http://dblp.uni-trier.de/db/journals/lgrs/lgrs11.html#Zan14.

J. A. Dowdeswell, K. A. Hogan, C. O. Cofaigh, E. M. G. Fugelli, J. Evans, and R. Noormets. Late quaternary ice flow in a west greenland fjord and cross-shelf trough system: submarine landforms from rink isbrae to uummannaq shelf and slope. *Quaternary Science Reviews*, 92:292–309, 2014. ISSN 02773791. URL http://www.sciencedirect.com/science/article/pii/S0277379113003430.

M. E. Enderlin, M. I. Howat, S. Jeong, M. Noh, H. J. Angelen, and R. M. Broeke. An improved mass budget for the greenland ice sheet. *Geophysical Research Letters*, 41:866–872, 2014. ISSN 1944-8007. URL http://onlinelibrary.wiley.com/doi/10.1002/2013GL059010/full.

E. Erten, A. Reigber, O. Hellwich, and P. Prats. Glacier velocity monitoring by maximum likelihood texture tracking. *IEEE Transactions on Geoscience and Remote Sensing*, 47, Feb 2009. ISSN 01962892. doi: 10.1109/TGRS.2008.2009932. URL http://dx.doi.org/10.1109/TGRS.2008.2009932.

ESA. chapter Product Types and Processing Levels Sentinel-1: Level-1.

M. Fahnestock, R. Bindschadler, R. Kwok, and K. Jezek. Greenland ice sheet surface properties and ice dynamics from ers-1 sar imagery. *Science*, 262:1530–1534, 1993. ISSN 0036-8075. URL http://science.sciencemag.org/content/262/5139/1530.short.

A. Ferretti, A. Monti-Guarnieri, C. Prati, F. Rocca, and D. Massonet. *InSAR Principles-Guidelines for SAR Interferometry Processing and Interpretation*, volume 19. 2007. ISBN 9290922338. URL http://adsabs.harvard.edu/abs/2007ESATM..19.....F.

P. M. Fischer and D. R. Powell. A simple model for the influence of push-morainal banks on the calving and stability of glacial tidewater termini. *Journal of Glaciology*, 44:31–41, 1998. ISSN 0022-1430. URL http://cat.inist.fr/?aModele=afficheN&cpsidt=1610409.

D. Floricioiu and M. Gottwald. *DLR's TerraSAR-X contributes to international fleet of radar satellites to map the Arctic and Antarctica*, chapter DLR's TerraSAR-X contributes to international fleet of radar satellites to map the Arctic and Antarctica. 2008.

L. A. Gray, N. Short, E. K. Mattar, and C. K. Jezek. Velocities and flux of the filchner ice shelf and its tributaries determined from speckle tracking interferometry. *Canadian Journal of Remote Sensing*, 27:193–206, Jun 2001. doi: 10.1080/07038992.2001.10854936. URL http://dx.doi.org/10.1080/07038992.2001.10854936.

F. R. Hanssen. *Radar interferometry: data interpretation and error analysis*, volume 2. Springer Science & Business Media, 2001. ISBN 0792369459. URL https://books.google.nl/books?hl=nl&lr=&id=bqNkJUk4wtMC&oi=fnd&pg=PA4&dq=Ramon+Hanssen&ots=8NhtlIGZfS&sig=-BjGqYaWKv26ZIYsyrZZnDBj81w.

O. Harant, L. Bombrun, G. Vasile, L. Ferro-Famil, and M. Gay. Displacement estimation by maximum-likelihood texture tracking. *Selected Topics in Signal Processing, IEEE Journal of*, 5:398–407, 2011. URL http://ieeexplore.ieee.org/xpls/abs_all.jsp?arnumber=5671450.

I. M. Howat, J. E. Box, Y. Ahn, A. Herrington, and E. M. McFadden. Seasonal variability in the dynamics of marine-terminating outlet glaciers in greenland. *Journal of Glaciology*, 56(198):601–613, 2010. URL http://www.ingentaconnect.com/content/igsoc/jog/2010/00000056/00000198/art00004.

M. I. Howat, A. Negrete, and E. B. Smith. The greenland ice mapping project (gimp) land classification and surface elevation data sets. *The Cryosphere*, 8:1509–1518, 2014. ISSN 1994-0416. URL http://www.the-cryosphere.net/8/1509/2014/tc-8-1509-2014.pdf.

IPCC. *Summary for Policymakers*, book section SPM, page 1–30. Cambridge University Press, Cambridge, United Kingdom and New York, NY, USA, 2013. ISBN ISBN 978-1-107-66182-0. doi: 10.1017/CBO9781107415324.004. URL www.climatechange2013.org.

M. Jakobsson, L. Mayer, B. Coakley, J. A. Dowdeswell, S. Forbes, B. Fridman, H. Hodnesdal, R. Noormets, R. Pedersen, M. Rebesco, H. W. Schenke, Y. Zarayskaya, D. Accettella, A. Armstrong, R. M. Anderson, P. Bienhoff, A. Camerlenghi, I. Church, M. Edwards, J. V. Gardner, J. K. Hall, B. Hell, O. Hestvik, Y. Kristoffersen, C. Marcussen, R. Mohammad, D. Mosher, S. V. Nghiem, M. T. Pedrosa, P. G. Travaglini, and P. Weatherall. The international bathymetric chart of the arctic ocean (ibcao) version 3.0. *Geophys. Res. Lett.*, 39(12), Jun 2012. doi: 10.1029/2012gl052219. URL http://dx.doi.org/10.1029/2012GL052219.

A. Jenkins. Convection-driven melting near the grounding lines of ice shelves and tidewater glaciers. *J. Phys. Oceanogr.*, 41(12):2279–2294, Dec 2011. doi: 10.1175/jpo-d-11-03.1. URL http://dx.doi.org/10.1175/JPO-D-11-03.1.

I. Joughin, M. I. Howat, M. Fahnestock, B. Smith, W. Krabill, B. R. Alley, H. Stern, and M. Truffer. Continued evolution of jakobshavn isbrae following its rapid speedup. *Journal of Geophysical Research: Earth Surface*, 113, 2008. ISSN 2156-2202. URL http://onlinelibrary.wiley.com/doi/10.1029/2008JF001023/full.

I. Joughin, B. Smith, M. I. Howat, T. Scambos, and T. Moon. Measures greenland ice sheet velocity map from insar data. *All data). National Snow and Ice Data Center*, 2010a. URL https://scholar.google.nl/scholar.ris?q=info:cghgOQrzkHsJ:scholar.google.com&output=cite&scirp=0&hl=en.

I. Joughin, B. E. Smith, and W. Abdalati. Glaciological advances made with interferometric synthetic aperture radar. *Journal of Glaciology*, 56(200):1026–1042, 2010b. URL http://www.ingentaconnect.com/content/igsoc/jog/2010/00000056/00000200/art00008.

B. Kampes and S. Usai. Doris: The delft object-oriented radar interferometric software. *2nd international symposium on operationalization of remote sensing, enschede, the netherlands*, 16, 1999. URL http://citeseerx.ist.psu.edu/viewdoc/download?doi=10.1.1.46.1689&rep=rep1&type=pdf.

S. Kenneth, Evans, H. Robert, and Baringer. Avhrr pathfinder version 5.2 level 3 collated (l3c) global 4km sea surface temperature. 2011. URL http://dx.doi.org/10.7289/V5WD3XHB.

M. König, J.-G. Winther, T. N. Knudsen, and T. Guneriussen. Equilibrium-and firnline detection with multipolarization sar–first results. *Proc. Workshop EARSeL-Special Interest Group 'Land Ice and Snow*, 2000. URL http://eproceedings.org/static/vol01_1/01_1_koenig1.pdf.

M. Konig, J. Winther, and E. Isaksson. Measuring snow and glacier ice properties from satellite. *Reviews of Geophysics*, 39:1–27, 2001. ISSN 1944-9208. URL http://onlinelibrary.wiley.com/doi/10.1029/1999RG000076/full.

R. Lindenbergh. Lecture notes in geo-signal analysis, November 2012.

S. Marshak. chapter Ice and the Nature of Glaciers.

L. C. Martınez. Multidimensional speckle noise, modelling and filtering related to sar data. *Unpublished Ph. D. dissertation, Universitat Politecnica De Catalunya, Barcelona, Spain*, 2003. URL https://www.researchgate.net/profile/Carlos_Lopez-Martinez/publication/265495886_MULTIDIMENSIONAL_SPECKLE_NOISE_MODELLING_AND_FILTERING_RELATED_TO_SAR_DATA/links/54afa2a70cf29661a3d5c5f4.pdf.

F. M. Meier and A. Post. Fast tidewater glaciers. *Journal of Geophysical Research: Solid Earth*, 92:9051–9058, 1987. ISSN 2156-2202. URL http://onlinelibrary.wiley.com/doi/10.1029/JB092iB09p09051/full.

N. Miranda, B. Rosich, C. Santella, and M. Grion. Review of the impact of ers-2 piloting modes on the sar doppler stability. *Proceedings Fringe '03*, pages 1–5, 2003. URL http://citeseerx.ist.psu.edu/viewdoc/download?doi=10.1.1.380.471&rep=rep1&type=pdf.

T. Moon and I. Joughin. Changes in ice front position on greenland's outlet glaciers from 1992 to 2007. *Journal of Geophysical Research*, 113(F2), Jun 2008. ISSN 01480227. doi: 10.1029/2007JF000927. URL http://dx.doi.org/10.1029/2007JF000927.

T. Moon, I. Joughin, B. Smith, and I. Howat. 21st-century evolution of greenland outlet glacier velocities. *Science*, 336(6081):576–578, May 2012. doi: 10.1126/science.1219985. URL http://dx.doi.org/10.1126/science.1219985.

T. Moon, I. Joughin, B. Smith, M. R. v. d. Broeke, W. J. v. d. Berg, B. Noël, and M. Usher. Distinct patterns of seasonal greenland glacier velocity. *Geophysical Research Letters*, 41(20):7209–7216, Oct 2014. doi: 10.1002/2014gl061836. URL http://dx.doi.org/10.1002/2014GL061836.

T. Moon, I. Joughin, and B. Smith. Seasonal to multiyear variability of glacier surface velocity, terminus position, and sea ice/ice mélange in northwest greenland. *J. Geophys. Res. Earth Surf.*, May 2015. doi: 10.1002/2015jf003494. URL http://dx.doi.org/10.1002/2015JF003494.

M. Morlighem, E. Rignot, J. Mouginot, H. Seroussi, and E. Larour. Deeply incised submarine glacial valleys beneath the greenland ice sheet. nat. geosci. 7, 418–422. 2014. URL https://scholar.google.nl/scholar.ris?q=info:g5UkFACq2UIJ:scholar.google.com&output=cite&scirp=1&hl=en.

M. Morlighem, E. Rignot, J. Mouginot, H. Seroussi, and E. Larour. Icebridge bedmachine greenland, version 2, bedrock altitude. 2015. URL http://dx.doi.org/10.5067/AD7B0HQNSJ29.

M. Morlighem, J. Bondzio, H. Seroussi, E. Rignot, E. Larour, A. Humbert, and S. Rebuffi. Modeling of store gletscher's calving dynamics, west greenland, in response to ocean thermal forcing. *Geophysical Research Letters*, 2016. ISSN 1944-8007. URL http://onlinelibrary.wiley.com/doi/10.1002/2016GL067695/pdf.

M. F. Nick. Modelling the behaviour of tidewater glaciers. 2006. URL http://dspace.library.uu.nl/handle/1874/12538.

M. F. Nick, J. C. Van der Veen, A. Vieli, and I. D. Benn. A physically based calving model applied to marine outlet glaciers and implications for the glacier dynamics. *Journal of Glaciology*, 56:781–794, 2010. ISSN 0022-1430. URL http://www.ingentaconnect.com/content/igsoc/jog/2010/00000056/00000199/art00004.

A. J. Ogilvy and A. J. Ogilvy. *Theory of wave scattering from random rough surfaces*. Hilger Bristol et al., 1991. ISBN 0750300639. URL http://www.ulb.tu-darmstadt.de/tocs/16250087.pdf.

R. Oost, R. Hanssen, and F. van Leijen. Prospects of the sentinel-1 interferometric wide swath mode for glacial velocity estimation. Technical report, Jul 2015.

B. W. S. Paterson. *The physics of glaciers*. Butterworth-Heinemann, 1994. ISBN 0750647426. URL https://books.google.nl/books?hl=nl&lr=&id=X75dmp9QFbgC&oi=fnd&pg=PA1&dq=The+physics+of+glaciers&ots=BgW_JbcaGr&sig=VelQOpq9TzFRASdbPSZSYCNTG0w.

A. Post. Preliminary hydrography and historic terminal changes of columbia glacier, alaska. Technical report, 1975. URL http://pubs.er.usgs.gov/publication/ha559.

D. R. Powell. Glacimarine processes at grounding-line fans and their growth to ice-contact deltas. *Geological Society, London, Special Publications*, 53:53–73, 1990. ISSN 0305-8719. URL http://sp.lyellcollection.org/content/53/1/53.short.

N. Reeh, N. S. Madsen, and J. J. Mohr. Combining sar interferometry and the equation of continuity to estimate the three-dimensional glacier surface-velocity vector. *Journal of Glaciology*, 45:533–538, 1999. ISSN 0022-1430. URL http://cat.inist.fr/?aModele=afficheN&cpsidt=1255121.

E. Rignot and J. Mouginot. Ice flow in greenland for the international polar year 2008-2009: Ice flow greenland 2009. *Geophysical Research Letters*, 39(11):n/a–n/a, Jun 2012. ISSN 00948276. doi: 10.1029/2012GL051634. URL http://dx.doi.org/10.1029/2012GL051634.

E. Rignot, K. Echelmeyer, and W. Krabill. Penetration depth of interferometric synthetic aperture radar signals in snow and ice. *Geophysical Research Letters*, 28:3501–3504, 2001. ISSN 1944-8007. URL http://onlinelibrary.wiley.com/doi/10.1029/2000GL012484/full.

E. Rignot, M. Koppes, and I. Velicogna. Rapid submarine melting of the calving faces of west greenland glaciers. *Nature Geoscience*, 3(3):187–191, Feb 2010. doi: 10.1038/ngeo765. URL http://dx.doi.org/10.1038/ngeo765.

E. Rignot, I. Velicogna, M. R. v. d. Broeke, A. Monaghan, and J. T. M. Lenaerts. Acceleration of the contribution of the greenland and antarctic ice sheets to sea level rise. *Geophysical Research Letters*, 38(5), Mar 2011. doi: 10.1029/2011gl046583. URL http://dx.doi.org/10.1029/2011GL046583.

E. Rignot, I. Fenty, Y. Xu, C. Cai, and C. Kemp. Undercutting of marine-terminating glaciers in west greenland. *Geophysical Research Letters*, 42:5909–5917, 2015. ISSN 1944-8007. URL http://onlinelibrary.wiley.com/doi/10.1002/2015GL064236/full.

E. Rignot, I. Fenty, Y. Xu, C. Cai, I. Velicogna, O. C. Cofaigh, A. J. Dowdeswell, W. Weinrebe, G. Catania, and D. Duncan. Bathymetry data reveal glaciers vulnerable to ice-ocean interaction in uummannaq and vaigat glacial fjords, west greenland. *Geophysical Research Letters*, 43:2667–2674, 2016. ISSN 1944-8007. URL http://onlinelibrary.wiley.com/doi/10.1002/2016GL067832/full.

R. Scharroo and P. Visser. Precise orbit determination and gravity field improvement for the ers satellites. *Journal of Geophysical Research: Oceans*, 103:8113–8127, 1998. ISSN 2156-2202. URL http://onlinelibrary.wiley.com/doi/10.1029/97JC03179/full.

R. Scheiber, M. Jager, P. Prats-Iraola, F. De Zan, and D. Geudtner. Speckle tracking and interferometric processing of terrasar-x tops data for mapping nonstationary scenarios. *Selected Topics in Applied Earth Observations and Remote Sensing, IEEE Journal of*, PP:1–12, 2015. ISSN 19391404. doi: 10.1109/JSTARS.2014.2360237. URL http://ieeexplore.ieee.org/xpl/articleDetails.jsp?arnumber=6926747.

A. Seale, P. Christoffersen, R. I. Mugford, and M. OLeary. Ocean forcing of the greenland ice sheet: Calving fronts and patterns of retreat identified by automatic satellite monitoring of eastern outlet glaciers. *J. Geophys. Res.*, 116(F3), 2011. doi: 10.1029/2010jf001847. URL http://dx.doi.org/10.1029/2010JF001847.

F. Straneo, P. Heimbach, O. Sergienko, G. Hamilton, G. Catania, S. Griffies, R. Hallberg, A. Jenkins, I. Joughin, R. Motyka, and et al. chapter Challenges to understanding the dynamic response of Greenland's marine terminating glaciers to oceanic and atmospheric forcing. American Meteorological Society, 2013.

P. Teunissen, J. D. Simons, and M. C. C. J. Tiberius. Probability and observation theory. 2004. URL http://espace.library.curtin.edu.au/R?func=dbin_jump_full&object_id=167196&local_base=gen01-era02.

J. Todd and P. Christoffersen. Are seasonal calving dynamics forced by buttressing from ice mélange or undercutting by melting?: Outcomes from full-stokes simulations of store glacier, west greenland. *The Cryosphere*, 8(6):2353–2365, 2014. doi: 10.5194/tc-8-2353-2014. URL http://dx.doi.org/10.5194/tc-8-2353-2014.

T. F. Ulaby, K. R. Moore, and K. A. Fung. Microwave remote sensing active and passive-volume iii: from theory to applications. 1986. URL http://infoscience.epfl.ch/record/51983.

J. C. Van der Veen. *Fundamentals of glacier dynamics*. CRC Press, 2013. ISBN 1439835667. URL https://books.google.nl/books?hl=nl&lr=&id=prWTLalwVn4C&oi=fnd&pg=PP1&dq=van+der+veen+glaciers&ots=CPQh93-V4h&sig=HQr6VJyAEQFfnSJyd2BIDseL6j4.

F. van Leijen. *Persistent Scatterer Interferometry Based on Geodetic Estimation Theory*. 2014. ISBN 9789461862990. URL https://books.google.nl/books?id=_0B4rgEACAAJ.

J. G. Van Oostveen. chapter Optimized Extraction of InSAR derived Along-Track Deformation during Glacial Surges. TU Delft, Delft University of Technology, 2014. URL http://repository.tudelft.nl/view/ir/uuid:5852018f-8db9-4639-a1e8-aa31ce6571f6/.

J. I. Walter, J. E. Box, S. Tulaczyk, E. E. Brodsky, I. M. Howat, Y. Ahn, and A. Brown. Oceanic mechanical forcing of a marine-terminating greenland glacier. *Annals of Glaciology*, 53(60):181–192, Nov 2012. doi: 10.3189/2012aog60a083. URL http://dx.doi.org/10.3189/2012AoG60A083.

K. Wilson, D. Patrick, and J. Blair. Radar scattering statistics for digital terrain models. *Defense and Security*, pages 248–258, 2005. URL http://proceedings.spiedigitallibrary.org/proceeding.aspx?articleid=864623.

X. Xu, L. Tsang, and S. Yueh. Electromagnetic models of co/cross polarization of bicontinuous/dmrt in radar remote sensing of terrestrial snow at x-and ku-band for coreh2o and sclp applications. *Selected Topics in Applied Earth Observations and Remote Sensing, IEEE Journal of*, 5:1024–1032, 2012. ISSN 1939-1404. URL http://ieeexplore.ieee.org/xpls/abs_all.jsp?arnumber=6185696.

T. Y. Yoon, M. Eineder, N. Yague-Martinez, and O. Montenbruck. Terrasar-x precise trajectory estimation and quality assessment. *Geoscience and Remote Sensing, IEEE Transactions on*, 47:1859–1868, 2009. ISSN 0196-2892. URL http://ieeexplore.ieee.org/xpls/abs_all.jsp?arnumber=4760272.

A

TERMINUS POSITION AND GLACIER VELOCITY RESULTS

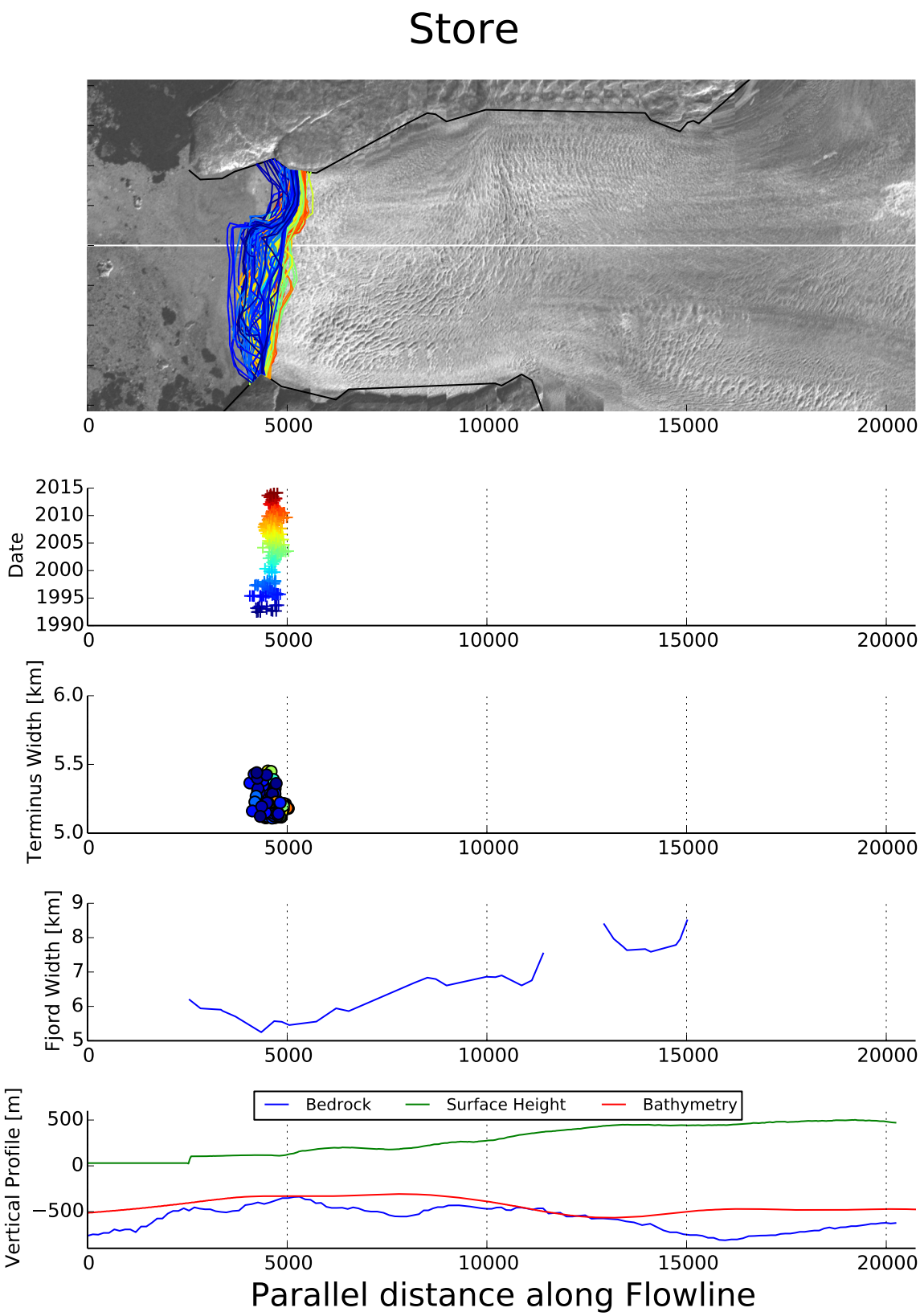

Figure A.1: An overview of the Equivalent Terminus Position (ETP) of Støre Gletscher. The upper graph shows the digitized terminus positions in the fjord. Here, the Flowline Reference System (FRS) has been used to wrap the fjord. The second graph shows the ETP in time, and the third graph shows the width of the terminus position. The fourth graph (fjord width) and fifth graph (fjord depth) depict the fjord topography. The bathymetry is considered less accurate than the bedrock but generally covers more of the fjord.

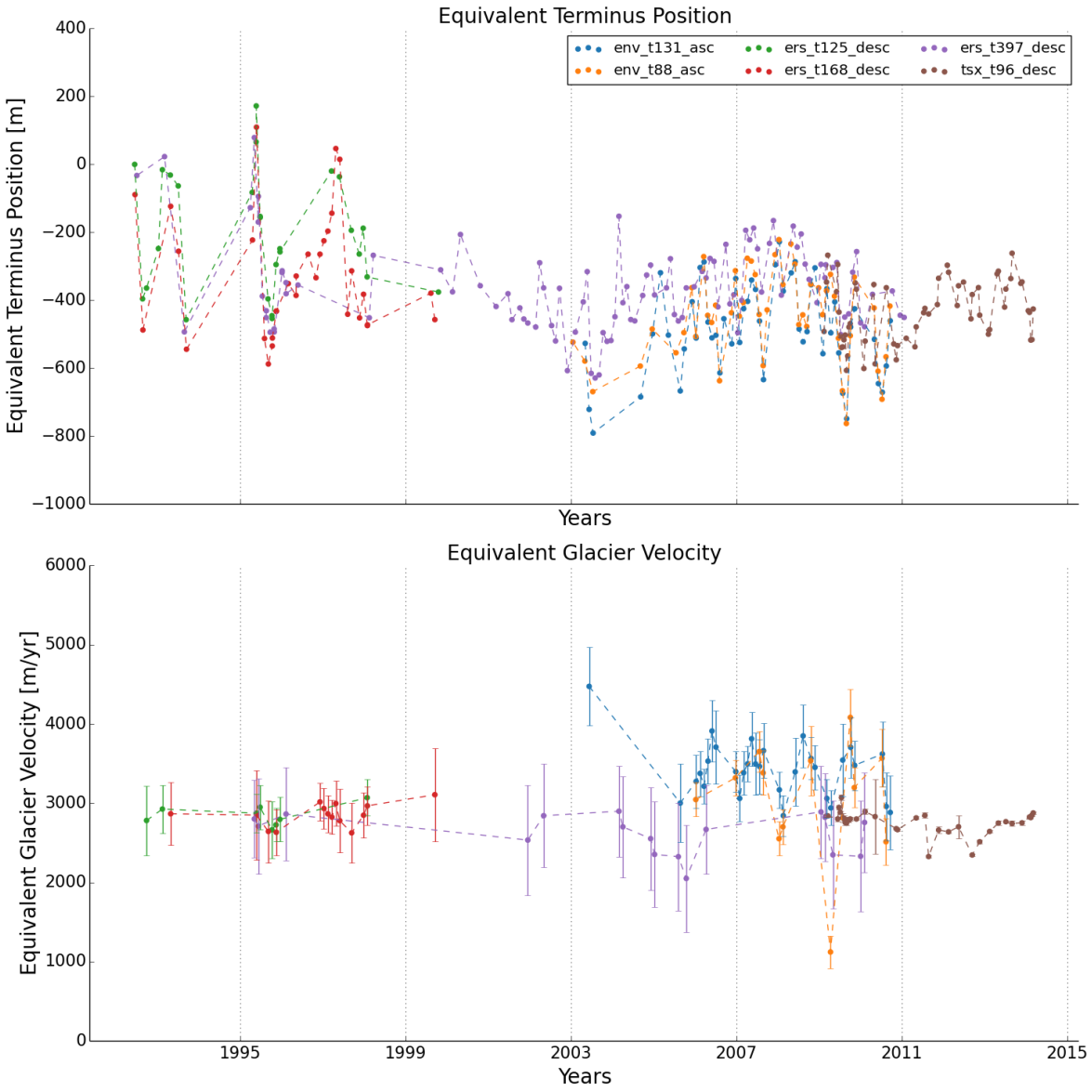

Figure A.2: An overview of the Equivalent Terminus Position and Equivalent Glacier Velocity of Støre Gletscher. The different colors denote the different satellite missions used.

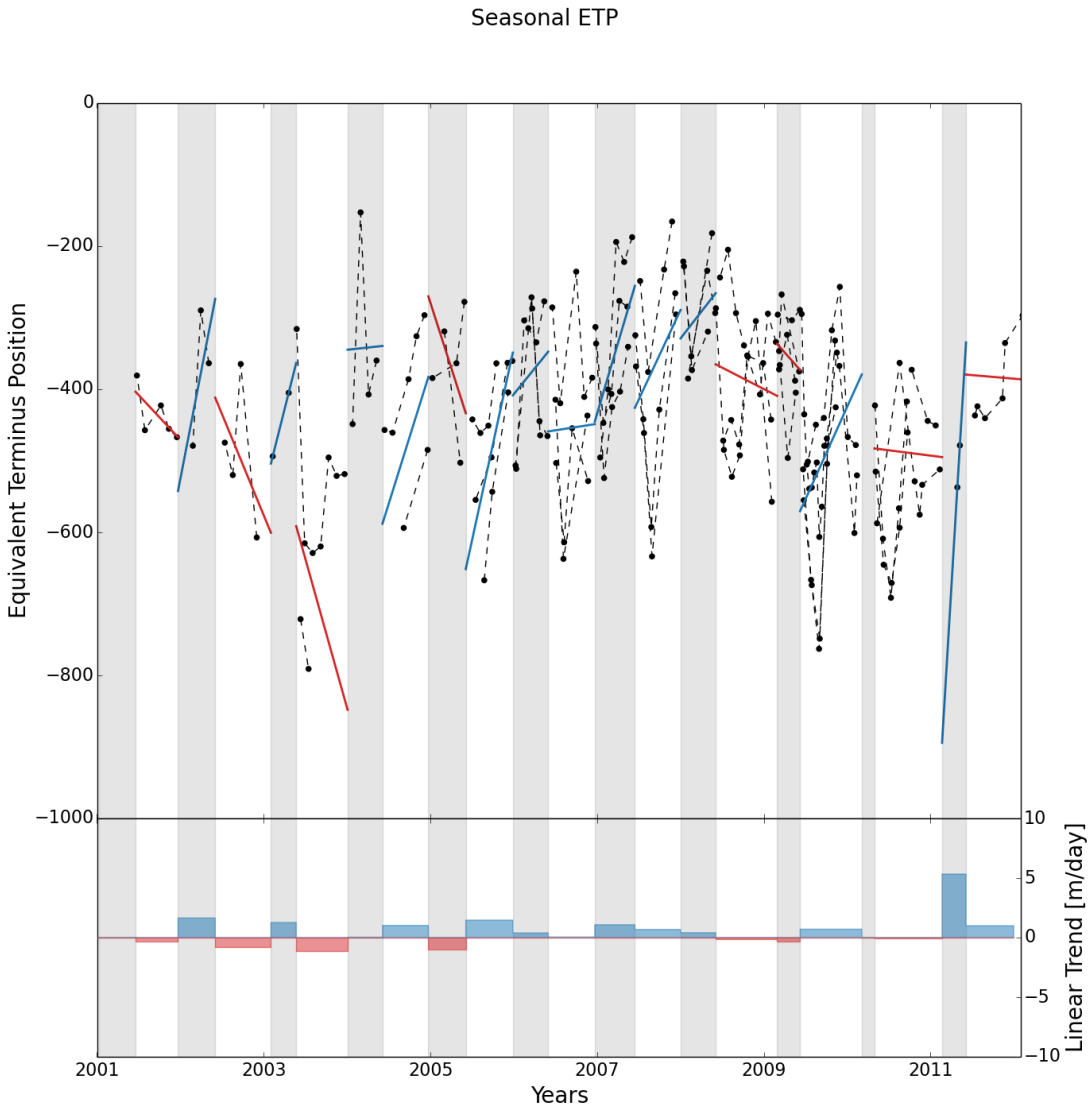

Figure A.3: An overview of the seasonal variations in Equivalent Terminus Position at Støre Gletscher. The gray bars indicate periods of high SIF, and white bars indicate periods of low SIF. The black dots are ETP estimations, and the blue and red lines are estimated linear trends within each bar. The linear trend is depicted below, where blue indicates advance and red indicates retreat of the ETP. In order to avoid issues related to biases, the estimated linear trends are an average of the estimated linear trend per satellite mission. Some trends are based on few points, and therefore the lower bars should be interpreted with caution.

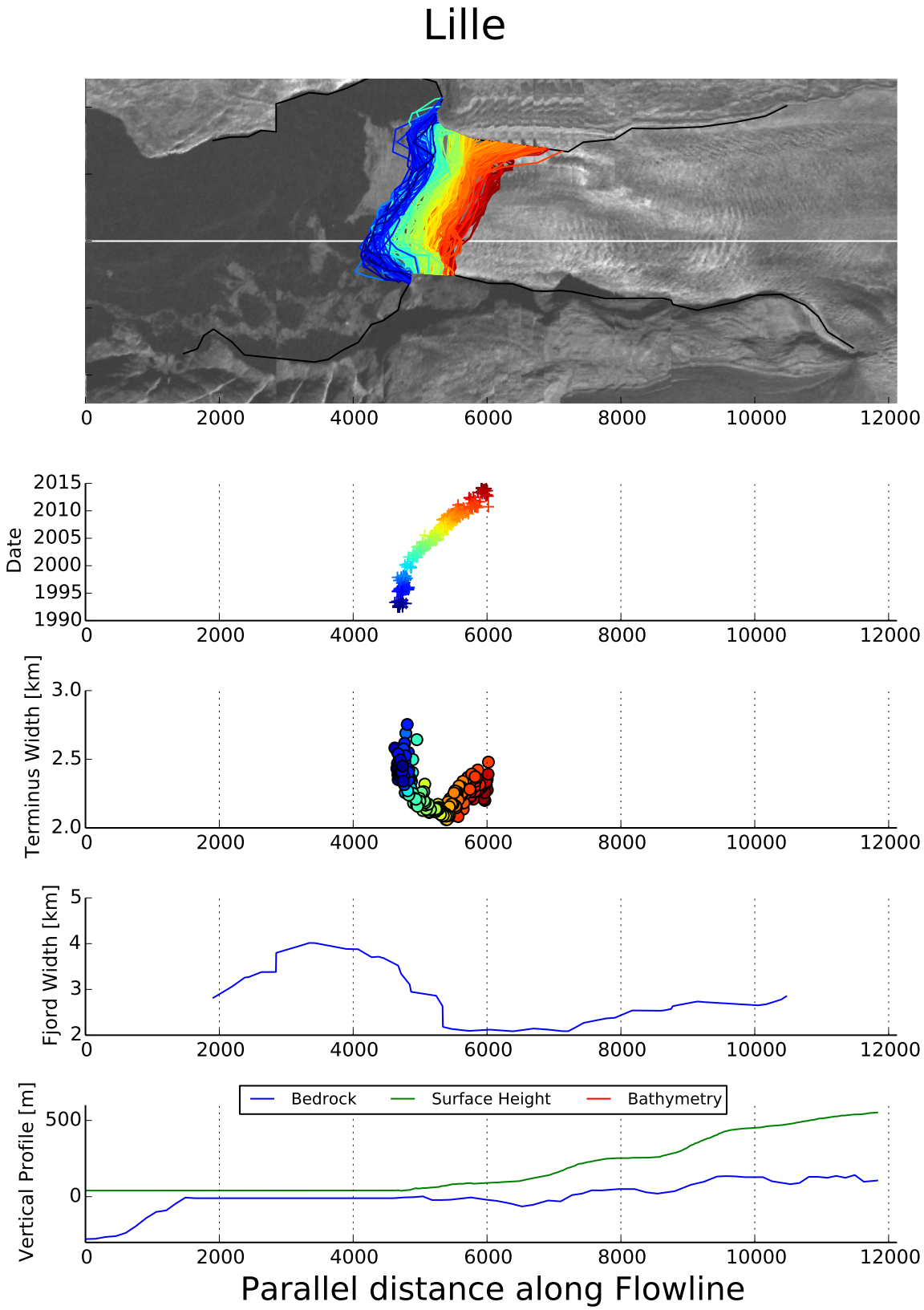

Figure A.4: An overview of the Equivalent Terminus Position (ETP) of Lille Gletscher. The upper graph shows the digitized terminus positions in the fjord. Here, the Flowline Reference System (FRS) has been used to wrap the fjord. The second graph shows the ETP in time, and the third graph shows the width of the terminus position. The fourth graph (fjord width) and fifth graph (fjord depth) depict the fjord topography. The bathymetry is considered less accurate than the bedrock but generally covers more of the fjord.

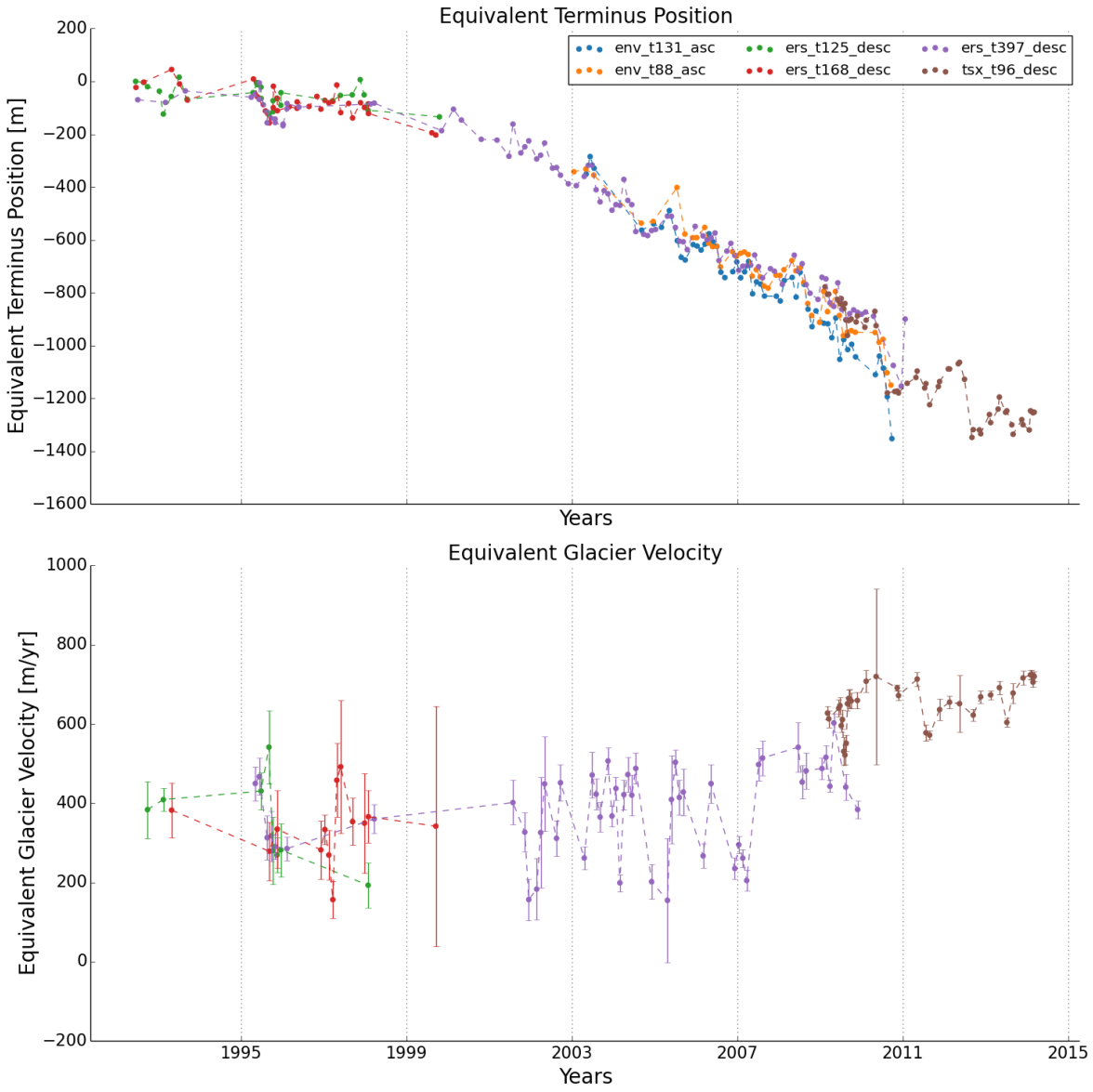

Figure A.5: An overview of the Equivalent Terminus Position and Equivalent Glacier Velocity of Lille Gletscher. The different colors denote the different satellite missions used.

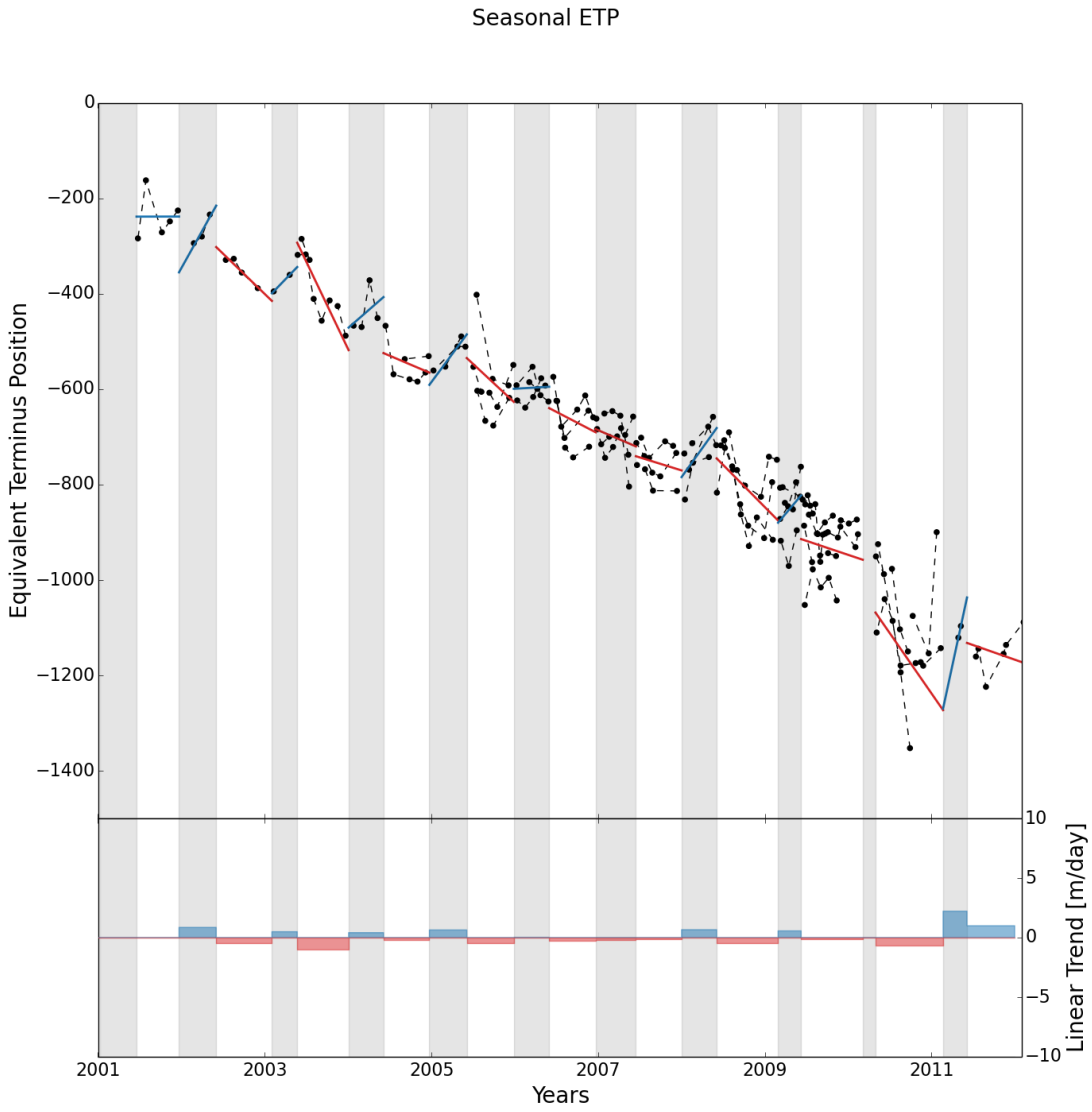

Figure A.6: An overview of the seasonal variations in Equivalent Terminus Position at Lille Gletscher. The gray bars indicate periods of high SIF, and white bars indicate periods of low SIF. The black dots are ETP estimations, and the blue and red lines are estimated linear trends within each bar. The linear trend is depicted below, where blue indicates advance and red indicates retreat of the ETP. In order to avoid issues related to biases, the estimated linear trends are an average of the estimated linear trend per satellite mission. Some trends are based on few points, and therefore the lower bars should be interpreted with caution.

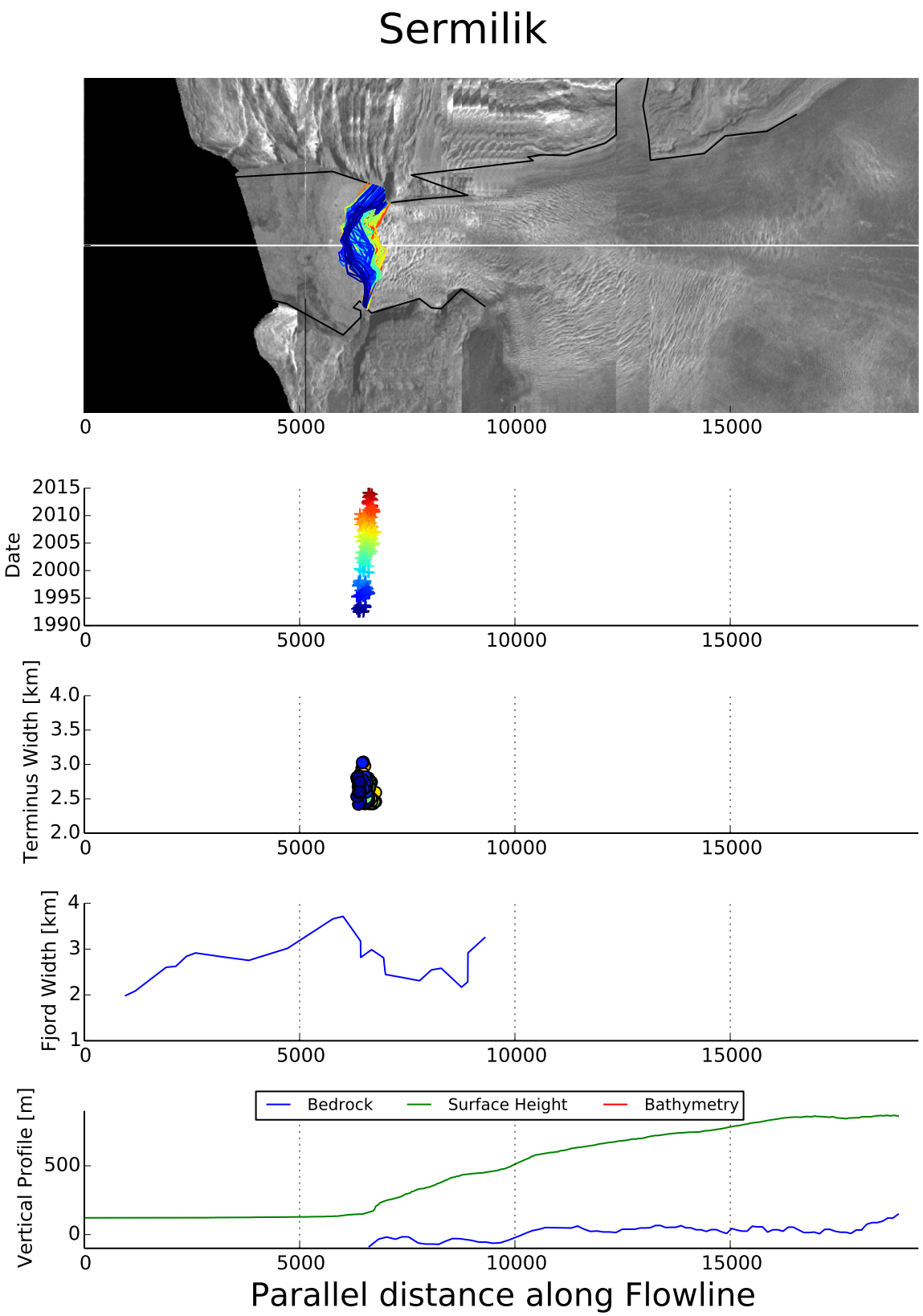

Figure A.7: An overview of the Equivalent Terminus Position (ETP) of Sermilik. The upper graph shows the digitized terminus positions in the fjord. Here, the Flowline Reference System (FRS) has been used to wrap the fjord. The second graph shows the ETP in time, and the third graph shows the width of the terminus position. The fourth graph (fjord width) and fifth graph (fjord depth) depict the fjord topography. The bathymetry is considered less accurate than the bedrock but generally covers more of the fjord.

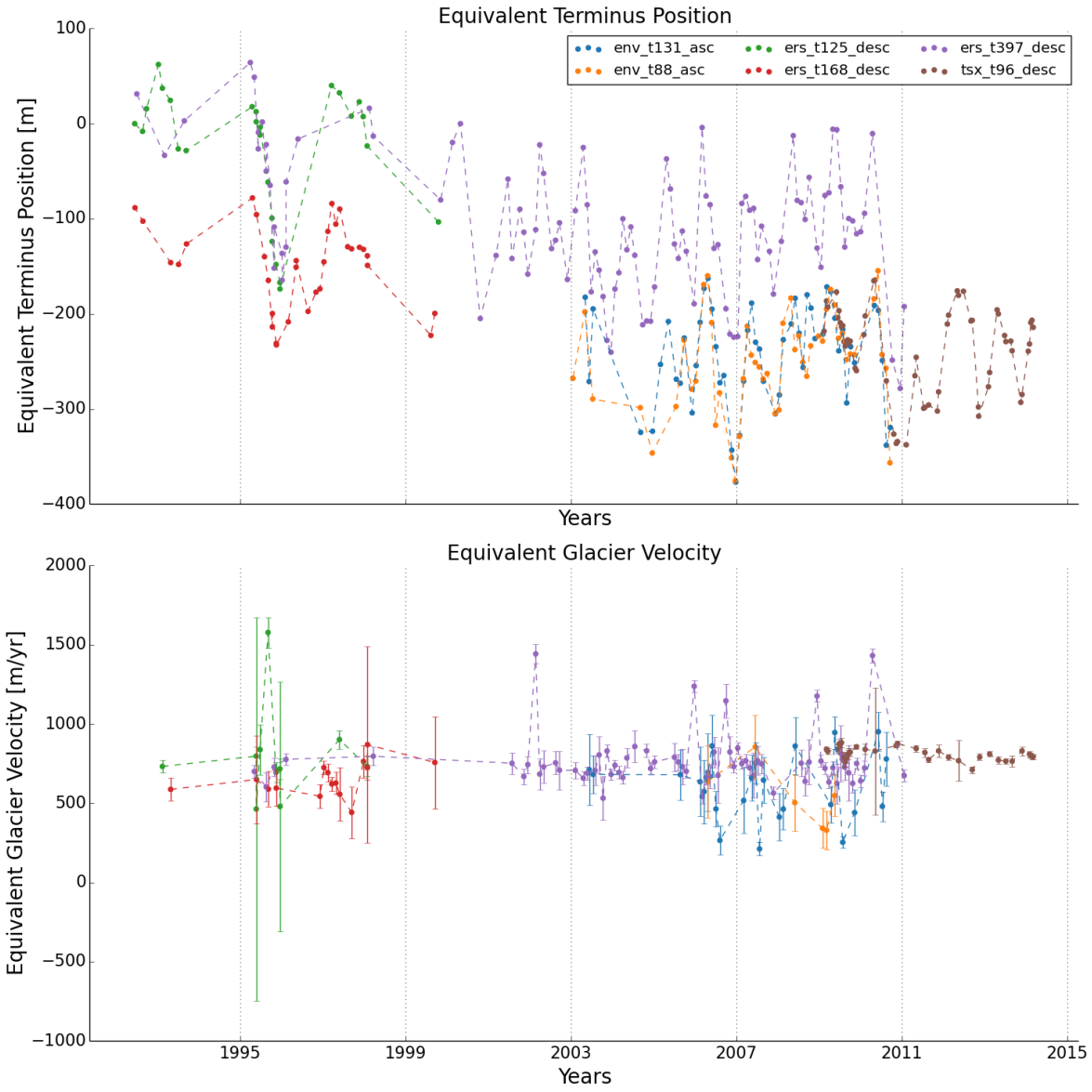

Figure A.8: An overview of the Equivalent Terminus Position and Equivalent Glacier Velocity of Sermilik. The different colors denote the different satellite missions used.

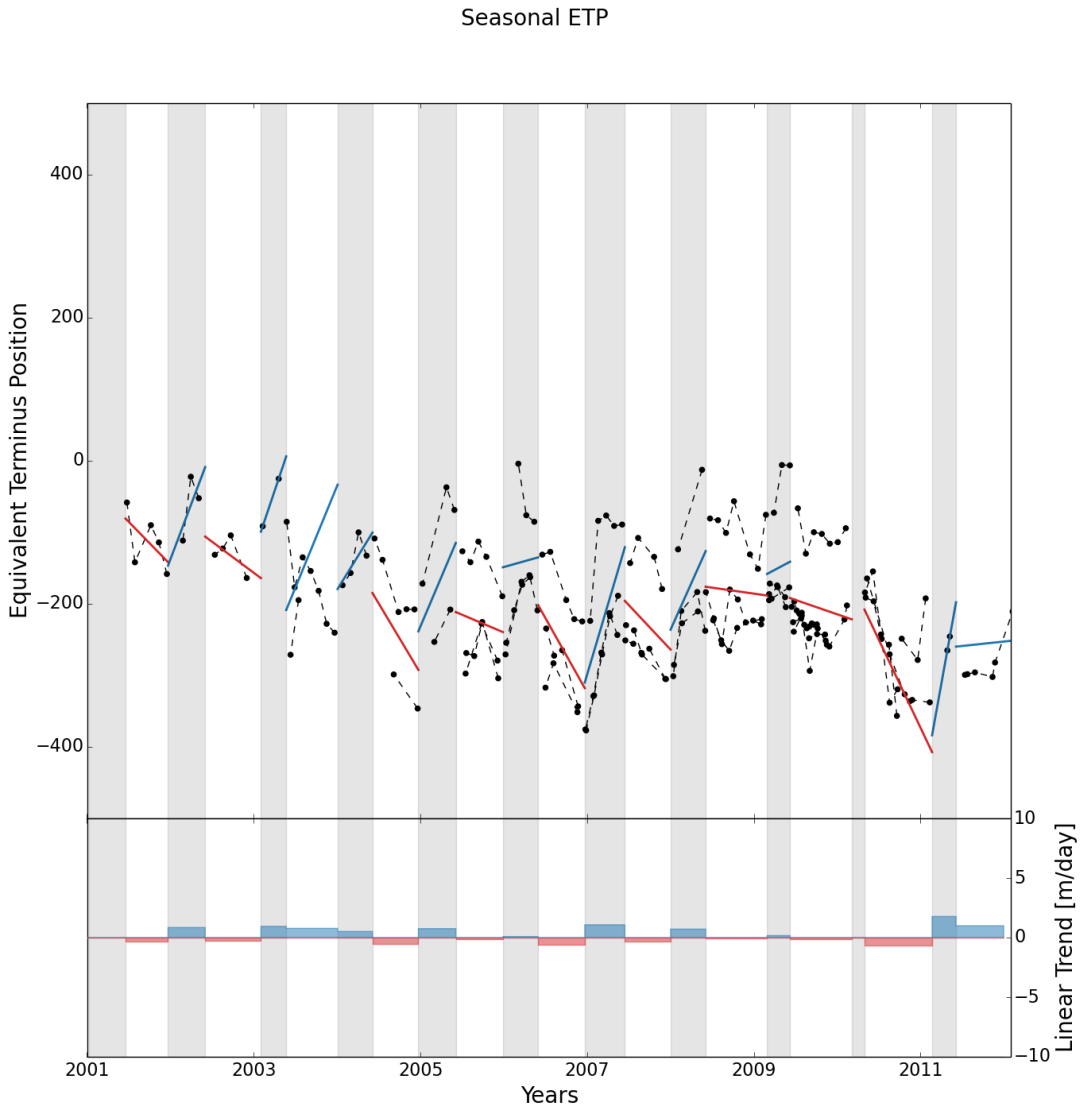

Figure A.9: An overview of the seasonal variations in Equivalent Terminus Position at Sermilik. The gray bars indicate periods of high SIF, and white bars indicate periods of low SIF. The black dots are ETP estimations, and the blue and red lines are estimated linear trends within each bar. The linear trend is depicted below, where blue indicates advance and red indicates retreat of the ETP. In order to avoid issues related to biases, the estimated linear trends are an average of the estimated linear trend per satellite mission. Some trends are based on few points, and therefore the lower bars should be interpreted with caution.

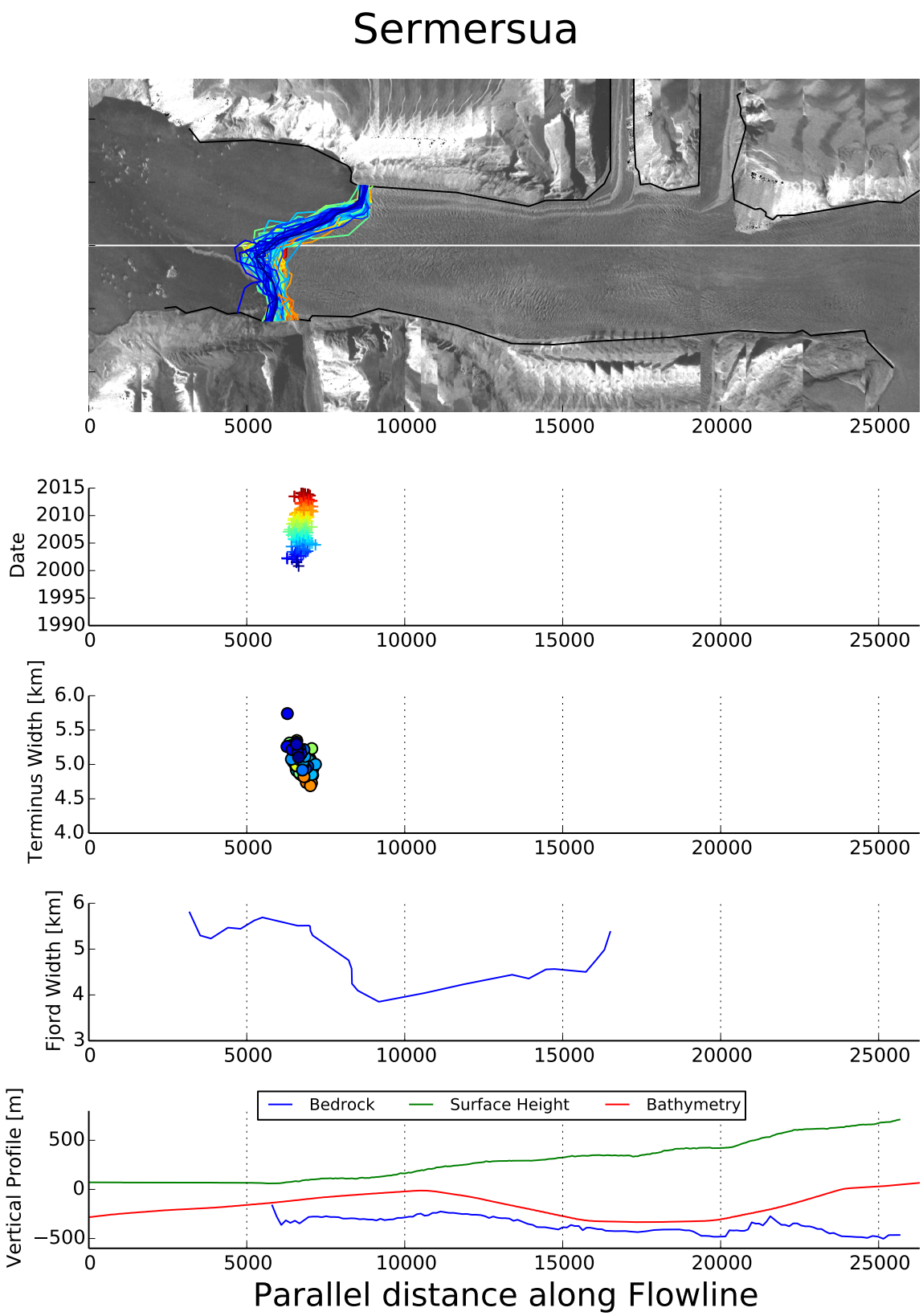

Figure A.10: An overview of the Equivalent Terminus Position (ETP) of Kangerlussuup Sermersua. The upper graph shows the digitized terminus positions in the fjord. Here, the Flowline Reference System (FRS) has been used to wrap the fjord. The second graph shows the ETP in time, and the third graph shows the width of the terminus position. The fourth graph (fjord width) and fifth graph (fjord depth) depict the fjord topography. The bathymetry is considered less accurate than the bedrock but generally covers more of the fjord.

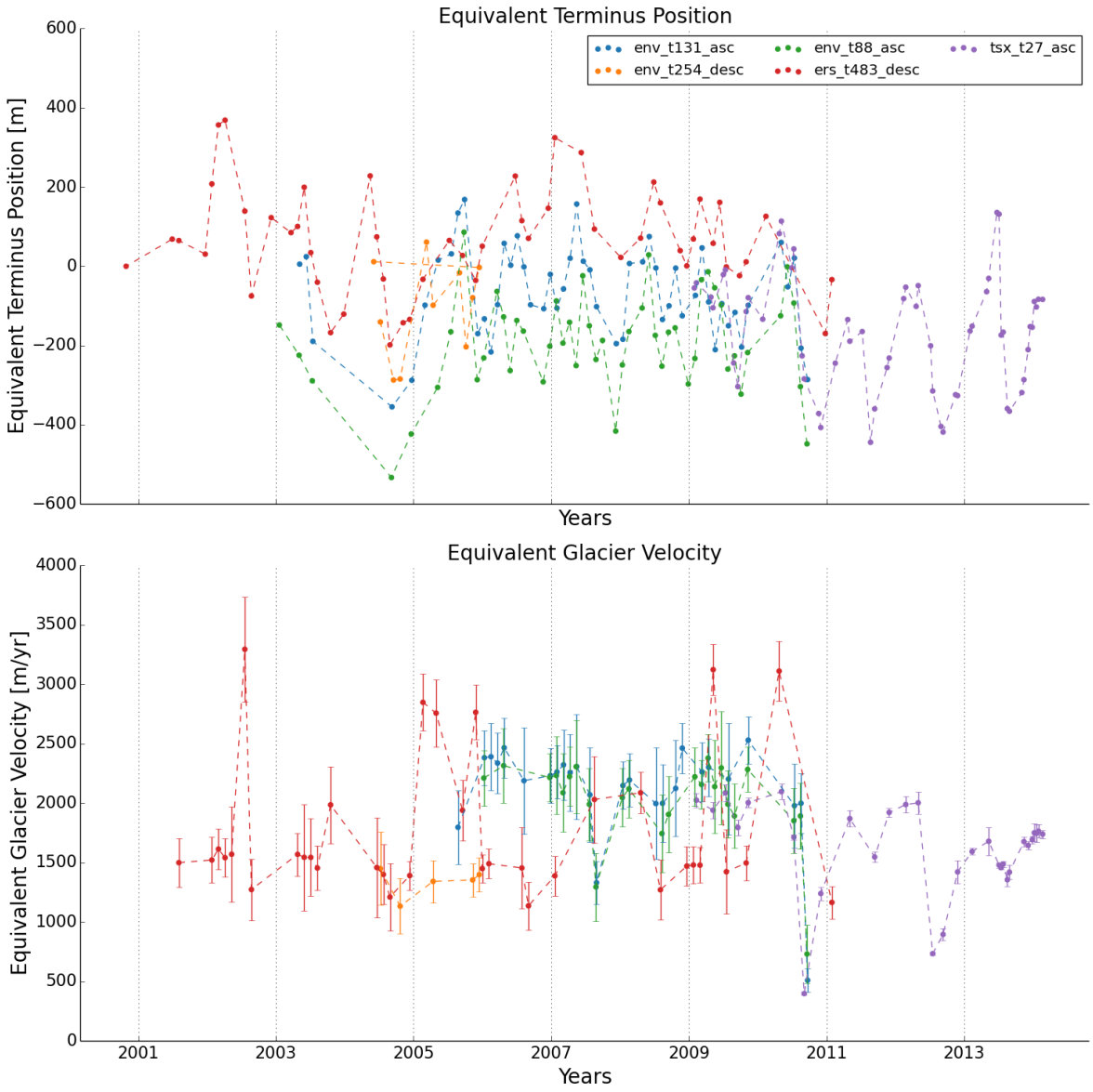

Figure A.11: An overview of the Equivalent Terminus Position and Equivalent Glacier Velocity of Kangerlussuup Sermersua. The different colors denote the different satellite missions used.

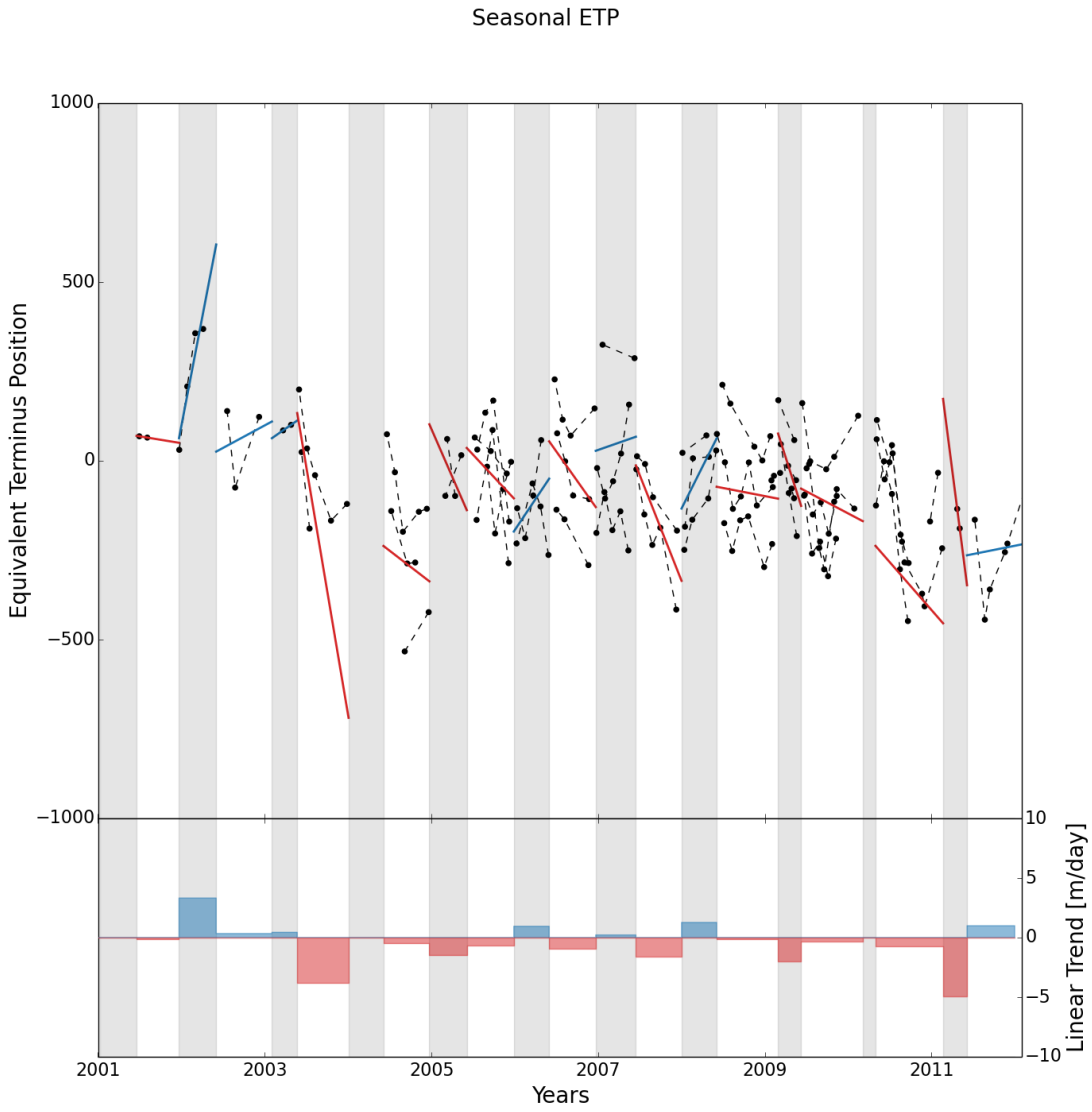

Figure A.12: An overview of the seasonal variations in Equivalent Terminus Position at Kangerlussuup Sermersua. The gray bars indicate periods of high SIF, and white bars indicate periods of low SIF. The black dots are ETP estimations, and the blue and red lines are estimated linear trends within each bar. The linear trend is depicted below, where blue indicates advance and red indicates retreat of the ETP. In order to avoid issues related to biases, the estimated linear trends are an average of the estimated linear trend per satellite mission. Some trends are based on few points, and therefore the lower bars should be interpreted with caution.

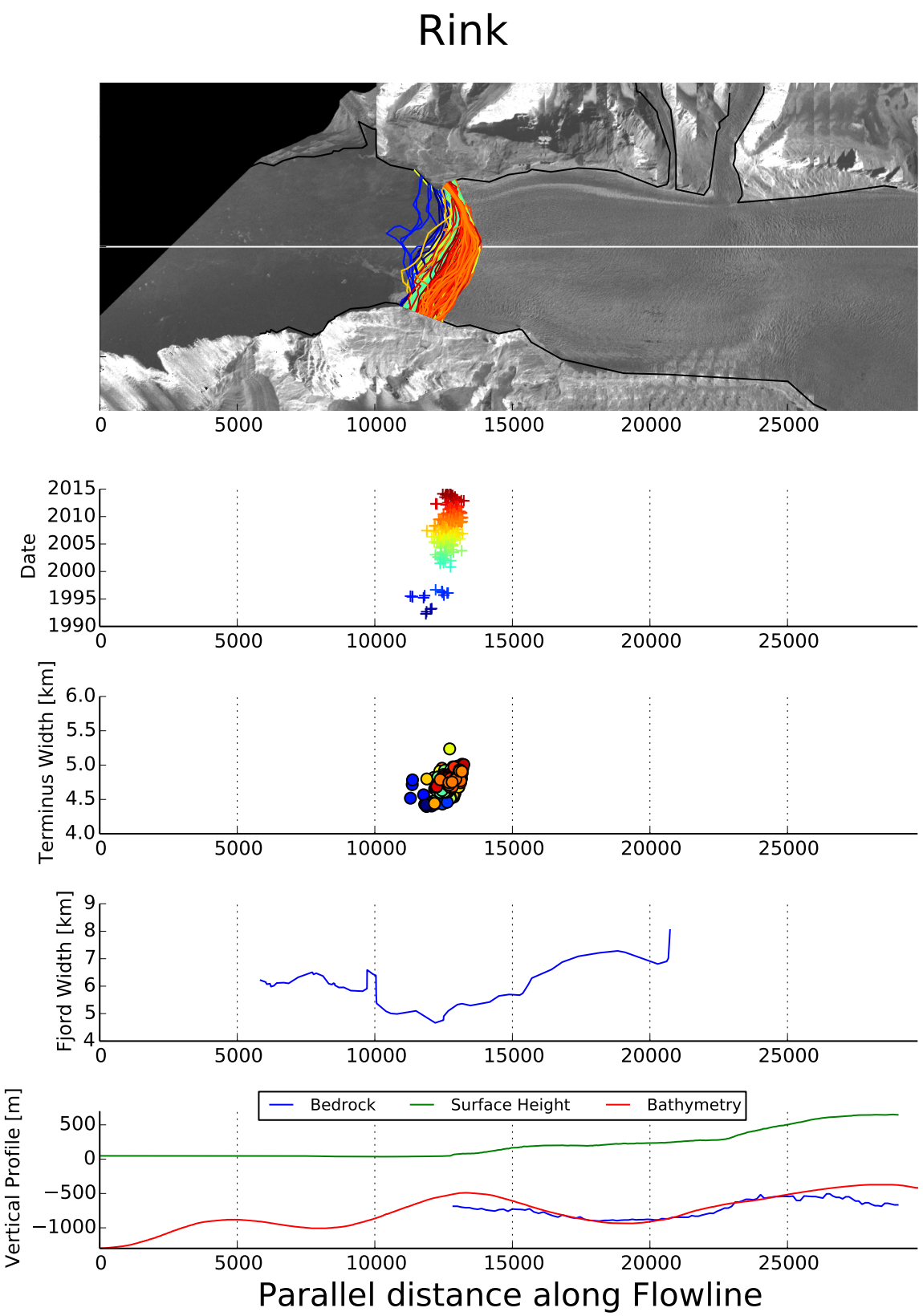

Figure A.13: An overview of the Equivalent Terminus Position (ETP) of Rink Isbræ. The upper graph shows the digitized terminus positions in the fjord. Here, the Flowline Reference System (FRS) has been used to wrap the fjord. The second graph shows the ETP in time, and the third graph shows the width of the terminus position. The fourth graph (fjord width) and fifth graph (fjord depth) depict the fjord topography. The bathymetry is considered less accurate than the bedrock but generally covers more of the fjord.

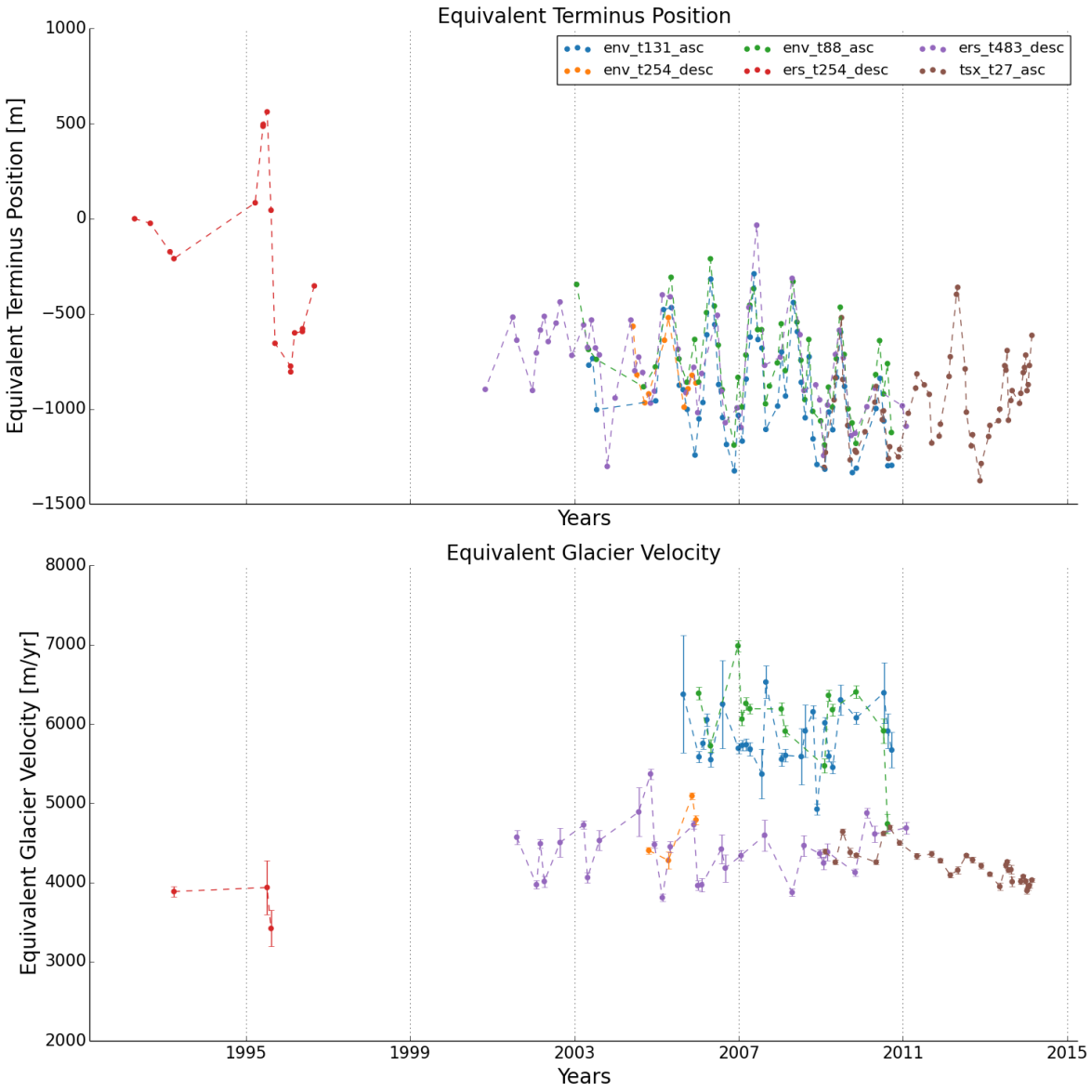

Figure A.14: An overview of the Equivalent Terminus Position and Equivalent Glacier Velocity of Rink Isbræ. The different colors denote the different satellite missions used.

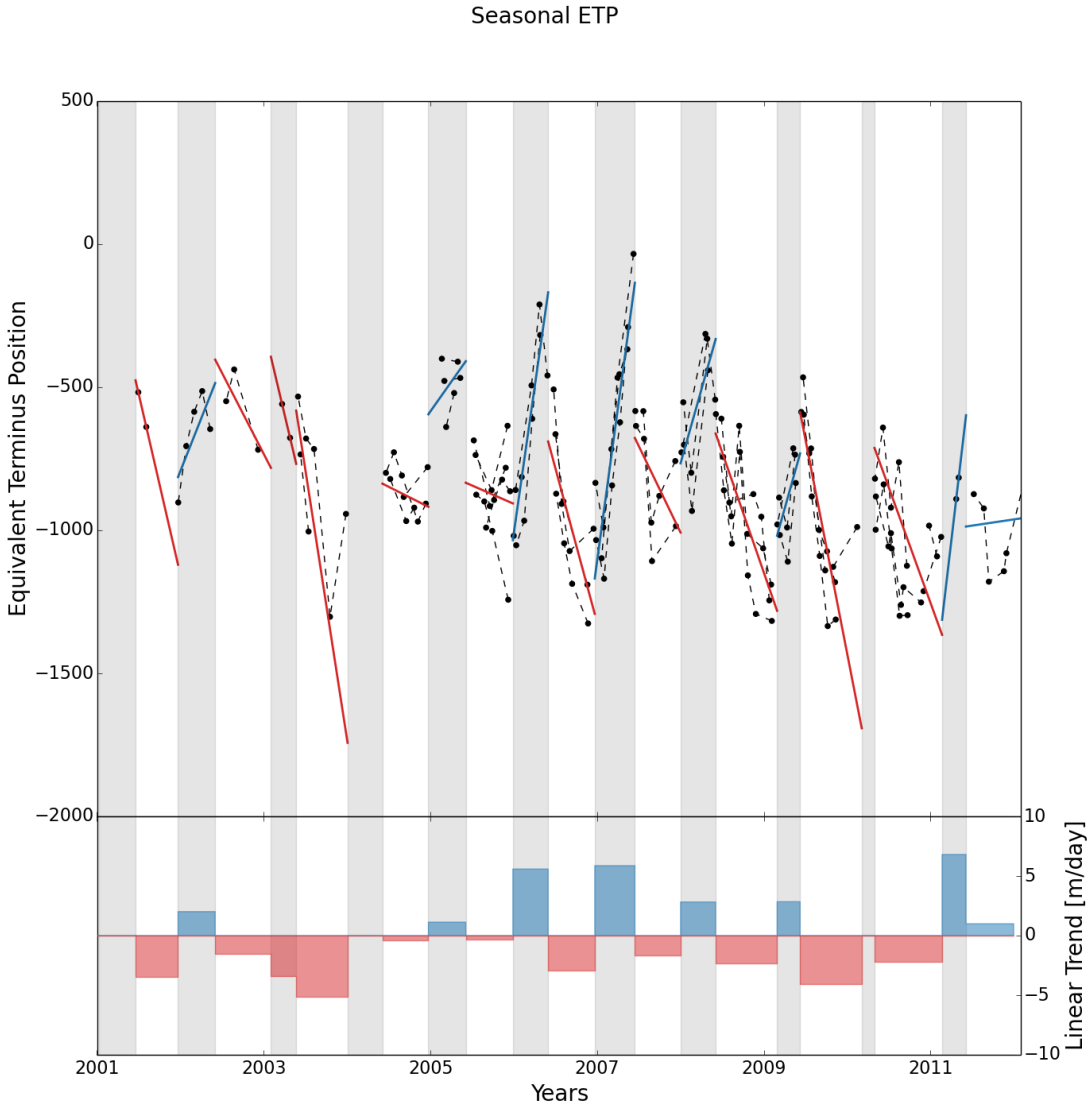

Figure A.15: An overview of the seasonal variations in Equivalent Terminus Position at Rink Isbræ. The gray bars indicate periods of high SIF, and white bars indicate periods of low SIF. The black dots are ETP estimations, and the blue and red lines are estimated linear trends within each bar. The linear trend is depicted below, where blue indicates advance and red indicates retreat of the ETP. In order to avoid issues related to biases, the estimated linear trends are an average of the estimated linear trend per satellite mission. Some trends are based on few points, and therefore the lower bars should be interpreted with caution.

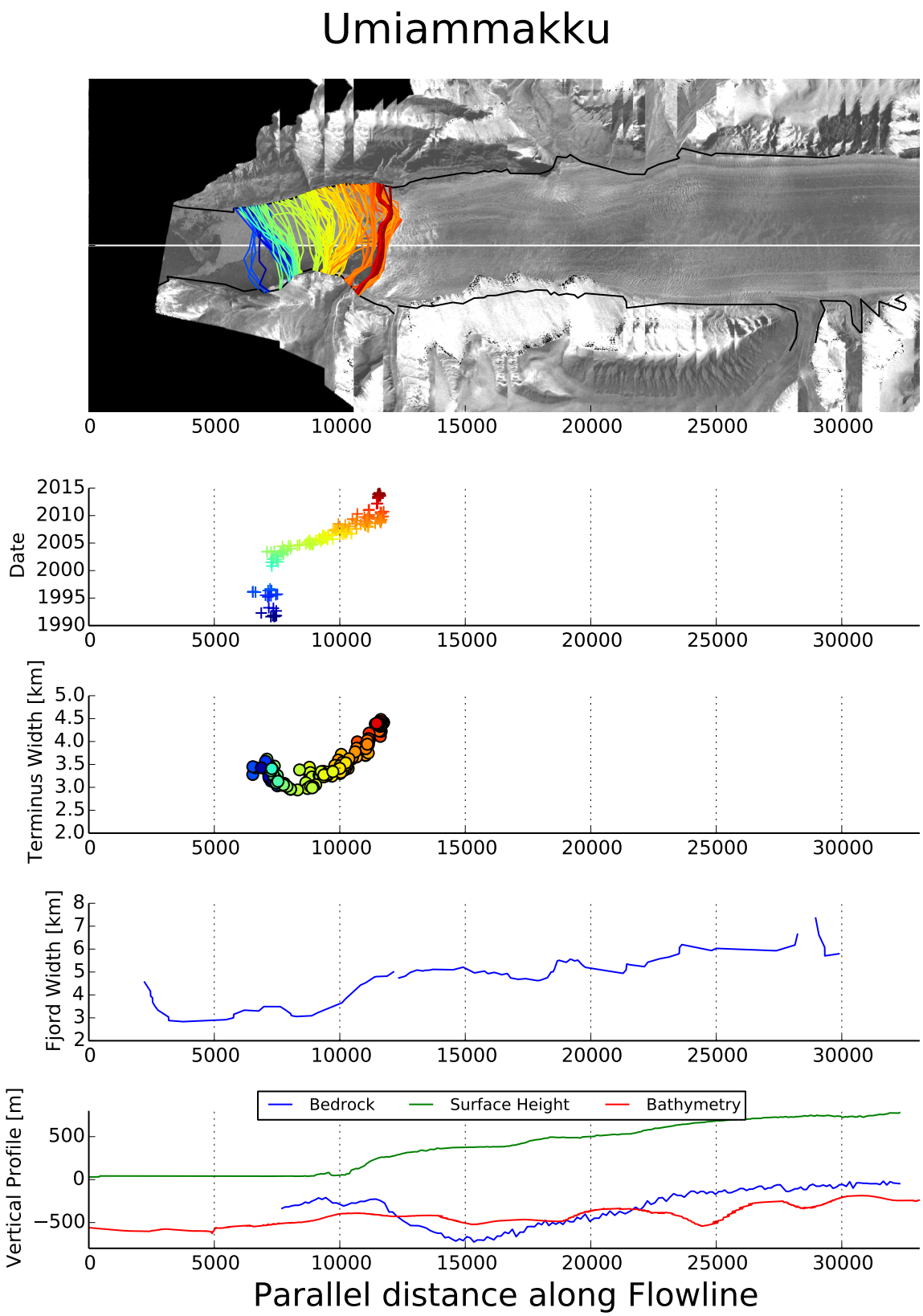

Figure A.16: An overview of the Equivalent Terminus Position (ETP) of Umiammakku. The upper graph shows the digitized terminus positions in the fjord. Here, the Flowline Reference System (FRS) has been used to wrap the fjord. The second graph shows the ETP in time, and the third graph shows the width of the terminus position. The fourth graph (fjord width) and fifth graph (fjord depth) depict the fjord topography. The bathymetry is considered less accurate than the bedrock but generally covers more of the fjord.

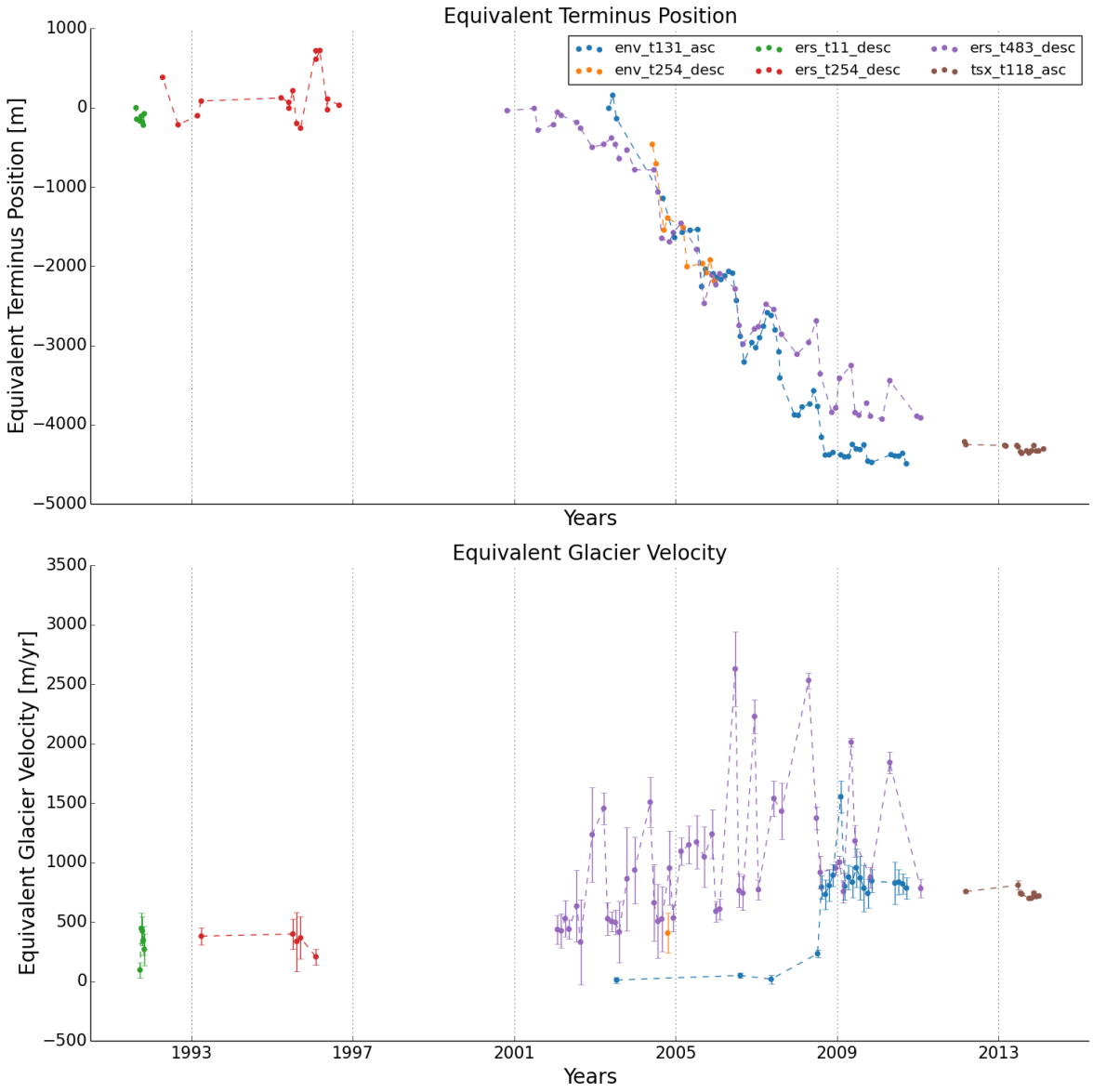

Figure A.17: An overview of the Equivalent Terminus Position and Equivalent Glacier Velocity of Umiammakku. The different colors denote the different satellite missions used.

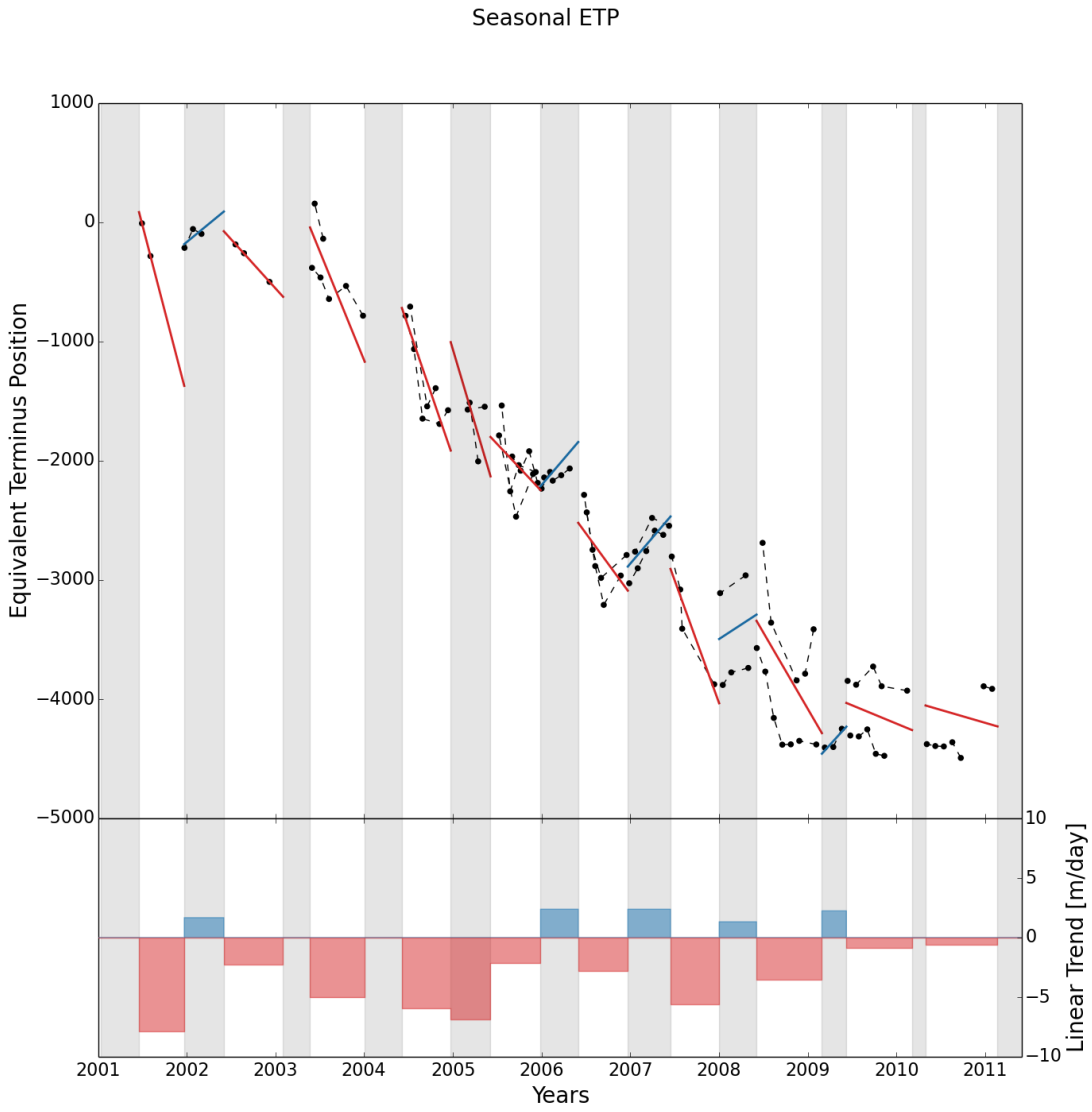

Figure A.18: An overview of the seasonal variations in Equivalent Terminus Position at Umiammakku. The gray bars indicate periods of high SIF, and white bars indicate periods of low SIF. The black dots are ETP estimations, and the blue and red lines are estimated linear trends within each bar. The linear trend is depicted below, where blue indicates advance and red indicates retreat of the ETP. In order to avoid issues related to biases, the estimated linear trends are an average of the estimated linear trend per satellite mission. Some trends are based on few points, and therefore the lower bars should be interpreted with caution.

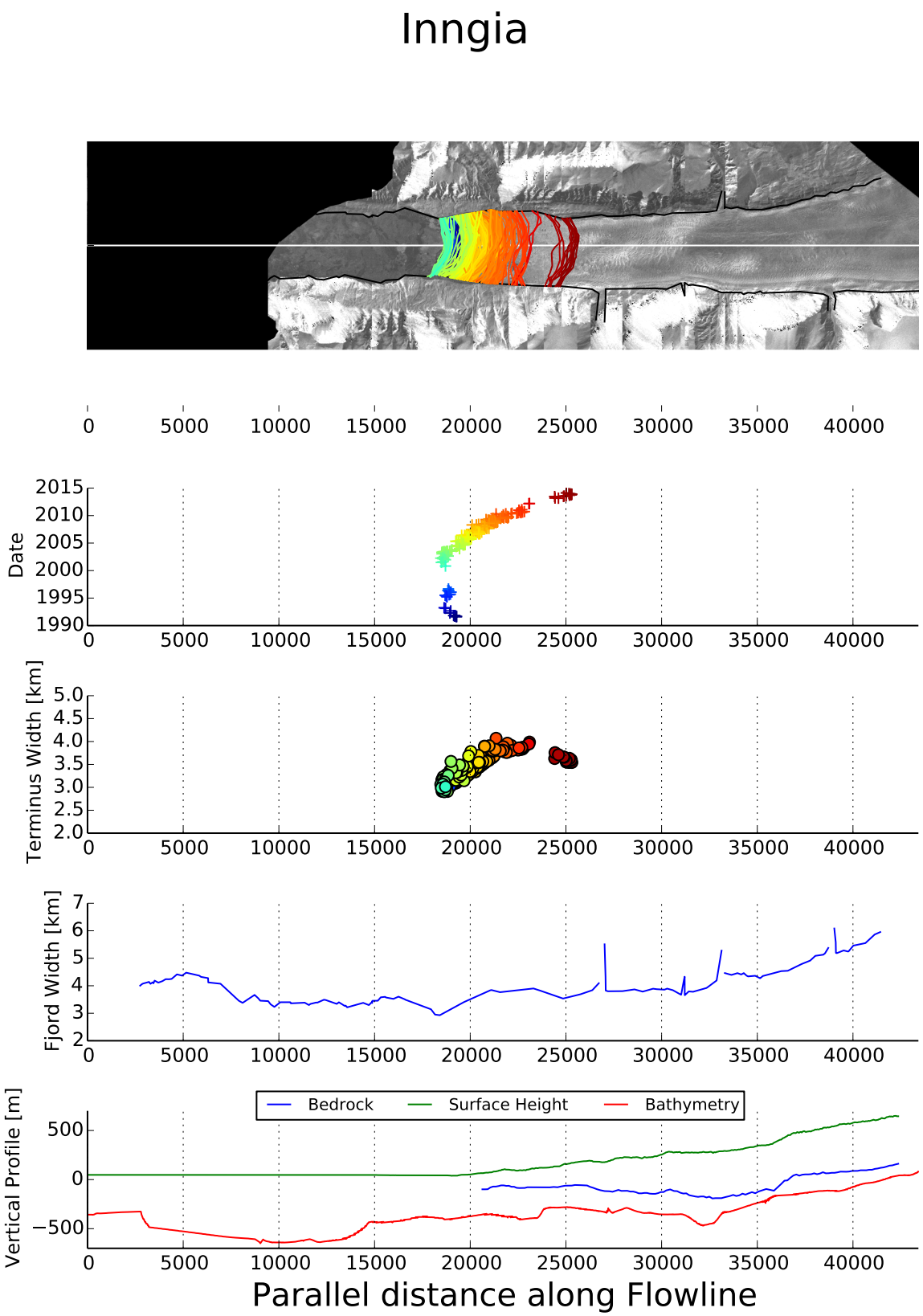

Figure A.19: An overview of the Equivalent Terminus Position (ETP) of Inngia Isbræ. The upper graph shows the digitized terminus positions in the fjord. Here, the Flowline Reference System (FRS) has been used to wrap the fjord. The second graph shows the ETP in time, and the third graph shows the width of the terminus position. The fourth graph (fjord width) and fifth graph (fjord depth) depict the fjord topography. The bathymetry is considered less accurate than the bedrock but generally covers more of the fjord.

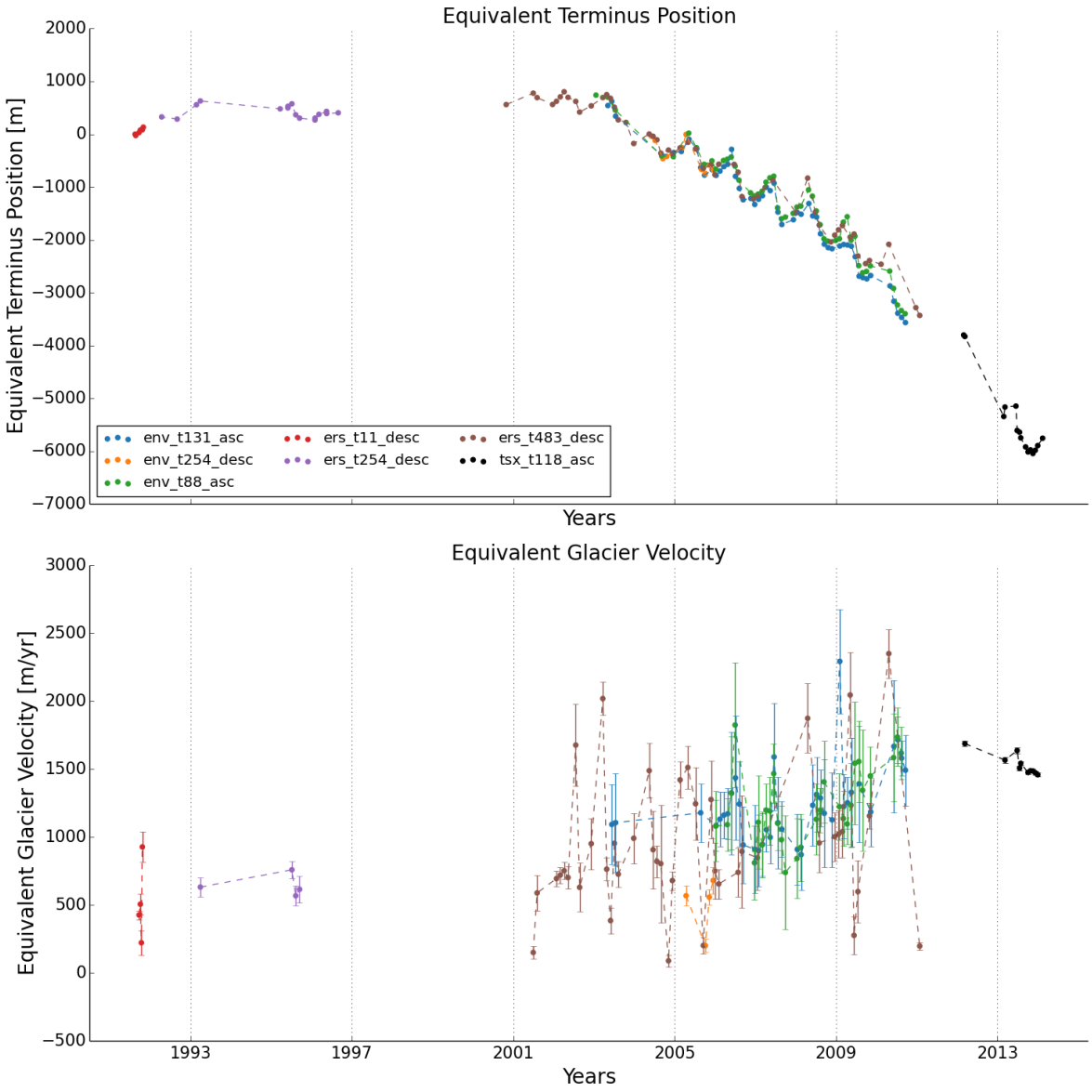

Figure A.20: An overview of the Equivalent Terminus Position and Equivalent Glacier Velocity of Inngia Isbræ. The different colors denote the different satellite missions used.

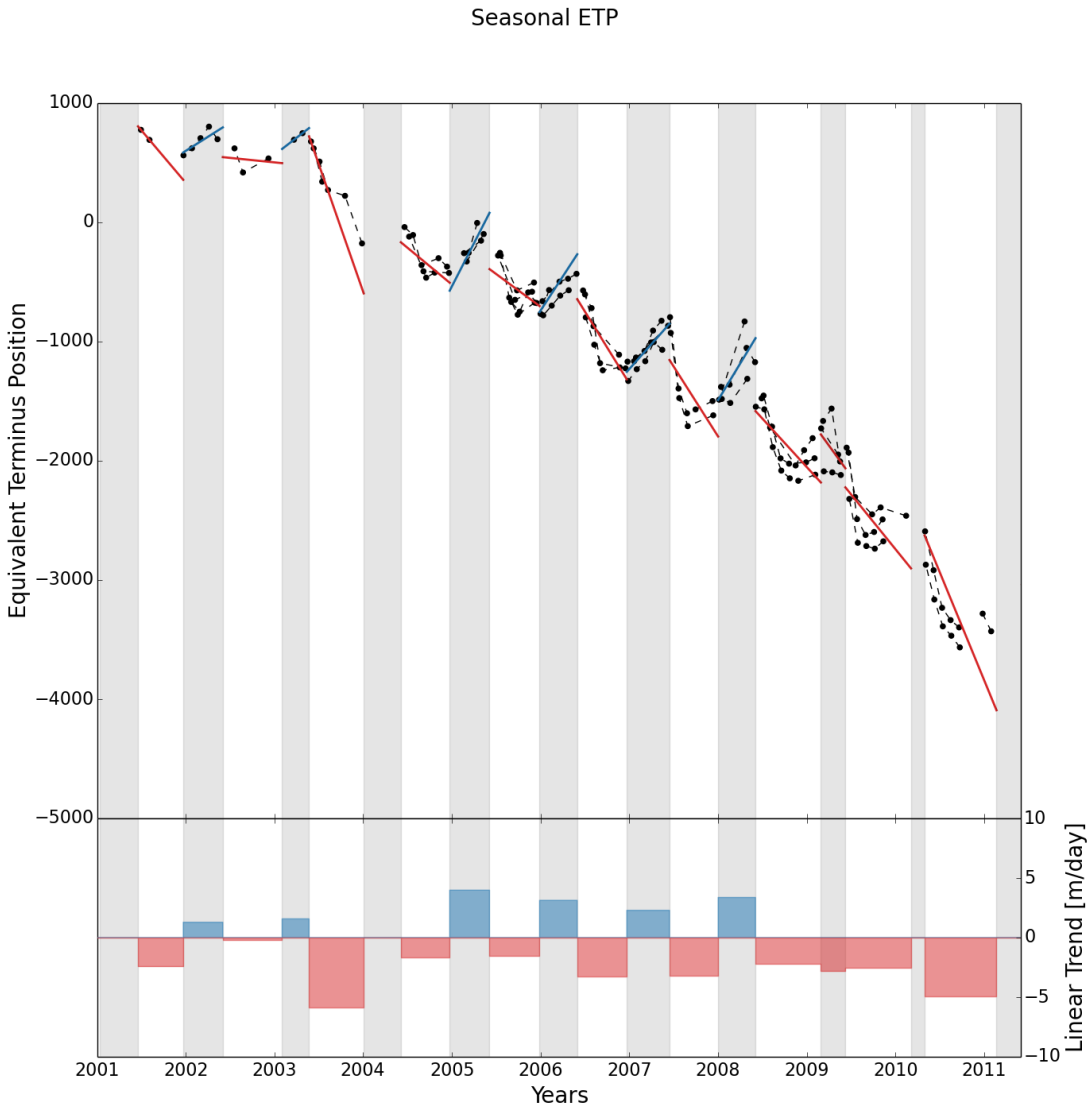

Figure A.21: An overview of the seasonal variations in Equivalent Terminus Position at Inngia Isbræ. The gray bars indicate periods of high SIF, and white bars indicate periods of low SIF. The black dots are ETP estimations, and the blue and red lines are estimated linear trends within each bar. The linear trend is depicted below, where blue indicates advance and red indicates retreat of the ETP. In order to avoid issues related to biases, the estimated linear trends are an average of the estimated linear trend per satellite mission. Some trends are based on few points, and therefore the lower bars should be interpreted with caution.